Effect Of Point Mutations On The Conformation Changes Of PR65 Using Double Nanohole Aperture Tweezer Signals

by

Samuel Mathew

BSc, Abia State University, 2009

MSc, University of Strathclyde, 2013

A Dissertation Submitted in Partial Fulfillment

of the Requirements for the Degree of

DOCTOR OF PHILOSOPHY

in the Department of Electrical and Computer Engineering

© Samuel Mathew, 2024

University of Victoria

All rights reserved. This Dissertation may not be reproduced in whole or in part, by photocopy or other means, without the permission of the author.

Supervisory Committee

Effect Of Point Mutations On The Conformation Changes Of PR65 Using Double Nanohole Aperture Tweezer Signals

by

Samuel Mathew

BSc, Abia State University, 2009

MSc, University of Strathclyde, 2013

Supervisory Committee

Dr. Reuven Gordon (Department of Electrical and Computer Engineering)

Supervisor

Dr. Thomas E. Darcie (Department of Electrical and Computer Engineering)

Departmental Member

Dr. Rustom Bhiladvala (Department of Mechanical Engineering)

Outside Member

Abstract

The purpose of this research was to investigate the effect of point mutations on the conformation changes of PR65 using double nanohole (DNH) optical tweezers. It explored the following questions: how does a dielectric nanoparticle interact with a nanoaperture? Could the way a nanoparticle interacts with a nanoaperture be exploited for probing protein conformation changes using aperture tweezers such as the DNH optical tweezer? What can be said of the behavior of PR65 when trapped in a DNH optical tweezer? Could the behavior of PR65 when trapped in a DNH optical tweezer be explained in terms of how PR65 interacts with the DNH aperture? Does the behavior of PR65 when trapped in a DNH change with point mutation? How might this be exploited for probing the impact of point mutations on the conformational dynamics of PR65 using DNH optical tweezers? The study has implications for tracking mutations in proteins as well as for drug discovery and testing. Methods employed included both theoretical modelling and experimental measurements using the DNH optical tweezer. We modelled the interaction between a nanoaperture and a dielectric nanoparticle in terms of a simple dipole-dipole interaction based on the Rayleigh scattering and Bethe aperture theorems. Our model showed that the interaction enhanced both the trapping potential and the transmission through the aperture in accordance with the self-induced back-action (SIBA) effect, in which a nanoparticle interacting with a focused laser beam aids in its own trapping. The model agreed quite well with numerical simulations performed in Lumerical and revealed that the motion of a particle trapped in an optical tweezer can be used to probe changes in the shape and size of a particle. This is because changes in the shape and size of a particle in an optical tweezer will alter the polarizability of such a

particle, and therefore the restoring force that it felt in the tweezer. This will manifest as differences in root-mean-squared displacement (RMSD) and corner frequency characteristic of the motion of the particle in the optical tweezer between one conformation and another. We thus formulated a hypothesis that if conformation changes induced by point mutations alter the material polarizability of PR65, then the DNH optical tweezer signals acquired by trapping each mutant PR65 will have different RMSDs and corner frequencies from that of wild type PR65. To test this hypothesis, DNH optical tweezers fabricated by colloidal lithography were used to trap PR65 wild type and six of its mutants at a laser power of ~ 22 mW. The resulting optical signals were captured using an avalanche photodiode (APD) connected to a digital USB-4771A data acquisition module and analyzed using MATLAB. Parameters extracted from the acquired signals and studied included the median transition time between the characteristic jump states shown by the acquired signals and the RMSD and corner frequency of the acquired signals. These parameters were higher for some of the mutants of PR65 and lower for others in comparison with wild type PR65. Correlation of the RMSDs with *in silico* mean contour lengths of PR65 wild type and six of its mutants studied was also consistent with this conclusion, and in agreement with our hypothesis. These results imply that PR65 undergoes conformation changes that are impacted by substitution mutations, with some mutations causing PR65 to assume an elongated conformation and other mutations causing PR65 to assume a more compact conformation.

Table of Contents

Supervisory Committee ..... **ii**

Abstract ..... **iii**

Table of Contents ..... **v**

List of Tables ..... **viii**

List of Figures ..... **ix**

Acknowledgments ..... **xiii**

Dedication ..... **xv**

1 Introduction **1**

1.1 An Overview of Plasmonics 1

1.2 Surface Plasmons and the Extraordinary Transmission of Light through Periodically Arranged Subwavelength Apertures 2

1.3 The Beginning of Optical Tweezers 5

1.4 The Need for Plasmonic Tweezers 7

1.5 Optical Tweezers in Single Molecule Protein Studies 14

1.6 The Research Questions 16

1.7 Contributions to Publications and Submitted Manuscripts 18

2 Theoretical Background **20**

3 The PP2A Assembly and Techniques for Studying Protein Interactions 26

3.1 Introduction 26

3.2 The Protein Phosphatase 2A (PP2A) 26

3.3 Survey of Selected Techniques for Studying Protein Conformation and Interactions 31

3.3.1 Equilibrium Dialysis 31

3.4 Photoaffinity Labeling 34

3.5 Radio Labeling 38

3.6 Fluorescence Correlation Spectroscopy 38

3.7 Single Molecule Fluorescence Energy Transfer 39

3.8 Single Molecule Force Spectroscopy 39

3.9 Nanopore Electro-Osmotic Trap (NEOtrap) 39

3.10 DNH Optical Tweezers 40

4 Colloidal Lithography Fabrication of Plasmonic Double Nanohole Apertures 41

4.1 Introduction 41

4.2 Colloidal Lithography 41

5 Self-Induced Back-Action for Aperture Trapping: Bethe-Rayleigh Theory 48

5.1 Introduction 48

5.2 SIBA in Optical Trapping Theory and Practice 48

5.3 Bethe-Rayleigh SIBA theory 49

5.4 Numerical Simulations 56

5.5 Discussion 59

5.6 Conclusion 61

6 Impact of Mutations on PR65 Shape Using DNH Optical Trapping Signals..... 62

6.1 Chapter Overview 62

6.2 Introduction..... 62

6.3 Hypothesis..... 65

6.4 Methods..... 66

6.5 Results, Analysis and Characterization of PR65 and its Variants 71

6.6 Conclusion 77

7 Diverse PP2A Scaffold Dynamics Observed Directly by Nanoaperture Optical Tweezers..... 80

7.1 Chapter Overview 80

7.2 Introduction..... 81

7.3 Methods..... 82

7.4 Results and Discussion 83

7.5 Summary and Conclusion..... 89

8 Conclusion 90

Bibliography 92

Appendix A. MATLAB Code for Computing The PSD..... 122

Appendix B. MATLAB Script for Plotting The PSD ...…….125

Appendix C. MATLAB Code for Computing The RMSD ..…….126

Appendix D. MATLAB Script for Plotting The RMSD ……...131

Appendix E. MATLAB Script for Plotting The Trapping Data Vs Time ……....132

List of Tables

Table 6.1: Mean corner frequencies and normalized RMSDs for PR65 wild type (WT) and mutants. 74

Table 6.2: Mean count lengths of PR65 WT and mutants from molecular dynamics simulations Source: Mert Gur, Istanbul Technical University, Turkey and University of Pittsburgh, USA. 75

List of Figures

Figure 1.1: Timeline of the development of plasmonics. …… . 13

Figure 2.1: Trapping signal of PR65 showing double jump S0 to S1 and then S1 to S2 due to electrostriction-induced conformational change. …… 25

Figure 3.1: An α-helix and (b) a β-sheet. Purple balls represent R groups, grey balls represent Carbon atoms, blue balls represent Nitrogen atoms, red balls represent oxygen atoms and white balls represent hydrogen atoms. Copyright: Freeman & Company, W & H, New York. 27

Figure 3.2: Cartoon illustration of the PP2A Assembly showing the A, B and C subunits. Source: Adapted from [154] Copyright: Freeman & Company, W & H, New York..... 29

Figure 3.3: Illustration of Equilibrium Dialysis. Copyright: Havard Apparatus. 33

Figure 3.4: Schematic of PAL workflow. Copyright: Future Science Ltd. 37

Figure 4.1: Array of nanoapertures on a glass substrate made by colloidal lithography.. 44

Figure 4.2: A double nanohole isolated from Fig. 4.1 44

Figure 4.3: Process flow for making DNHs by colloidal lithography. A. Drop-coating glass with colloidal solution. B. Evaporating water from drop-coated glass and coalescence of polystyrene beads. C. Plasma etching. D. Titanium/Gold deposition. E. Sonication. F. Finished sample of nanoapertures in gold-on-glass showing single nanoholes (SNH), double nanoholes (DNH) and triple nanoholes (TNH). Even more

complex composites like quodroples and higher occur, but with increasing rarity, in real samples [92]. 45

Figure 4.4: Signal for PR65 trapped with a DNH made by colloidal lithography..... 46

Figure 5.1: Geometry of an aperture in a metal film interacting with sphere with light incident from the opposite side. ……50

Figure 5.2: Transmission through aperture calculated with Bethe-Rayleigh theory, normalized to transmission without SIBA. Theoretical result and FDTD simulation shown. Copyright: Optica Publishing Group. ……...54

Figure 5.3: Difference in trapping potential of aperture with and without SIBA calculated with Bethe-Rayleigh theory (black), and for the FDTD simulations with and without SIBA (green). Copyright: Optica Publishing Group…….55

Figure 5.4: yz-section of simulation setup. Copyright: Optica Publishing Group ….....57

Figure 5.5: (A) Distribution of $\left|\vec{E}\right|^2$without SIBA. (B) Distribution of $\left|\vec{E}\right|^2$wit SIBA. (C) Distribution of $\left|\vec{H}\right|^2$without SIBA. (D) Distribution of $\left|\vec{H}\right|^2$without SIBA. Copyright: Optica Publishing Group ...……58

Figure 6.1: A. Clean glass microscope slide. B. Image spacer. C. Test tube containing solution of PR65 in phosphate-buffered saline. D. Micropipette. E. DNH in gold. F. Microwell. H. Introducing 10 µL of 10 µM dilute PR65 solution into microwell using a micropipette. I. 10 µL of 10 µM dilute PR65 solution in microwell. J. Inverting DNH

over microwell to seal it off chamber. K. Completed sample ready for placement on sample stage for trapping experiment. 67

Figure 6.2: Schematic of experimental setup. WLS is a white light source; DM stands for dichroic mirror; APD stands for avalanche photodiode; L is a lens; MO stands for microscope objective; S is the sample; OIO stands for oil immersion objective; SS is the sample stage; CAM is a camera; M stands for mirror; BE is a beam expander; HWP is a half wave plate; LP is a linear polarizer; OI is an optical isolator. Top left inset shows the diffraction pattern seen when the laser is focused through the sample while center right inset shows how the laser light is focused through the sample by the OIO and collected by the MO. Throughout, magnifications are shown by the × symbol followed by a number to the left of an objective, e.g., ×10 MO indicates a microscope objective with a magnification of 10. 70

Figure 6.3: Tetherless aperture-based nanoplasmonic tweezers enable characterization of the structural dynamics of PR65 and single-site mutants. (A) PR65 undergoes a characteristic step as it enters the double nanohole trap, followed by an increase in noise from Brownian translational motion. (B) A histogram of this noise (transmission through the aperture, T, normalized to the pre-trap level) sampled after the trapping event. (C) The power spectral density from the detected transmission of PR65. (D) Root-mean-square deviation and (E) corner frequency of the amplitude of the noise for WT PR65 and the six mutants. (F) The mean end-to-end distance observed across 1.5 μs of molecular dynamics simulation for WT PR65 and the six mutants report a Pearson correlation coefficient of -0.83 with the normalized RMSD. 73

Figure 7.1: Optical trapping with DNH. a. Optical setup schematic showing laser focused onto sample and collection. b. Representative scanning electron microscope image of a DNH. ……....83

Figure 7.2: PR65 WT trapping event with regions highlighted in color: Untrapped (pink, I), sharp dip (yellow, II), intermediate step (green, III), final step (orange, IV) ……88

Figure 7.3: Power spectral density plot of trapping signal from DNH showing Lorentzian characteristic typical of weak optical traps. ……..... 86

Figure 7.4: PR65 WT and mutants. a. Intermediate step times (colored circles) and mean values (black squares) for PR65 WT and mutants versus relative stability. b. Trapping event of mutant L197V, scaled to show long intermediate step. c. Trapping event of mutant D315E, scaled to show telegraphing behavior (upper) and scale zoomed to show intermediate step (lower). 88

Acknowledgments

Firstly, I would like to thank my Supervisory Committee – Dr. Reuven Gordon, Dr. Rustom Bhiladvala and Dr. Thomas Darcie. Dr. Rustom Bhiladvala's wise counsel, calming influence and probing questions were immeasurably vital to me locating the niche of this work and persisting through with it. Dr. Thomas E. Darcie's thoughts were instrumental to clarifying my ideas and being able to explain this work clearly and concisely. His constant reminder that I was doing this for me and no one else was crucial to me not throwing in the towel when it seemed that I was getting nowhere with this research. My supervisor, Dr. Reuven Gordon, deserves special thanks: he went out of his way to help me complete this work. I am grateful for his patience, understanding and support materially, intellectually, and otherwise. He was particularly generous with his time and made himself more available than I would have hoped from anyone as busy as he was, and without his guidance, belief and enthusiasm I could not have succeeded.

I am also grateful to the University and to the Department of Electrical and Computer Engineering for the 2-year fellowship that I received toward this research. My gratitude likewise goes to staff of the CAMTEC facility for their invaluable assistance in the course of my research. I am similarly grateful to the Abia State University, Uturu, Nigeria and to the Tertiary Education Trust Fund (TETFund) of Nigeria for financial support toward my PhD.

I remain indebted to my long-time mentor Dr. (Mrs.) J. N. Ogwo who started me on this journey, and whose philosophy was invaluable to me through the dark times. I am

particularly grateful for her understanding while I was distracted and disconnected from her. I hope to have time now to reconnect with everyone.

I want to also acknowledge the encouragement and assistance in various ways of members of my lab group, particularly Dr. Demelza Wright, Dr. Ali Khademi, Dr. Ghazal Hajisalem, Dr. Jamal Etiaba, Dr. Mirali Shariatdoust, Mr. Ardash Ravindranath and Dr. Zohreh Sharifi.

Thanks also to my wonderful and life-long friend, Kenneth, for his kind support and encouragement, and to my amazing parents, and very kind and supportive mother-in-law, without whose belief, support and encouragement I could not have pulled this off.

Finally, to my wife, Precious, and my kids, Avis and Max: your love, support and understanding were the beacon of hope through the somber moments of my studies. You were my strength in weakness, the loving shoulders of reassurance when I needed some to lean on; you were the voices that kept telling me that I could yet make it when it seemed that I could not. Without a doubt, you earned this degree along with me, and it is time to celebrate.

Dedication

To my wife, Precious, and kids, Avis and Max.

Chapter 1

Introduction

1.1 An Overview of Plasmonics

As the title of this dissertation suggests, the plasmonic effect is at the root of the physics of the primary tool employed for the research presented in this dissertation. It is thus fitting that the report begins with an overview of this concept to make for an easier and robust appreciation of the results obtained in the study via the exploitation of the plasmonic effect.

The field of nanoplasmonics is a relatively new one [2], [3], [4], the term plasmonics having only been coined in 2000 by the research group of Harry Atwater [2]. Like most other fields of human endeavor, however, the early origins of nanoplasmonics go further back, beginning with the work of Michael Faraday with thin gold leaves and colloidal gold particles in 1856 [5]. Similarly, the theoretical groundwork needed to understand the underlying phenomena of nanoplasmonics was established by Gustav Mie back in 1908 [6], [7]. Nanoplasmonics relies on the coupling between electromagnetic fields and the collective oscillations of delocalized electrons at the interface between a metal and a dielectric, where the real part of the dielectric constant changes sign. This coupling between electromagnetic fields and the collective oscillations of delocalized surface electrons is known as a surface plasmon polariton (SPP) when it occurs at an interface between a metal and dielectric and as a localized surface plasmon (LSP) when it occurs on the closed surface of a small nanoparticle [8], [9], [10], [11]. The existence of surface plasmons was first predicted by Ritchie in 1957 [12] and observed by Swan and Powell in 1959 [13], [14]. But the concept of surface electromagnetic waves in general was introduced by Zennech in 1907 in the context of radio waves [15], with further theoretical support by

Sommerfield's 1909 work on guided electromagnetic waves along a thin wire of finite conductivity [15], [16]. The field of plasmonics has rapidly evolved since then leading to a myriad of applications in agriculture [17] medicine [18], [19], [20], light technologies [21], [22], [23], [24], sensing [25], [26], energy [27], [28], [29], and research [30], [31], [32], [33], [34], [35].

1.2 Surface Plasmons and the Extraordinary Transmission of Light through Periodically arranged Subwavelength Apertures

A metal contains a sea of electrons. Just like a wave is created in a sea of water by disturbing its surface, a wave of electrons is created in a metal when, say, a beam of light or other electrons with the right energy and momentum is incident on a metal. This wave of electrons in a metal is known as a plasmon. Plasmonics is the study of this electron wave. The history of the development of plasmonics is a lengthy one involving contributions by many researchers at different times since Ritchie, Swan and Powell [5]. Space will not permit us to discuss the contribution of every one of these researchers. More pertinent to the present discussion is the work done by Ebbesen *et al*. on the extraordinary optical transmission through subwavelength metal apertures [5], which followed the works by Andreas Otto, Erich Kretschmann and Heinz Raether, who demonstrated the excitation of surface plasmons on metallic films using light in lieu of electrons, thereby making both the generation of plasmons and experiments on plasmon related effects handy to many more researchers [5]. To lay a foundation for understanding the phenomenon of extraordinary transmission through subwavelength apertures, however, we must now discuss surface plasmons. This is frequently a difficult concept to understand for people who are new to the field of plasmonics because they have a difficulty understanding how light can propagate parallel with the direction of a surface charge that the light either excites or is

emitted by since light is a transverse wave [36], [37], since this suggests an electromagnetic wave having its propagation vector and polarization collinear. The true picture, though, is that the exciting light field does not propagate either along or against the direction of oscillation of the surface charges. It is, instead, the electric field (or polarization) of the exciting light which lies parallel or antiparallel with the oscillation of the surface charges, and it is not difficult to see how light, even propagating on the same surface that it excites oscillating charges on, can satisfy the transverse condition.

Furthermore, the electric field of the exciting light causes charge separation on the surface, so that there exist alternate regions of positive and negative charges on the surface which change in density and switch sign over time as the electric field goes through a cycle changing its amplitude and flipping sign. This is like having a continuum of oscillators on a surface, where each oscillator is a 'charge amplitude' that could take on a value -q or +q as the oscillator goes through a cycle in time. The wave which results from such a collection of surface charge oscillators will have both a wavelength and a frequency like any other wave, with the frequency determined by the excitation source (exciting light field) and the wavelength by the medium in which the wave propagates. Different from the exciting light for the surface charges, however, the 'light' which is inherently associated with the surface charge density wave (surface plasmon) is just a quantity related to the square of the modulus of the electric field of the charge distribution – not an actual propagating light field as the surface plasmon does not couple to radiative modes. The field decays exponentially into the adjoining medium with its maximum on the surface and has a characteristic length given by $\frac{1}{\delta_{zi}} = \frac{\omega}{c} Im\left[\frac{\epsilon_i^2}{\epsilon_d+\epsilon_m}\right]^{1/2}$, where δ_{zi} is the characteristic length of the surface plasmon wave in the medium i, $i = d, m$, with d standing for dielectric and m standing for metal, ω is the angular frequency of the exciting electromagnetic

radiation, c is the vacuum speed of light, ϵ_i is the permittivity of medium i, while ϵ_d and ϵ_m are, respectively, the permittivities of the dielectric and metallic media. $Im[\cdot]$ represents the imaginary part of the expression within the brackets. The 'light' in surface plasmon effects is thus confined tightly to the surface on which the plasmon propagates. It is therefore an example of a surface mode which does not radiate into space [3], [38].

While studying the optical properties of metallic films on which subwavelength cylindrical apertures had been fabricated, Ebbesen *et al*. [39] observed an unusual zero order spectra through the array of cylindrical apertures which did not match what was expected for diffraction from such apertures. For example, there were large peaks at wavelengths larger than the diameter of the cylinders when there should have been no peaks at all. Furthermore, the absolute transmission efficiency (the ratio of optical power transmitted through the aperture to the area taken up by array of holes [39]) measured at those peaks was greater than 1, with the order of magnitude of the absolute transmission efficiency also been larger than standard theory would predict. Consequently, Ebbesen *et al*. attributed their observation to the excitation of surface plasmons on the periodic metal film, which in turn coupled to radiating modes either by evanescent tunneling or by scattering off roughness on the surface. This was based on a couple of observations. The first was the conspicuous absence of the observed anomalous transmission spectra for an array of holes fabricated in germanium films, which highlighted the importance of the metal on which the arrays were fabricated. The second was that the dependence of the transmission spectra of the holes fabricated in the metal samples on the angle of incidence matched that of light coupled with surface plasmons in reflection gratings. In a later experiment, Ghaemi *et al*. would find their measurement in good agreement with calculations assuming

coupling with plasmons on the interface of the metal in which the subwavelength cylindrical apertures were fabricated [40].

Relevant to this work though is the enhancement that results from the self-induced back-action (SIBA) effect rather than the phenomena of extraordinary transmission through periodically arranged subwavelength plasmonic nanoapertures. The discussion of the extraordinary transmission of light through periodically arranged subwavelength nanoapertures is just to provide an overview of the rich phenomena observed in plasmonics, some which find applications in very critical fields such as biochemistry and biomedical research as we demonstrate in this work.

1.3 The Beginning of Optical Tweezers

Arthur Ashkin articulated the principles of optical trapping in the 1970's [41]. In 1986 he demonstrated the first successful trapping of small dielectric spheres using a highly focused laser beam [42], [43], [44], [45]. He termed the device so used an optical tweezers to describe its ability for picking up and moving objects. The working of the conventional optical tweezers invented and used by Arthur Ashkin and a host of other researchers after him is briefly discussed in what follows. The limitations of such an optical tweezer are also discussed, followed by a discussion of the plasmonic double nanohole (DNH) optical tweezers and how it overcomes the inherent limitations of the conventional optical tweezers. Briefly, two forces, namely a scattering force and a gradient force, are always present at any point within a beam with a non-uniform spatial profile such as found in an optical tweezers [46], [47], [48]. These forces, while not collinear, act contrary to each other, with the scattering force in particular being a nuisance in single beam gradient traps [49], [50], [51], [52], [53], [54], [55]. The principle differ slightly depending on whether the size of the particle being trapped is larger than the wavelength of the

light employed in the optical tweezers (Mie regime) or smaller than this wavelength (Rayleigh regime) [51], [53].

The theory describing the optical tweezers effect in the regime between the aforementioned extremes is complicated and requires a first principle solution of Maxwell's equation with appropriate boundary conditions [56], [57], [58], [59], except when the difference in the refractive index of the particle involved and that of the embedding medium is negligible [60], in which case the formulation in the Rayleigh regime can be quite simply generalized to account for the forces in the optical tweezers in this general case [61].

In the Mie regime, the change in momentum when rays of the light used refract through a particle gives rise to the scattering force and the gradient force. Diffraction effects can be ignored if the ratio of a particle's refractive index to that of its embedding medium is greater than 1, which is the case in the majority of situations encountered in optical trapping [42], [47], [62]. In the Rayleigh regime, a particle simply behaves as a collection of induced dipoles polarized by a spatially slow varying electric field. Going through the formulation, one finds that the energy of the field is proportional to the negative of the squared magnitude of the local field intensity. Since the squared magnitude of the local electric field intensity is proportional to the light intensity over the particle, it is understandable that gradients in the intensity of the trapping light would give rise to forces on the particle, which can be found by taking a gradient of the filed energy. A particle with an index of refraction greater than its surrounding medium, such that its specific polarizability is positive, will experience a force of attraction toward the focal point of the trapping beam where the intensity is highest, and the field energy is minimum. A scattering force – which is destabilizing for trapping – also arises from radiation pressure, and thus a highly

focused beam is often required to increase the gradient force significantly above the scattering force, achieving stable trapping [42], [47].

1.4 The Need for Plasmonic Tweezers

So far, that is how the story goes for conventional optical tweezers. But useful as they may be – for example, Arthur Ashkin who invented the technology in 1986 and demonstrated its usefulness for manipulating bacteria and viruses in [63] was awarded the Nobel Prize in 2018 [64] – conventional optical tweezers come with a caveat in the form of two difficulties which arise when trying to use them to optically trap very small particles.

First, the gradient force that pulls the particle into the trap is scaled by the cube of the particle's radius. For very small particles, therefore, a higher intensity gradient is required to counter the effect of this scaling. This can be done in one of two ways. The incident light could be focused down to a smaller spot or the peak intensity of the input light could be raised. How tightly the input light can be focused is limited by diffraction, so for really small particles this may be impractical as we may need to focus below the minimum spot size allowed by diffraction to achieve trapping, which is simply impossible, leaving the only viable option to be to raise the peak intensity of the input light high enough to attain a sufficient gradient force to be able to trap such particles. Second, for stable trapping, we need the potential of the gradient force to exceed the thermal energy of the particle to be trapped to guarantee that the particle will be pulled into the optical trap faster than it can diffuse away from it by Brownian motion [42] – aided by the decrease in viscous drag with decreasing particle size [65]. But very small particles can attain incredible speeds even for moderate thermal energies, so again we must raise the peak intensity of the input light – on which the potential of the gradient force depends [66] – high enough to

achieve this. In general, therefore, conventional optical tweezers require high intensities for trapping very small particles.

Now, exposure to high intensities can heat the particles even more, requiring even higher intensities to achieve stable trapping and more heating still. For biological samples, which can easily be damaged by such heat [67], this is simply not good, hence the need for plasmonic nanoapertures, since the local field enhancement of these apertures can be exploited to increase the gradient force significantly for moderate light intensities [68].

Although these tweezers do not benefit from the phenomenon of extraordinary transmission (EOT) discovered by Ebbesen *et al*. for periodic arrays of nanoapertures discussed earlier [69], [70], [71], [72], [73], they still take advantage of an enhancement in the transmission through the DNH aperture owing to a different effect known as the self-induced back-action (SIBA) effect [74], [65], whereby particles in the DNH aperture play an active role in their own trapping in such a way that both the transmission through the DNH aperture and the trapping potential are enhanced. Add this to the considerable enhancement of the local field in these plasmonic aperture tweezers due to the plasmonic effect discussed previously, and what one gets is a considerable reduction in the input light intensity required for optical trapping with plasmonic aperture tweezers.

Plasmonic enhancement is the result of energy conservation in plasmonic systems in general. The energy of an optical field is resonantly transferred to the conduction electrons in these systems. Owing to the optical properties of plasmonic systems, they necessarily span very small regions of space – typically of dimensions much smaller than the wavelength of the exciting radiation. Storing the energy of the original optical field in the much smaller space occasioned by

the physical dimensions of plasmonic systems results in much higher fields – which is the origin of the plasmonic enhancement in plasmonic nanoapertures.

These apertures can exhibit resonances – different from the plasmonic resonance of the metal they are made from – because of their geometry and the laws of electromagnetic interaction.

There are at least two competing explanations for the autonomous feedback which the dielectric property of a trapped particle provides in a plasmonic aperture tweezer by way of the SIBA effect.

In the first due to [65], the effect derives from the difference in momentum change corresponding to differences in transmission through the particle in and out of the trap location. A particle outside the trap location transmits light equally in all directions. As such, the net momentum from its transmission is zero. However, the incident light impinging on it exerts a force on the particle in the direction of propagation. Accordingly, the total momentum change – and hence the force on a particle due to scattering outside the trap location – is along the direction of propagation of the incident light. If a particle is in the view of an aperture, the scattering force pushes it downstream into the trap location. However, for a particle in the trap location, the aperture's directivity forces the particle to transmit over a very narrow angle, so that it experiences a net upstream recoil force due to the change in momentum resulting from light transmission (refraction) through it – amplified if the particle has a higher refractive index than its surrounding medium, which can be understood on account of Bethe's aperture theory, since the transmission, T_0, through the aperture goes from $T_0 = (r/\lambda)^4$ in the absence of the particle to $T = (r/\lambda/n)^4 = (nr/\lambda)^4 = n^4(r/\lambda)^4 = \mathrm{n}^4\mathrm{T}_0$ in the presence of the particle, where r is the radius of the particle, λ is the vacuum wavelength of the trapping laser light and n is the index of refraction of the trapped particle. This dielectric loading makes the aperture effectively larger

[65]. This force balances out the force due to the incident light impinging on the particle and prevents the particle from leaving the trap downstream of the incident light beam. The SIBA effect thus turns the vexatious scattering force into an advantage, exploiting it to provide an additional vertical confinement of the trapped particle.

With the scattering force mostly cancelled out through SIBA, the constraint on the magnitude of the gradient force is also lifted, resulting in less intensity of the input light being required to achieve a stable trap – bar of course the thermal energy of the particle which, in most cases, the metal part of the aperture handles through conduction and radiation. In the other explanation [75], [76], [77], the SIBA effect arises from the coupling of the trapped particle's motion with the resonance of the nanoaperture in that the position of the trapped particle alters the resonance frequency of the aperture so that it is possible to control the gradient force experienced by the particle using the frequency of the input light in lieu of its intensity, thereby allowing stable trapping at lower intensities. Unlike the previous explanation, however, this latter explanation does not describe any features that ensure the maintenance of stable trapping against perturbations.

All these effects then put together enable stable optical trapping of particles at much lower input powers using nanoplasmonic apertures when compared with conventional optical tweezers. But while these advantages are shared to varying degrees by different types of plasmonic nanoapertures such as bowtie, nanoring, ring slits, single holes, double holes, *et cetera* [74], [78], [79], [80], double nanoholes (DNH) are relevant to the work presented here and would be discussed exclusively in what follows.

The use of plasmonic nanoapertures for optical trapping was first suggested by Okamoto and Kawata in 1999 [81]. This was followed by a similar and independent suggestion in 2004 [82]

and the first successful trapping with a plasmonic nanoaperture in the same year [83]. This experiment demonstrated the use of single plasmonic nanoapertures of 500 nm diameter to trap 200 nm latex beads.

The use of such an apparently large aperture (on the nanometric scale), however, fails to take full advantage of the plasmonic enhancement available through spatial reduction, and hence could not be used for trapping smaller particles without increasing the input photo power to the level required in conventional optical tweezers [65]. One way to overcome this would be to reduce the aperture size much further using a technique such as focused ion beam milling, for example, [84]. However, the symmetry of the aperture would still prevent the harnessing of the SIBA effect so that, again, stable 3-dimensional confinement can only be achieved at high input light intensities that increase inversely with particle size [65]. Furthermore, DNHs can be engineered to maximize the signal-to-noise ratio of the optical trapping signal through enhanced transmission [85]. It is not clear when the plasmonic DNH aperture was first used or who invented it or first investigated its properties. The 2009 article by Juan *et al.* seems to suggest that it might be the first to describe the double nanohole aperture and to investigate its resonances. This suggestion would seem to be corroborated by other publications such as [80], [74], [75] and [77], but in another article [85] from 2007 double nanohole arrays in gold film were used for enhanced Raman spectroscopy, and Iyer *et al.* [86] also studied the double nanohole aperture independently in 2009. There is also a publication [87] of a 2006 numerical investigation of the optical field enhancement of an array structure of DNH apertures. Apparently, it seems safe to conclude that the DNH aperture has both been studied and used in optical tweezer experiments prior to 2009, but that its resonances were probably elucidated about this time.

Plasmonic double nanoholes have several advantages as optical tweezers. Surface plasmon effects on the surface enhance the gradient force needed to pull particles into the cusp of the double nanohole, where the lightening rod effect [88] and the gap plasmon resonance effect [68] together give rise to strong fields in the gap between the cusps of the DNH for confining trapped particles. All these can be achieved at very reduced trapping light intensities. The double nanohole makes it easy to maximize the latter effect in particular by minimizing the width and length of the cusps. An additional wedge plasmon resonance [68] also improves optical trapping with plasmonic double nanoholes while the SIBA effect enables a reduction in the optical intensity used for stable trapping in double nanoholes. Double nanoholes can be fabricated in a number of ways including focused ion beam milling [89], [90], electron beam lithography [91], [92], [93], template stripping [94], [95], and colloidal lithography [96], [97], [98], [99], [100]. The fabrication of double nanoholes by colloidal lithography was employed in this work and will be discussed in more detail subsequently.

The power of plasmonic double nanohole optical tweezers is demonstrated in their successful utilization in trapping dielectric particles as small as 12 nm [65]. In this work, the ability of plasmonic double nanoholes to exert electrostrictive forces of hundreds of piconewtons [101], [102] is exploited to study the conformational changes of PR65 – the 65 kDa structural subunit of protein phosphatise 2A [103]. The study is based on two very fundamental premises – the light scattered by a physical object is dependent upon its geometry [104], [105]; all dielectric materials, but especially soft dielectric materials, exhibit electrostriction – that is, are mechanically deformed when exposed to an electric field [106], [107]. It should, therefore, be possible to probe the electrostriction-induced change in conformation of a particle such as a protein molecule by observing the scattering from such a particle as a function of time.

The non-requirement of tethers and labels [108] – which may otherwise influence the result of such studies in unknown ways, impacting reliability, or complexify experimental design in a bid to eliminate any likely influence by labels or molecular tethers or both and so increase reliability [109] – together with the excellent spatial and temporal resolution [110] make optical tweezers a choice tool for this type of studies. Indeed, many previous studies such as [46], [110], [34], [33], [96], [32] among others have all demonstrated the power of optical tweezers for single molecule studies.

The historical timeline sketched out here of the development of plasmonics is illustrated summarized in Fig. 1.1 below.

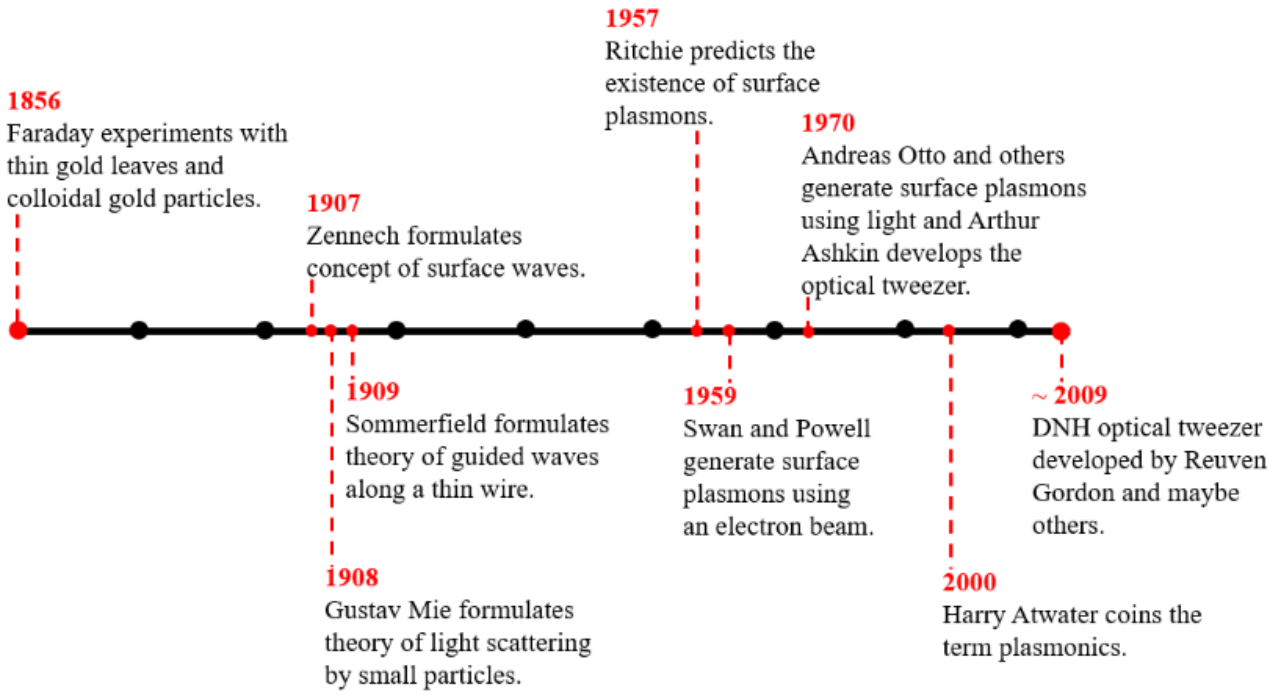

Figure 1.1: Timeline of the development of plasmonics.

1.5 Optical Tweezers in Single Molecule Protein Studies

Following the successful demonstration by Arthur Ashkin of the trapping and manipulation of small particles such as viruses and bacteria using optical tweezers [63], researchers soon adapted it for other purposes such as studying single molecule proteins and their interaction with other molecules such as DNA [111]. The first single molecule proteins studied using optical tweezers were molecular motors such as kinesin [112] and myosin [113]. These seminal works demonstrated the spatio-temporal sensitivity of optical tweezers in tracking minuscule movements at the single digit nanometric scale, just as a decade later the capability of optical tweezers for studying the mechanism of pausing in DNA transcription was demonstrated by Neuman *et al*. [114].

These early experiments used conventional optical tweezers, however, and the relatively large trap volumes of these tweezers meant that isolating single proteins for study using them required the use of specially treated tethers in the form of micron-sized beads coated with biotin, for example, to which single protein molecules were then attached, or the use of labels that allowed single molecules to be tracked within the relatively large trap volumes of the optical tweezers that contained many such molecules or both, increasing both cost and complexity [115]. For the same reason, these experiments required the purest of samples.

The advent of nanoplasmonic tweezers, however, enabled a significant reduction in trap volume such that single molecules could be conveniently isolated within the nanoplasmonic tweezers at a time, thereby eliminating the need for both tethers and labels as well as the need for highly purified samples [116]. The first single molecule studies conducted using a plasmonic nanotweezers was in 2012 [33]. In that study the interaction of DNA with wild and mutant tumor suppressor protein p53 was investigated, resulting in the quantification of the unzipping energy

of a DNA hairpin using a plasmonic double nanohole optical tweezers. If this was a landmark achievement, what came the following year was nothing short of spectacular. In 2015 Wheaton *et al*. [117] determined the Raman spectrum of the proteins Carbonic anhydrase and Conalbumin using the plasmonic double nanohole aperture in a study that has been acclaimed to be the "first clear evidence of protein acoustical modes of globular proteins" [118]. Double nanohole aperture tweezers have also been used to size proteins [119], [120].

Other techniques such as nanopore electro-osmotic trap (NEOtrap) [121] and light interference scattering (iSCAT) [122], [123], fluorescence spectroscopy [124], and nanopore electrophoresis [125] have also been used for single molecule protein studies much like the plasmonic double nanohole aperture [33], [116]. However, their use has been limited to single molecules of sizes no smaller than 50 kDa, whereas the DNH aperture has been used to reliably characterize single molecules down to 6.5 kDa [116]. Furthermore, compared to these other techniques, the plasmonic double nanohole aperture seems to have a superior resolution and sensitivity for single molecule studies [116]. For example, one study [126] combined the nanopore approach with the plasmonic double nanohole aperture technique for characterizing antibody-ligand interactions and revealed a superior sensitivity and resolution capability of the DNH technique compared to the nanopore approach. The choice of the DNH for the current study is informed by this attested superiority of the DNH over these other techniques with respect to single molecule studies.

However, while the foregoing studies have shown the utility of the DNH aperture for studying protein conformation [115], sizing proteins [119] and studying the interaction of proteins with other molecules [127], [33], [111], [126], here the power of DNH optical tweezers in resolving single point mutations and their effect on protein stability and dynamics is demonstrated for the first time, helping to unravel the intricate mechanisms of protein dynamics and its potential for

insightful applications in molecular biophysics; and it is in this regard that the current study not only differs from what has come before, but also goes one step further to do something novel with this amazing and powerful analytical tool. An overview of the current research and its implications will be discussed in the next section.

1.6 The Research Questions

Protein phosphatase 2A (PP2A) is a tumor suppressor protein [128]. Its function is thought to be regulated by its Aα subunit, also known as PR65, by the latter acting as an elastic bridge which deformation controls the opening and closing of the binding and catalysis sites of the PP2A assembly as well as by altering the positions of some of its catalytic residues [103]. PR65 has, furthermore, been implicated in a number of cancers [129], [130] as well as Alzheimer's disease [131], [132]. PP2A has also been investigated for inhibiting the proliferation of cancer by inhibiting the production of proteins that drive the growth of cancer cells [128]. It was found that certain substances called small molecule activators of PP2A, or SMAPs for short, activate PP2A by binding to PR65 to produce conformational changes that enable PP2A to suppress the production of cancer signaling proteins [128]. It follows that PR65 is both of interest by itself and for the role that its elastic behavior, which derives its conformational dynamics, plays in the functioning of the PP2A assembly. However, various mutations of PR65 have been implicated in altering PP2A activity [133], [134], [135], and it is important to investigate the impact of this mutations on the conformational flexibility of PR65 through its elastic behavior, which has so far only been studied numerically [103]. The aim of the current study is to investigate the impact of point mutations on the conformational dynamics of PR65 using optical tweezers, which have emerged as a powerful tool for probing the biophysics of proteins at the molecular level [136], [137], [127], [110]. In particular, the study will show the utility of enhanced field confinement

and sensitivity of aperture-based nanoplasmonic tweezers for studying the structure and dynamics of single proteins. Unlike conventional optical tweezer approaches, this approach allows for characterization of individual unmodified proteins in solution for extended durations without the need for tethers or labels [136]. The study will proceed by investigating the underlying physics of nanoaperture tweezers, and then comparing the DNH as a tool for probing single molecule protein dynamics with other techniques commonly employed for studying protein characteristics [138], [119], protein interactions [136], [127], and protein conformational dynamics [139], [121].

The following very important questions are examined in this study:

(a) How does a dielectric nanoparticle interact with a nanoaperture, and could this be exploited to study protein conformation changes using aperture tweezers such as the DNH aperture tweezer?

(b) What can be said of the behavior of PR65 when trapped in a DNH aperture tweezer, and can this be explained in terms of how PR65 interacts with the DNH aperture?

(c) What is the impact of point mutations on the conformational dynamics of PR65 trapped in a DNH aperture tweezer?

Steps taken to address these questions are discussed in subsequent chapters, as is a brief account of techniques commonly employed in studying proteins interactions and dynamics other than optical tweezers and how they compare to the method employed in the current study.

The outcome of this study is relevant to research and biomedical communities, whether as biophysicists, biochemists, oncologists and so on, who may find it useful to use protein conformational dynamics as a biomarker for studying, identifying and tracking mutations, whether at the DNA level leading to the coding of mutant proteins or at the protein level, by

either directly using the technique developed in this study for PR65 or by adapting it for their purposes.

1.7 Contributions to Publications and Submitted Manuscripts

During the study that culminated in this dissertation report, the author contributed two published works and two submitted manuscripts (as at the time of writing). This section provides details of these various contributions. The author of this dissertation report was coauthor of *Colloidal lithography double-nanohole optical trapping of nanoparticles and proteins, Opt Express, 27 (11), 16184 – 16194,* 2019 together with Adarsh Lalitha Ravindranath, Mirali Seyed Shariatdoust, the author of this dissertation report and Reuven Gordon. The contribution of the author of this dissertation report to that work included computation of the approximate concentration of polystyrene solution to use for maximizing the number of DNHs on a surface, production of some of publication figures such as the workflow diagram and the experimental setup, and participation in the deposition and imaging processes. Coauthored with Reuven Gordon, the author of this dissertation report is the first author of *Self-induced back-action for aperture trapping: Bethe-Rayleigh theory, Opt Express 31 (26), 44190 – 44198, 2023*. The author of this dissertation's contribution to this latter work included some of the theoretical derivations for the publication, all the numerical computations, all the publication's figures and writing the theory, simulations and discussion sections of the publication's manuscript. The author of this dissertation is also joint first author with Anupam Banerjee of the manuscript on *Influence of Point Mutations on PR65 Conformational Adaptability: Insights from Nanoaperture Optical Tweezer Experiments and Molecular Simulations Impact of mutations on PR65 conformation adaptability (2023) (manuscript number: adn2208)* submitted for publication to Science Advances. To this the author of this dissertation report contributed the optical tweezer

experiments, the analysis and interpretation of the results of the optical tweezer experiments, production of publication figures for the optical tweezer section of the results and methods sections of the submitted manuscript and writing up the methods, results and discussion sections of the submitted manuscript that pertain to the optical tweezer experiments. Finally, the author of this dissertation report is coauthor with Veerpal Kaur and others of the manuscript on *Portable fiber-based double nanohole optical tweezer for trapping small proteins (2024) submitted to J. Phys. Photonics (manuscript reference: JPPHOTON-100588),* to which the author of this dissertation report's contribution was the provision of data from trapping using stand-alone DNH optical tweezers for comparison with similar data from trapping using fiber-based DNH optical tweezers.

Chapter 2

Theoretical Background

In this chapter we present the theoretical background to this work. These are the tools required by the reader to understand the work. It was earlier stated that the study is based on two very fundamental premises, namely that the light scattered by a physical object is dependent upon its geometry [104], [105] and that all dielectric materials, but especially soft dielectric materials, exhibit electrostriction – that is, are mechanically deformed when exposed to an electric field [106], [107]. It was then averred that, based on these simple but far-reaching premises, it should be possible to probe the electrostriction – induced change in conformation of a particle such as a protein molecule by observing the scattering from such a particle as a function of time. We expand on this concept in this chapter.

The dependence of scattering on geometrical properties such as shape and size arises from the dependence of the specific material polarization, or the residual polarizability per unit of mass as has been theorized elsewhere [140], of particles on their shape and size [141], [142]. This dependence may be described by expressing the specific polarizability of a particle as α(g), where g is a geometric parameter of interest such as size or shape. The effect of varying this parameter on the intensity of the light scattered by a particle can be readily seen by inserting the specific material polarization above into the Rayleigh scattering formula [143],

$$I_s = \frac{\pi^2 \alpha^2}{\varepsilon_0^2 \lambda^4 r^2} I_i sin^2\theta \qquad 2.1$$

where ε_0 is the permittivity of free space, α is the specific polarizability, λ is the wavelength of the incident light, r is the distance from the location of the scatterer to the point where the scattered intensity is observed, θ is the angle of sight, I_s is the scattered intensity and I_i is the incident intensity. It can be seen from (2.1) that if g changes in such a way that α increases, then there would be an increase in the scattered intensity by the square of $\alpha(g)$. If, on the other hand, g changes in such a way that $\alpha(g)$ decreases, then the scattered intensity would decrease.

Either of these changes would be reflected as a change in the level of the scattered intensity. Now, if a dielectric particle is placed in a non-uniform electric field, it will experience a force toward the point where the electric field is most intense [46]. This is the same reason that a comb attracts bits of paper after it is used on the hair. It can be shown that the magnitude of this force is given [144] as in (2.2) below.

$$\vec{F} = (\varepsilon - \varepsilon_0) \iiint_{\mathrm{V}} (\vec{\mathrm{E}} \cdot \vec{\nabla}) \vec{\mathrm{E}} \mathrm{dV} \qquad 2.2$$

where $\vec{F}$ is the force, ε is the permittivity of the dielectric, ε_0 is the permittivity of free space, $\vec{E}$ is the electric field intensity and dV is an elemental volume. In a DNH aperture (to be discussed in more detail in Chapter 4), the electric field intensity is maximum at the tip of each of its cusps and minimum half way between the cusps [68], [145], [146]; a particle trapped in a DNH optical tweezer will therefore have its opposite ends pulled toward the cusp nearest to it. These forces will cause such a particle to elongate or unfold or straighten, depending on its shape, how these forces resolve at its ends, and the magnitude of the forces. This will alter the geometry of the affected particle, altering its size, shape or both, and therefore its polarizability and scattered intensity as in (2.1).

Particles in an optical tweezer experiment are suspended in solution and undergo Brownian motion [66], [65]. This motion is described by [66], [147], [61]

$$\dot{x} + \frac{1}{\tau_0} x = \frac{1}{\gamma} \xi(t) \tag{2.3}$$

where x is position, $\dot{x}$ is velocity, $\tau_0 = k/\gamma$, with k being the trap stiffness, is the relaxation time, γ is the coefficient of friction, t is time and $\xi(t)$ is the Brownian force, with the property

$$\langle \xi(t)\xi(t-\tau) \rangle = \delta(t-\tau) \tag{2.4}$$

for some delay τ. The implication of (2.3) is that the particle moves randomly within the potential well of the gradient force. As it moves, the angle θ in (2.1) changes, and as such the scattered intensity fluctuates randomly in the same manner as x, while the change in $\alpha(g)$ causes the scattered intensity to transition to a new level at the instant of time when the change takes place, and remains there unless the change is reversed, usually by turning off its source, if within the control of the experimenter. It should be noted that transitions in the level of scattering corresponding to changes in $\alpha(g)$ occur only after the first transition in the time trace of the scattered intensity, being that a change in $\alpha(g)$ cannot occur until the particle is trapped and well within the cusps of the double nanohole aperture, so that the aforementioned first transition in the level of the scattered intensity observed in the time trace of the scattered intensity during a DNH tweezers experiment is usually attributed to the dielectric loading of the aperture [127], [139] when the particle is just trapped. Thus, any observed transition (jump or step) in the time trace of the scattered intensity (equivalently, the trapping signal) beyond the first are due to changes in $\alpha(g)$ caused by electrostriction in the cusp of the DNH aperture.

If a mutation alters the shape or conformational flexibility or both of a protein, this will impact its polarizability in any adopted conformation following a conformational transformation in response to an axial force or forces, say, due to electrostriction in an optical tweezer, and will show up in the scattered intensity of the protein [148], which can thus be used to distinguish mutant proteins from one another and from the wild type by comparing the amplitude of the

scattered intensity of the mutants and wild type to one another. If the scattering protein molecules are undergoing random motion such as Brownian motion in a fluid environment, the scattered intensity would be modulated by this motion, and one way to represent the amplitude of the scattered intensity of the proteins in this case would be through the root-mean-squared-deviation (RMSD) of the scattered intensity [119]. Other ways would include the autocorrelation of the scattered intensity and the power spectral density of the scattered intensity [61].

This also provides a way of monitoring Protein-ligand binding using double nanohole optical tweezers, for example, since the binding of a particle, such as a small molecule activator of PP2A (SMAP), to a protein will lead to a change in $\alpha(g)$ either by changing the shape of the protein or by altering its conformational flexibility, such that it undergoes greater electrostriction resulting in a change in its shape or size or both, or by making it more polarizable so that it scatters more light, or all of this. In any one way or combination of ways that this happens, it would manifest as a transition in the time trace of the scattered intensity at the instant that such a change occurs, indicating binding, with the caveat that the conformation change due to thermo-optical forces alone is known in this case, so that the binding-specific conformation change can be extracted from the overall conformation change.

Alternatively, subject to the foregoing caveat, if, say, a protein and a SMAP are mixed and binding takes place between these, forming a composite that is then trapped, this will show up as a difference in the trapping characteristics of the composite relative to the trapping characteristics of the protein alone, for example in the standard deviation of the signal normalized to the pre-trap level. For example, if the protein-SMAP composite is made more polarizable than the protein alone, then the gradient force experienced by the protein-SMAP composite in the presence of a non-uniform electric field becomes larger than the protein alone

will experience in the presence of the same electric field. This amplification of the gradient force experienced by the protein-SMAP composite in the presence of the electric field will make it possible to trap it at a lower intensity than will be required to trap the protein alone. The protein-SMAP composite will also, according to (2.1), scatter more light than the protein alone. Consequently, by trapping just the protein and then the protein-SMAP complex using the same laser intensity, binding can be inferred by comparing the standard deviation (or root-mean-squared-deviation, RMSD) of the acquired trapping signal normalized to the pre-trap level from the two separate cases. The physical explanation for this is, of course, that the polarizability of a particle influences the tweezer potential. When a particle is trapped in an optical tweezer, it undergoes Brownian motion with an amplitude that is correlated with the intensity of the light scattered by the object. As previously mentioned, the Brownian motion induces a fluctuation in the intensity of the light scattered by the particle, with the fluctuation increasing in amplitude as the Brownian motion of the particle increases in rapidity (more about this in Chapter 6). The higher the polarizability of a particle, the steeper the tweezer potential it experiences, and the less motion the particle undergoes [110], so the amplitude of the noise (fluctuation) is expected to be lower (root-mean-squared-deviation). The stiffness is proportional to the polarizability of the particle, which is higher for longer particles, so less deviation (fluctuation) is expected if the protein is extended by a point mutation.

Another variable that can be extracted from the record of scattered intensity is the power spectral density. This has a corner frequency proportional to the trap stiffness divided by the hydrodynamic drag on the particle [110] and so is expected to show the opposite trend of increasing as the particle lengths (opposite to the RMSD), which gives us yet another independent means by which to carry out the same analysis. Figure 2.1 below shows an example

of the acquired signal from trapping PR65 at an intensity of ~ 11.25 mW/μm^2. The "noisiness" of the signal comes from the motion of PR65 in the optical tweezer. The first step comes from what is known as the "dielectric loading" of the aperture, where the presence of the dielectric causes the transmission through the aperture to increase (jump) while the second step comes from the conformational change of PR65.

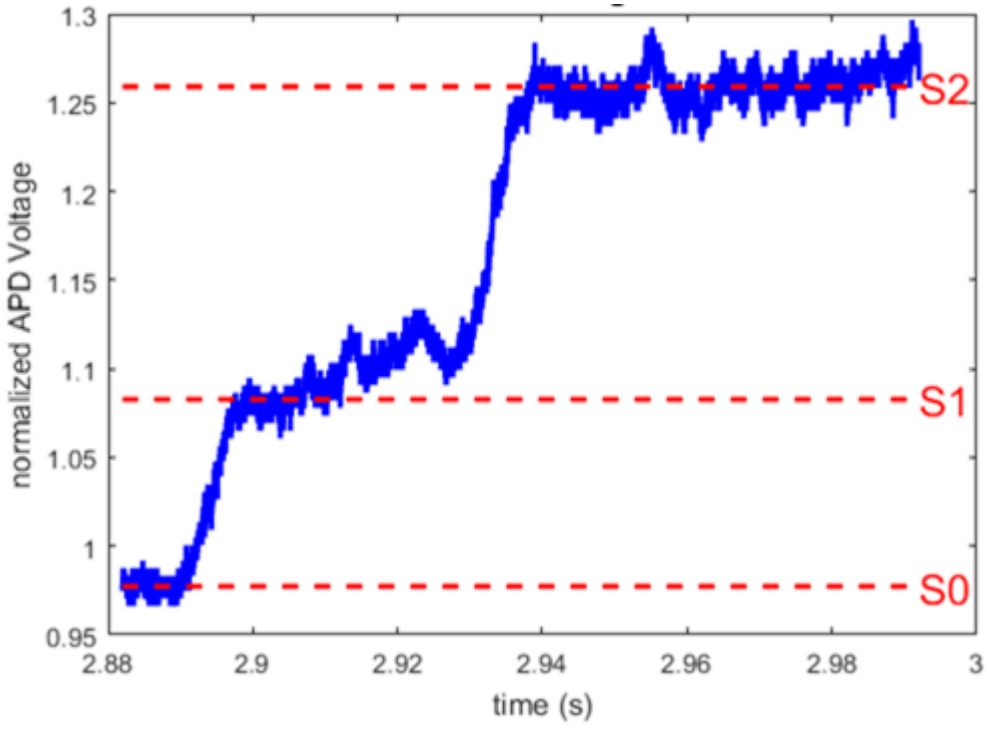

Figure 2.1: Trapping signal of PR65 showing double jump S0 to S1 and then S1 to S2 due to electrostriction-induced conformational change.

Chapter 3

The PP2A Assembly and Techniques for Studying Protein Interactions

3.1 Introduction

In this chapter we describe how the protein phosphatase 2A (PP2A) functions; we also present a brief account of the techniques mentioned in the first chapter for studying protein conformation and the interaction of proteins with other molecules such as the small molecule activators of PP2A (SMAPs). The material in this chapter would be useful for understanding the remainder of the work, especially for the non-expert.

3.2 The Protein Phosphatase 2A (PP2A)

The 3-dimensional arrangement of atoms in a molecule of a protein leading to a specific shape of the protein molecule is known as the structure of the protein or as the protein's conformation [149]. The specific structure or conformation ordinarily adopted by a protein is known as its native fold, and allows it to perform a specific biological function, during which a protein would usually undergo changes in structure known as conformational changes [150].

Broadly, protein structure is classified into four hierarchical orders [151]. The lowest order structure is the primary structure, which simply refers to the amino acids that make up a protein, known as the amino acid residues of the protein [152]. The primary structure is important because it is believed to determine how a protein folds, with every protein sequence folding into a unique shape to enable the protein to perform its specific biological function [153]. At a higher

level of structural organization is the secondary structure, which refers jointly to the structure (technically referred to as a polypeptide) formed by linking two or more amino acid residues together by peptide and, if any, disulfide bonds and the spatial arrangement of the amino acid residues. There are two very common arrangements – the α-helix and the β-sheet. The α-helix is the structure that results when amino acid residues are arranged in a helix around a spine, while the β-sheet is the structure that results when amino acid residues form strands which are linked side by side by side by side by hydrogen bonds. Figure 3.1(a) below shows an α-helix whereas figure 3.1(b) shows a β-sheet.

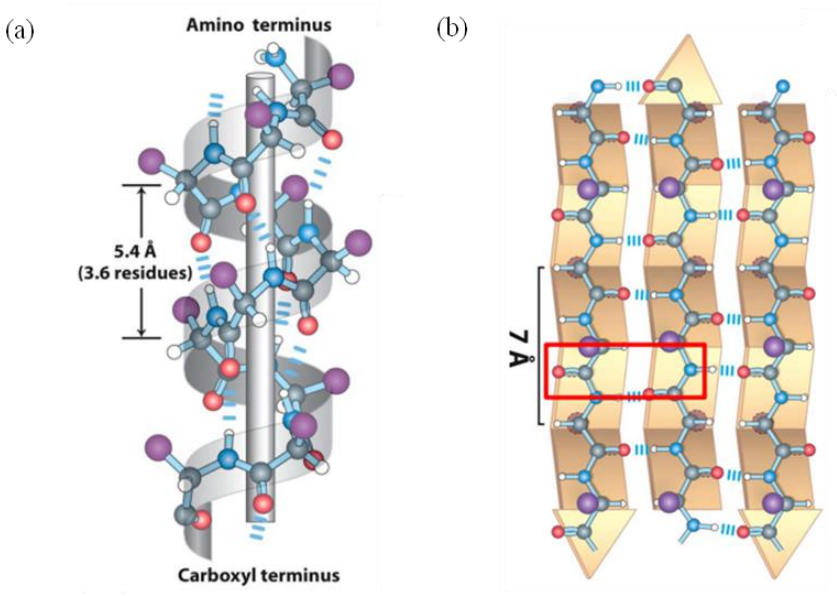

Figure 3.1: An α-helix and (b) a β-sheet. Purple balls represent R groups, grey balls represent Carbon atoms, blue balls represent Nitrogen atoms, red balls represent oxygen atoms and white balls represent hydrogen atoms. Copyright: Freeman & Company, W & H, New York.

At an even higher level of structural organization is the tertiary structure, which refers to a collection of secondary structures linked together by electromagnetic interactions such as van der Waals, hydrogen and ionic bonds involving amino acid side chains called R groups forming a more complex 3-D folded structure. The difference between a secondary structure and a tertiary structure also involves the length scale over which they are defined. Secondary structures are defined over very short length scales typically spanning a few tens of amino acid residues and are as such said to be local structures. Tertiary structures, on the other hand, span several secondary structures and are thus said to be global structures.

At the highest level of structural organization is the quaternary structure, which consists of an assemblage of tertiary structures forming a complete and functional protein assembly in which each tertiary structure is referred to as a monomer or subunit of the protein assembly [154]. The subunits are held together in the quaternary structure by the same forces that bind secondary structures together in the subunits. The protein phosphatase 2A (or PP2A) is a quaternary structure [103], [155], [156]. In fact, the PP2A assembly is not a single protein but a complex assemblage of different proteins, each with a distinct structure and function [157]. Broadly, however, the PP2A assembly is divided into two parts – a core enzyme part and a holoenzyme part [157]. Core enzymes and holoenzymes are similar in the sense that they both convert biological substrates to products but differ in the sense that while a core enzyme achieves this all by itself, a holoenzyme requires the presence of a non-protein chemical compound known as a cofactor to function [158]. The core enzyme part of PP2A consists of a scaffold subunit designated as the A subunit, a catalytic subunit designated as the C subunit and a variable regulatory or B subunit. The B subunit can be one of different tertiary structures identified, respectively, as B, B′ B″, B‴. The core enzyme together with any of these forms the

holoenzyme part. This makes PP2A able to interact with a wide variety of substrates [157].

Figure 3.2 below shows a cartoon of the PP2A assembly.

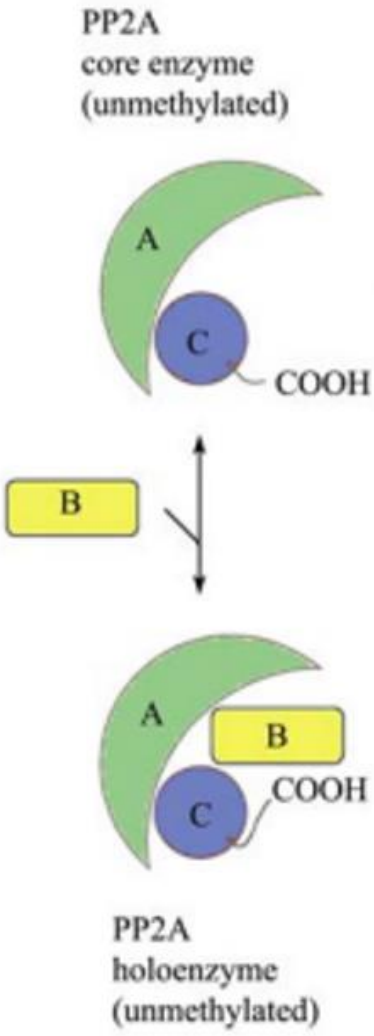

Figure 3.2: Cartoon illustration of the PP2A Assembly showing the A, B and C subunits. Source: Adapted from [153]. Copyright: Freeman & Company, W& H, New York.

As a phosphatase, PP2A plays a vital role in cancer as it reverses the action of kinases which control cell activities such as growth, division, proliferation, and survival [159]. For example, errors can occur during cell division. Normally, appropriate kinases would signal for abnormal cells resulting from errors during cell division to die. But it can so happen that the wrong signal is sent by kinases such that, instead of dying, abnormal cells thrive and proliferate in the absence of phosphatases to reverse the action of the kinases, or where such phosphatases have been deactivated, thereby leading to cancer. PP2A thus has a tumor suppressing activity. PP2A can reverse the action of kinases because while kinases act as molecular switches by phosphorylating their substrates, phosphatases like PP2A achieve their molecular switching action by dephosphorylation of their substrates [160].

The foregoing action by PP2A has been attributed to the A subunit of PP2A [128], [161], either in the Aα or Aβ conformation, with the former being more abundant [157]. The small molecule activators of PP2A also act by binding to the Aα, thereby driving the conformational changes that reactivates PP2A to act against oncogenic kinases to halt the progression of tumors [128]. The Aα subunit of PP2A (also known as PR65, where this abbreviation stands for the 65 kDa putative regulatory subunit of PP2A) has a primary structure consisting of a sequence of 39 amino acid bases. It may be useful to define a few terms for the benefit of the uninitiated prior to describing the secondary structure of PR65. A gene is a molecule that is responsible for transmitting traits such as height and color in plants and animals. An allele is a copy of a specific gene that differs slightly from the original in the way in which it is coded. A diploid organism is one in which genes that determine specific physical traits such as height and color occur in pairs. Haploinsufficiency is a term that refers to the lack of tolerance of a gene to the loss of an allele in a diploid organism [162]. With these terms now defined, the secondary structure of PR65 should

be appreciated without difficulty: it is simply a two-layered, left-handed (that is, wound in an anti-clockwise fashion) α-helix, 15 of which are tandemly repeated to form the horseshoe tertiary structure that is PR65 itself [156], whose importance lies in the fact that it functions as a haploinsufficient tumor suppressor gene by playing a role in regulating phosphatidylinositol 3-kinase (PI3K) signaling [161].

3.3 Survey of Selected Techniques for Studying Protein Conformation and Interactions

A selection of techniques used in studying protein conformation and interactions is now surveyed. The selection is not at all exhaustive because the purpose is not so much to give an exhaustive review the techniques commonly employed for the aforementioned purpose per se than it is to provide a comparison for the performance of optical tweezers, and especially DNH optical tweezers, employed for the same or similar purpose, providing justification for the choice of the latter for the current investigation.

3.3.1 Equilibrium Dialysis

Equilibrium dialysis is one of the techniques for establishing binding between macromolecules such as protein molecules and small molecules (ligands) [128]. Binding is indirectly established in this technique using the equilibrium concentration of ligands on one side of a semipermeable membrane which permits only ligands through it.

To understand how the technique works, imagine having 10 molecules of a protein on one side of a membrane that permits the passage of ligands from the opposite side of the membrane through it, but not protein molecules. Suppose there are 20 ligands on the opposite side of the membrane. The difference in the concentration of ligands on the two sides of the membrane will

drive ligands from the side where they are in higher concentration to the side where their concentration is less until equilibrium is established by the concentration of ligands on both sides of the membrane being equal. Thus, in the absence of binding, equilibrium will be established across the membrane when there are 10 ligands on the side of the membrane opposite the side containing the protein molecules (and 10 ligands on the side of the membrane containing the proteins). If there is binding, however, the 10 ligands which cross to the side of the membrane containing proteins will all be removed from solution by binding to the 10 molecules of protein on that side of the membrane, which would leave an excess of 10 ligands on the opposite of the membrane and, therefore, a concentration gradient that continues to drive ligands across the membrane to the other side of it. Since there are now no more free proteins on the side of the membrane opposite the side where the ligands are contained, equilibrium is reached when there are 5 ligands opposite the side of the membrane initially containing free proteins (and 5 ligands on that side as well). That is, binding is established in equilibrium dialysis whenever the final concentration of ligands (5 in this hypothetical example) is equal to the initial concentration of ligands (20 in this hypothetical example) less half the difference between the initial concentrations of ligands and macromolecules ($5 = (20 - 10)/2$, in this hypothetical example). Figure 3.3 below is a visual demonstration of this process taken from [163].

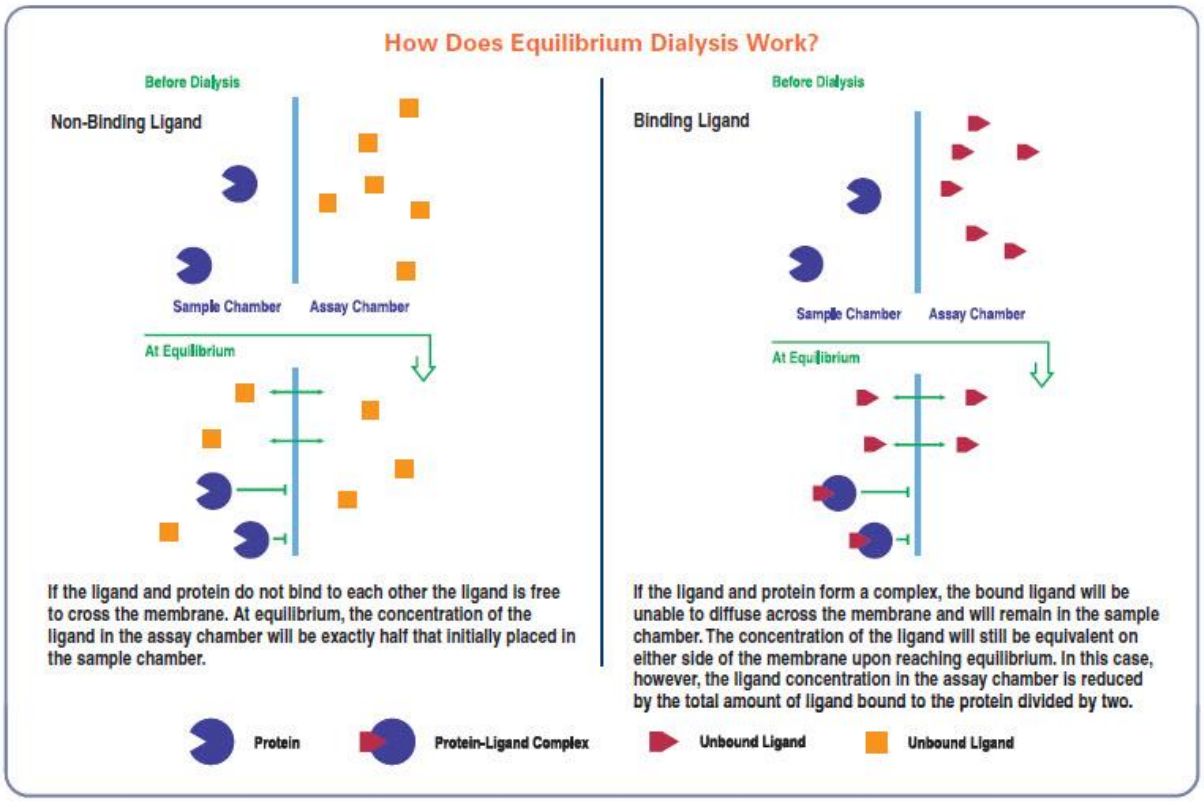

Figure 3.3: Illustration of Equilibrium Dialysis. Copyright: Havard Apparatus.

In Chapter 2 it was described how this could be done using DNH optical tweezers. Compared to the use of the DNH optical tweezers, equilibrium dialysis is both slow and more expensive. Slow because one must wait for equilibrium to be reached, which can take a while for a process driven by diffusion across a membrane; and more expensive because a larger amount of both protein and ligand is required for equilibrium dialysis than for a DNH optical tweezers as was discussed in Chapter 2.

3.4 Photoaffinity Labeling

Photoaffinity labelling (PAL) is another technique used for studying protein-ligand interaction or binding [128]. The technique gets its name from the use of molecular tags or probes which get activated by illumination with light of a specific wavelength such as ultraviolet light or infrared radiation [164]. A photoaffinity label has three parts to it [165] – an affinity or specificity unit, which refers to the small molecule or ligand which binding to a given protein is of interest; a photoreactive molecule such as benzophenone and a molecular identification tag such as biotin. The affinity unit is designed to bind with a specific protein, and when introduced into an environment containing the target protein and given time, the affinity unit binds covalently and reversibly with the target protein. The mixture is then irradiated with light of the appropriate wavelength so that the photoreactive molecule forms a highly reactive intermediate that quickly binds irreversibly to the protein before the affinity unit can dissociate from the protein. This fixes the entire photolabeling unit permanently to the protein. The identification tag enables the target protein to be isolated and studied. There are many routes by which this isolation can be done. For example, streptavidin could be used to bind the biotin of the photoaffinity label, or an antibody (a type of blood protein produced in response to and counteracting a specific body or substance which the body of an organism finds to be foreign to itself) could be used to bind to the protein's epitope – also known as an antigenic determinant, is the part of an antigen molecule (a molecule foreign to the body of an organism, and, therefore, causing an immune response from the body of the organism), to which an antibody attaches itself – thereby isolating the target protein [165]. This method of isolating a protein-ligand complex is known as affinity chromatography [166]. A resin is coated with streptavidin or a particular antibody. The resin is contained in a column which is pre-equilibrated in an appropriate buffer prior to introducing the sample containing the

protein. The protein of interest is tethered to the resin by the streptavidin or antibody binding to the biotin or epitope of the photoaffinity label bound to the protein of interest while all other proteins freely flow out of the column until they have all been removed.

The protein of interest is then extracted by changing the pH, which disrupts the bonding between streptavidin or antibody and biotin or epitope allowing the protein-ligand complex to flow out. This process also enriches the labelled proteins [165]. The captured protein-ligand complex is then analyzed using Sodium Dodecyl Sulfate PolyAcrylamide Gel Electrophoresis (SDS-PAGE) and Western blotting, and the protein of interest excised from the gel.

SDS-PAGE is a chromatographic technique for separating and analyzing proteins based on their molecular weights. Disulfide bonds are first reduced from the protein by treating the protein with β-mercaptoethanol, for instance. This aids the unfolding of the protein. SDS – an ionic detergent – is then further used to disrupt non-covalent bonds in the proteins causing them to unfold. SDS further binds to the unfolded proteins, covering them in negative charge. The result is that the proteins all acquire a near identical charge to mass ratio. Because the proteins so treated become identically charged, separation is based solely on the molecular weight of the proteins.

An accelerating electric field is subsequently introduced between two electrodes sandwiching a column containing the proteins by connecting the electrodes up to a source of steady electromotive force (emf). A constant electric force is thus exerted on the charged proteins in the column, such that the proteins acquire a velocity inversely proportional to their molecular weights, such that, at any given instant, lighter proteins are drifting faster than heavier ones, with the result that after some time the proteins become separated into bands at varying distances from one another. The bands are made visible by staining with a dye such as Coomassie blue,

with a leftmost band of proteins of known molecular weights, known as marker proteins, used as a reference for determining the molecular weights of the analyzed proteins. Figure 3.4 below illustrates the process of attaching molecular tags to proteins.

Western blotting is a similar chromatographic technique used to identify unknown proteins but will not be described here because interest is being limited to surveying techniques employed in the investigation of the interactions of known proteins. Compared to the use of nano-optical tweezers such as DNH optical tweezers, photoaffinity labeling is both more complex, time-consuming, and expensive. It also has the potential of altering the target protein, thereby interfering with its interaction, if not done properly and with the utmost care and design. It also cannot yield any information on how interaction affects the target protein, whereas this can be deduced with an optical tweezers system such as a DNH optical tweezers as was described in Chapter 2. With photoaffinity labeling, there is also the problem of optical bleaching, quenching by water molecules and non-specific binding. However, it has the advantage that it can reveal the specific site of binding, which cannot be done with optical tweezers.

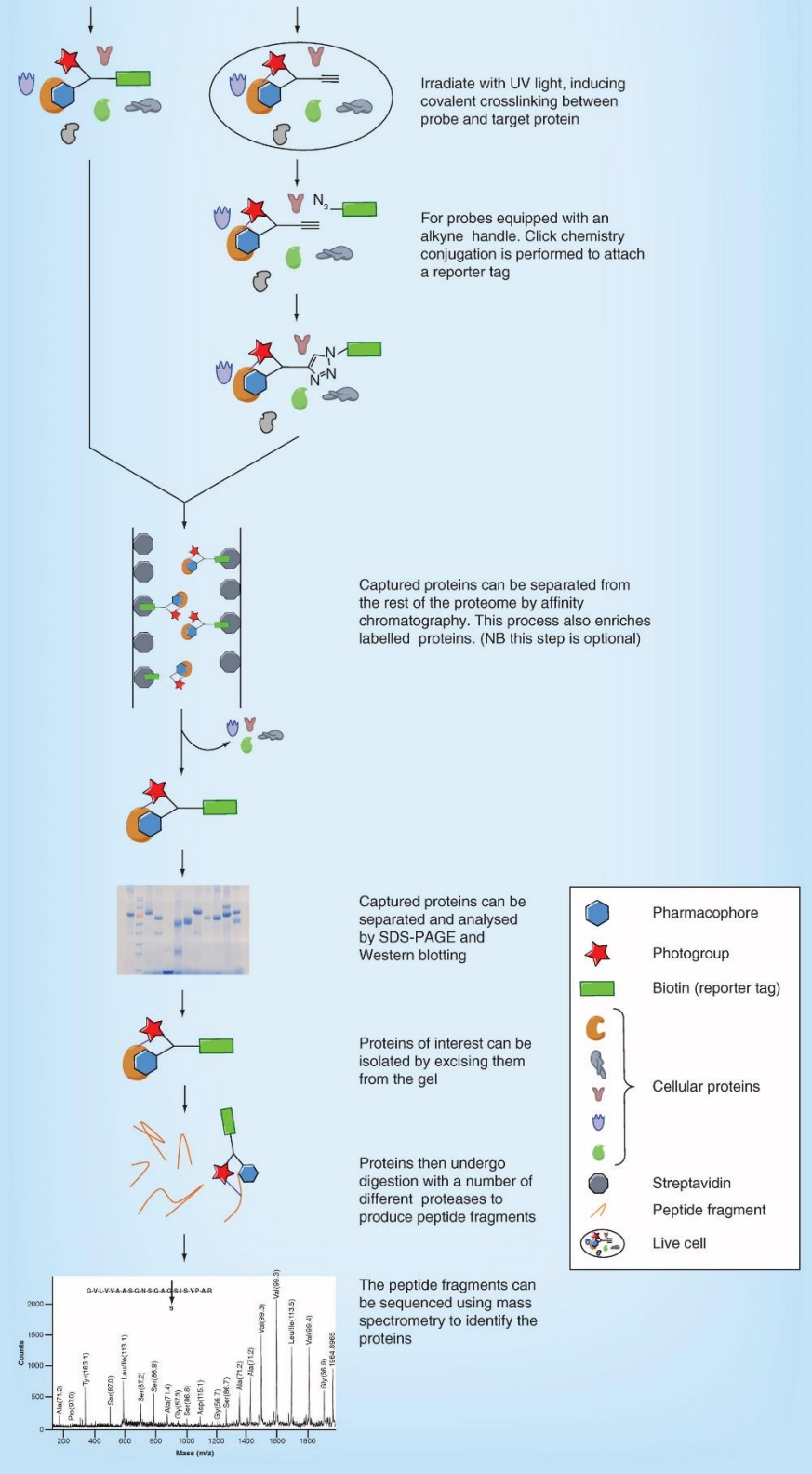

Figure 3.4: Schematic of PAL workflow. Copyright: Future Science Ltd.

3.5 Radio Labeling

Radio labeling provides another option for the identification tag used with photoaffinity labeling in investigating protein-ligand interactions [165]. The radio label – often tritium or iodine-125 – is incorporated into the ligand, and detecting radiation in captured protein-ligand complex after separation would be evidence of successful binding. Issues with this mainly concern the safety of handling and the care required to prepare samples and dealing with the very short lifetimes of the radio isotopes which can make measurement very difficult – all issues which are absent with the technique of optical tweezers, and especially nano-optical tweezers employing plasmonic effects such as the DNH optical tweezer.

3.6 Fluorescence Correlation Spectroscopy

This relies on the difference in the hydrodynamic characteristics of a protein in different conformations [167]. It essentially provides information on changes in protein conformation via measurement of the hydrodynamic radius. Molecules to be examined using fluorescence correlation spectroscopy are tagged with a fluorophore and illuminated in solution using focused light. The Brownian motion of the molecules induces a fluctuation in the measured fluorescence intensity of the molecules, which is analyzed using temporal correlation to extract kinetic parameters such as hydrodynamic radius associated with the Brownian motion underlying the fluctuation in the measured fluorescence intensity. The disadvantage of this technique in comparison with the use of optical tweezers such as the DNH optical tweezer is its use of fluorescent tags which can modify the protein and confound results. The use of fluorescent tags also makes the experimental design and procedure more complex and expensive, which can be avoided using optical tweezers techniques such as afforded by the DNH optical tweezer.

3.7 Single Molecule Fluorescence Energy Transfer

This technique utilizes the distance dependence of Förster resonance to study conformational changes in proteins by attaching donor and acceptor chromophores at a single location on a protein and measuring the efficiency of the Förster resonance energy transfer, is inversely proportional to the sixth power of the distance between donor and acceptor, between the chromophores, which provides direct information about the separation between the chromophores as the protein to which they are attached undergoes conformation changes [168]. As with fluorescence correlation spectroscopy, single molecule fluorescence energy transfer requires fluorescent tags, which is a disadvantage compared to optical tweezer techniques such as DNH optical tweezers.

3.8 Single Molecule Force Spectroscopy

In this technique, tension or compression forces applied to a single protein molecule through tethers at two adjacent locations on a protein provide insight into the mechanical properties of a protein, such that the response of a protein to being altered or, equivalently, feedback from a mechanically altered protein can be used to monitor and to detect conformational changes undergone by a protein [169]. Here, the disadvantage relative to the DNH optical tweezer is the requirement for tethers which means that the probe force is not directly applied to the protein under investigation. Additionally, the dynamics of the tethers can obscure that of the protein under investigation.

3.9 Nanopore Electro-Osmotic Trap (NEOtrap)

In this technique, a process – known as electro-osmosis – involving hydrodynamic flow of ions under a spatially uniform electric field through a porous origami-DNA sponge, or similar

structure, adsorbed to a solid state membrane across a nanopore is used to drive a single protein molecule towards the origami-DNA molecule to which the protein then gets attached, producing a signature drop in ionic current that is used to interrogate physical properties of a protein as well as any conformational changes which may be undergone by a protein [121]. This technique, although not requiring the use of tethers or labels, has only been demonstrated for proteins of about 50 nm [121] in diameter whereas the DNH optical tweezer has been used to trap and manipulate proteins down to about 12 nm across [170].

3.10 DNH Optical Tweezers

The DNH optical tweezer is a type of a nanoplasmonic tweezer that incorporates a structure consisting of a metal film on glass, with an aperture composed of two overlapping circular apertures made using one of several techniques such as focused ion beam milling (FIB), colloidal lithography, electron beam lithography (EBL), reactive ion etching, template stripping, *et cetera*, such that the depth of each aperture is equal to the thickness of the metal film. Laser light is focused through the aperture in a diffraction limited spot, creating an intensity gradient that is the source of the trapping force experienced by a particle that approaches within the range of this force. The particle scatters light, which intensity is measured using an avalanche photodiode (APD), and once trapped, the Brownian motion of the particle induces a fluctuation in the measured scattered intensity, analyzed using either the temporal autocorrelation or power spectral density method [61] or in terms of the RMSD of the fluctuation of the measured scattered intensity [139]. The technique boasts a number of advantages such as not requiring labels and tethers [136], being relatively inexpensive and easy to fabricate [96], having a high sensitivity [6], and requiring small volumes of sample solution that need not be highly purified [116].

Chapter 4

Colloidal Lithography Fabrication of Plasmonic Double Nanohole Apertures

4.1 Introduction

In this chapter we discuss the first of several steps taken to investigate the research questions raised in the penultimate paragraph of the first Chapter. Specifically, we describe the fabrication of plasmonic DNH apertures by the method of colloidal lithography.

4.2 Colloidal Lithography

Lithography is derived from two Greek root words, namely, “lithos” meaning stone [171] and “graphein” meaning to write [172]. It refers to a range of techniques for writing using templates [173]. Lithography was invented in the late 18^{th} century by Johann Alois Senefelder [174]. Lithography has been used for writing patterns on surfaces in nanofabrication since the 20^{th} century [175]. For example, Fischer and Zingsheim used lithography to imprint patterns with a 100 nm resolution onto a photoresist in 1981 [175]. This seminal work could only write such patterns over a limited area of a surface of at most 25 μm^2, but this limitation was soon eliminated via the method devised by Deckman and Dunsmuir in 1982 [176]. This technique has variously been dubbed natural lithography [176] and nanosphere lithography [177], [178]. We adopt the term colloidal lithography [96] to emphasize the fact that the technique relies on the use of colloidal nanospheres that are deposited on a surface and used as either deposition or etching masks, but especially the latter in our case.

Colloidal lithography has been used for fabricating nanoapertures for over 3 decades, beginning with Fischer who in 1985 and 1986, respectively, used the technique to fabricate single nanohole apertures for studies in microscopy and spectroscopy, respectively [179], [180]. The optical properties of nanoapertures made by colloidal lithography have been studied by numerous researchers, for example, [181], [182], [183] and one can easily observe that they are identical with those made by other techniques such as focused ion beam milling (FIB) [39], but offers more flexibility with regard to parallel processing, ease of implementation, and low cost [96]. We can even report finding less variation in apertures made using colloidal lithography as opposed to focused ion beam milling, for example. The use of colloidal lithography for making nanoapertures has not been limited to single nanoholes (SNH) as double nanoholes apertures (DNH) have also been made using the technique [184]. The cusp sizes of this early double nanohole aperture tweezers, while adequate for the purposes they were made, can be made smaller for a more robust trapping of smaller particles like proteins if, prior to metal deposition, the colloidal masks used for making the double nanohole apertures were etched in a high-power plasma as described in [96].

The caveat against using the colloidal lithography technique for making double nano-hole apertures is that it is random and, as such, gives the fabricator no control over what type of nanohole aggregations are predominantly produced. This can be overcome if a technique can be found for controlling the placement of the polystyrene nanospheres on a surface in such a way as to form a preferred pattern consisting solely of singles, doubles, triples, etc. as desired. Some promising routes that have been explored for implementing this include dielectrophoresis [185] and nanorobotic manipulation [186]. The results are far from perfect, however, so more work needs to be done in this regard.

In the work being reported, we used polystyrene beads as masks for making DNH apertures. First, microscope slides (12-550-A3, Fisherbrand) are cleaned for 15 minutes in a plasma machine at high power and then sonicated for 8 minutes in an ethanol bath. 38 mL of ethanol is added to 30 µL of 10 % w/v solution of 500 nm polystyrene beads and stirred thoroughly. Each of the microscope slides from the previous step is uniformly drop-coated with the resultant solution from the last step. The coating is allowed to dry out overnight by evaporation in a dust-free environment, so that the nanospheres adhere to the microscope slides. This is followed by separately exposing each slide from the last step to a beam of plasma for a time that varies from 170 seconds to 177 seconds to etch the polystyrene beads down to create the narrow cusps between pairs of touching polystyrene beads, with each slide being exposed for a minute longer than the one before it. It was found that slides exposed for 173 seconds and 174 seconds were best for trapping PR65. The range of etch times was initially estimated based on the target cusp size, which must be wide enough to fit the particle to be trapped and yet narrow enough to give considerable field enhancement for stable and efficient trapping. For how to satisfy both conditions, reference was made to [96], which is a previous study establishing the relationship between the etch time and the cusp size.

Following the last step, a 7 nm thick adhesion layer of titanium was deposited on the microscope slides with plasma-etched polystyrene beads on them, followed by the deposition of a 70 nm thick layer of gold. Once this process of deposition was complete, the slide was sonicated for 6 minutes in an ethanol bath to remove the polystyrene beads, producing nanoholes of different aggregations on the surface – singles, doubles, triples, et cetera as shown in Figure 4.1 below.

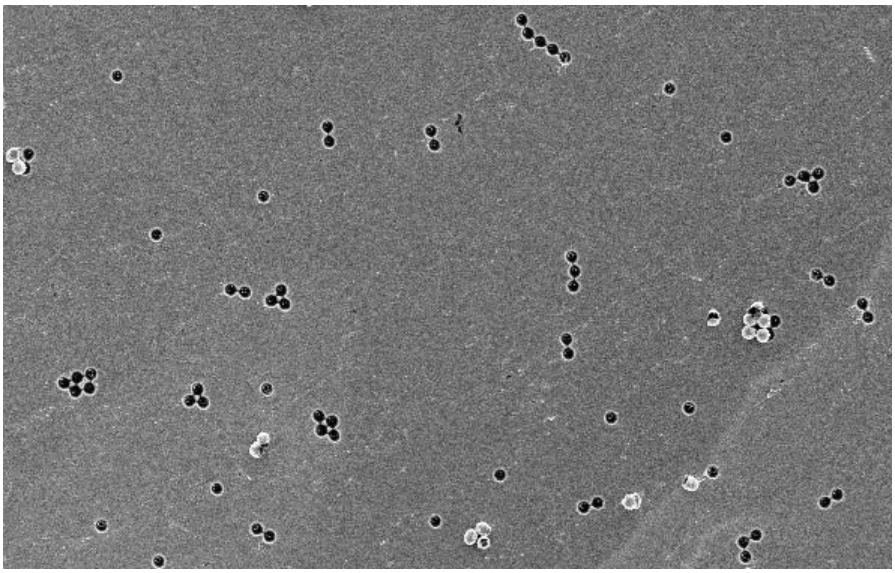

Figure 4.1: Array of nanoapertures on a glass substrate made by colloidal lithography.

A zoom in of a double nanohole aperture from Figure 4.1 above is shown in Figure 4.2 below.

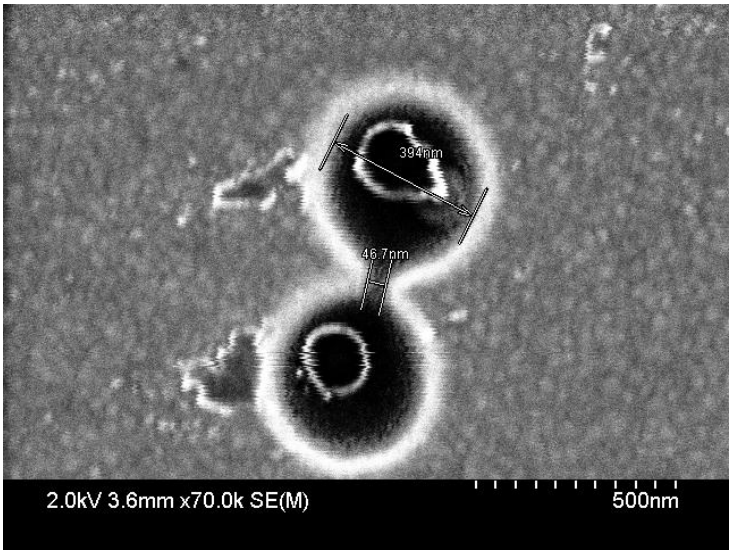

Figure 4.2: A double nanohole isolated from Fig. 4.1

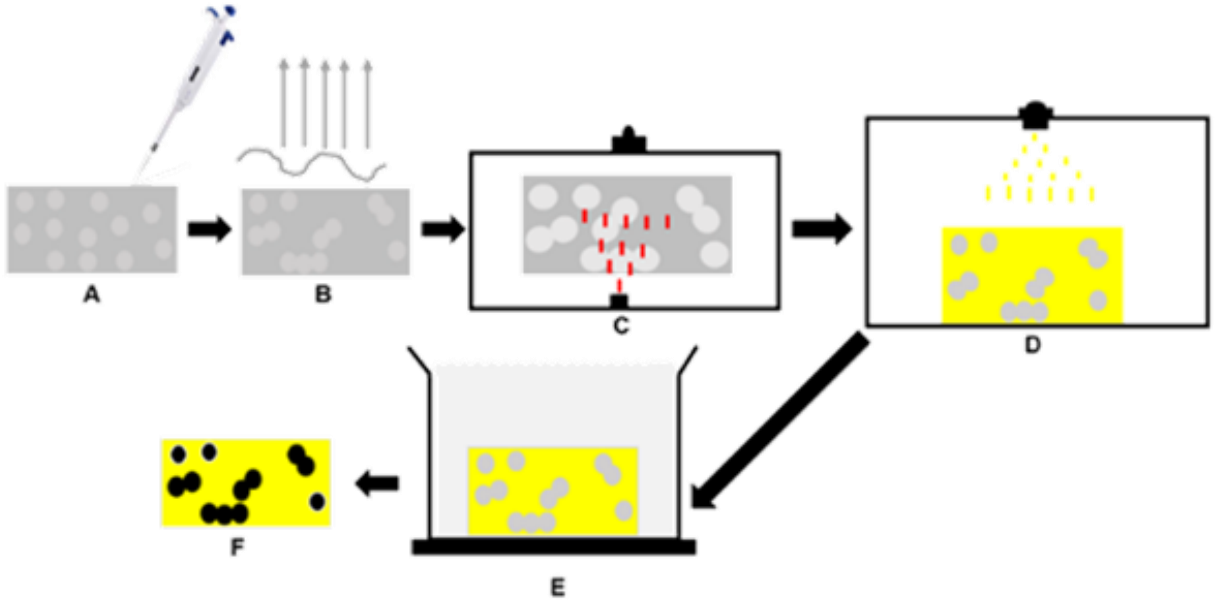

Figure 4.3: Process flow for making DNHs by colloidal lithography. A. Drop-coating glass with colloidal solution. B. Evaporating water from drop-coated glass and coalescence of polystyrene beads. C. Plasma etching. D. Titanium/Gold deposition. E. Sonication. F. Finished sample of nanoapertures in gold-on-glass showing single nanoholes (SNH), double nanoholes (DNH) and triple nanoholes (TNH). Even more complex composites like quadruples and higher occur, but with increasing rarity, in real samples [96].

Figure 4.3 above is the flow process summarizing the fabrication of the DNH aperture by colloidal lithography. Figure 4.4 below shows an example of the trapping signal for PR65 trapped using a DNH aperture made by colloidal lithography, where the time trace has been normalized with respect to the mean of the pre-trap signal, the pre-trap portion of the signal being the segment on the left of the vertical step up to about 2.7 s on the time axis.

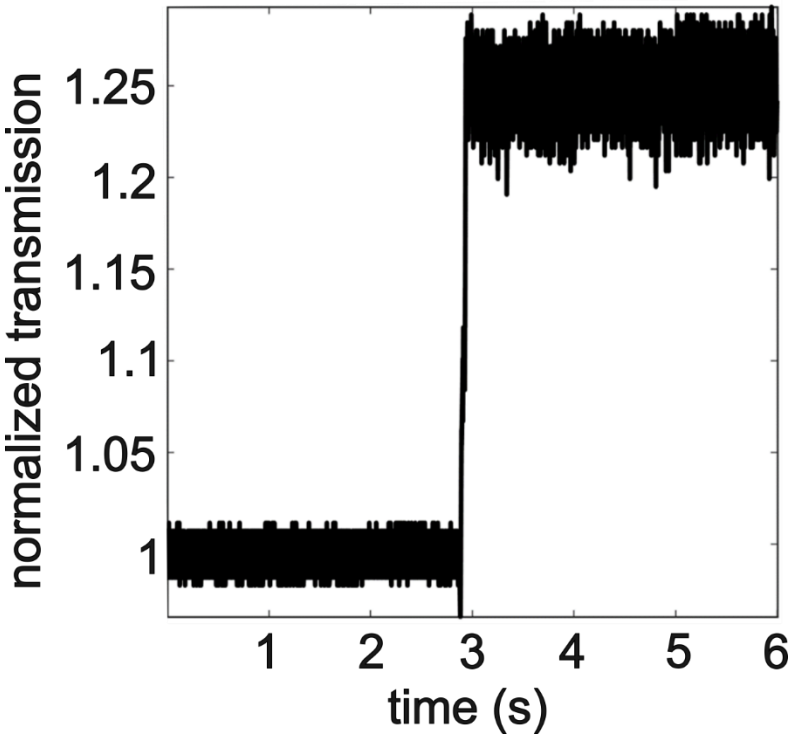

Figure 4.4: Signal for PR65 trapped with a DNH made by colloidal lithography.

Focused ion beam milling (FIB) [170] has been mentioned in passing as a technique for producing DNH apertures. It enjoys an advantage of allowing a researcher control over what type of apertures to produce and where to position the apertures on a surface. It is, however, a more expensive technique than colloidal lithography in terms of instrument requirement. Colloidal lithography also requires less skill in implementation, which may account for the less variability that we seem to have observed between the apertures produced by colloidal lithography and those that were previously made using FIB. Difficulties with using FIB, for example, include aligning the beam, dealing with surface charge issues, being precise with cutting angles, etc.

Apart from FIB, there is also the template-stripping technique of producing DNH apertures [94]. In this technique, DNH apertures are made on a master or template which are then

transferred to other surfaces on which DNH apertures are desired to be reproduced. This technique has the advantage of being cost effective, with the major cost being in the production of the master which can be reused again and again and allowing for parallel production and a high throughput. The disadvantage is that the master is only as good as the technique used in making it. Accordingly, it is susceptible to high systematic errors where the technique used to produce the master has accuracy, precision or both issues.

As can be seen, the master for a template-stripping process can be made either by FIB or colloidal lithography. Apart from the precision issues associated with the FIB technique, template-stripping using FIB to make the master would have been the best technique. However, because of the precision colloidal lithography, template stripping can be done away altogether with no increase in cost.

In conclusion, while colloidal lithography is limited by giving a researcher little control over what type of aperture to preferentially produce and where and how to position apertures on a surface, therefore calling for more research and innovation on the technique, it clearly provides an economically viable means of making DNH apertures reproducibly, which justifies our choice of the technique for making the DNH apertures used for this work.

Chapter 5

Self-Induced Back-Action for Aperture Trapping: Bethe-Rayleigh Theory

5.1 Introduction

In this chapter we look at the Self-Induced Back-Action (SIBA) effect for off-resonant apertures within the framework of the Bethe-Rayleigh theory to elucidate the advantages of optical trapping using shaped apertures vis-à-vis conventional optical traps. It is shown that while surface plasmons do exist in real systems, they are not necessary or required for the occurrence of the SIBA effect. This is shown analytically, followed by numerical simulations which show that the analytical model developed captures the physics of the system. While the theory of this chapter is developed for a single circular aperture in a perfect electric conductor (PEC), it is argued that this can be extended to other shaped apertures and to multiple such apertures.

5.2 SIBA in Optical Trapping Theory and Practice

SIBA arises from the interaction of a particle with a local electromagnetic field in such a way that the particle modifies the field, and therefore the force that the particle feels from the field, thereby contributing to its own trapping [65]. Aperture trapping was first investigated numerically by [81]. This was followed by an experimental demonstration of particle trapping near an aperture [83]. Since that demonstration of particle trapping near an aperture, apertures have been used in a variety of other optical trapping experiments with the same success. Examples include the optical trapping of dielectric spheres of varying sizes [65], [170], [187],

proteins [137], [127], [115], [188], [139], quantum dots [189], [190], vesicles [191] and several other particles. Theories such as [192] explaining SIBA have tended to be based on shifts in cavity resonances. While such theories sufficiently describe SIBA in resonant systems such as photonic crystal cavities [193], [194], [195] and apertures [196], they are not as adequate for describing SIBA in non-resonant systems such as off-resonant subwavelength apertures, necessitating other theories that bridge this gap. A simple theory explaining SIBA in non-resonant subwavelength apertures in terms of the Bethe-Rayleigh aperture-particle theory is here proposed. Finite-Difference-Time-Domain (FDTD) simulation is used to show that this simple theory captures the physics of SIBA in non-resonant subwavelength apertures. The theory under discussion is developed for a single subwavelength aperture in a PEC, but it is argued that this can be extended to other systems such as other shaped apertures and multiple apertures.

5.3 Bethe-Rayleigh SIBA theory

The theoretical quantification of SIBA when an aperture satisfying Bethe's theory interacts with a particle in the Rayleigh regime is now developed. For the purposes of this theory, an aperture satisfying Bethe's theory will be called a Bethe aperture while a particle which interacts with an electromagnetic field according to Rayleigh's theorem will be referred to as a Rayleigh particle. It will be shown that the SIBA effect can be modelled as an interaction between a Bethe aperture and a Rayleigh particle, with the Bethe aperture modelled by a magnetic dipole and the Rayleigh particle by an electric dipole. Figure 5.1 below shows the schematic of the geometry of the problem, where the following parameters are defined: R is the radius of the Bethe aperture, a is the radius of the Rayleigh particle, r is the center-to-center distance from the Bethe aperture to the Rayleigh particle, z is the direction of propagation of the beam of light exciting the Bethe

aperture and *x* is the direction of polarization of the exciting beam of light, modelled as a plane wave.

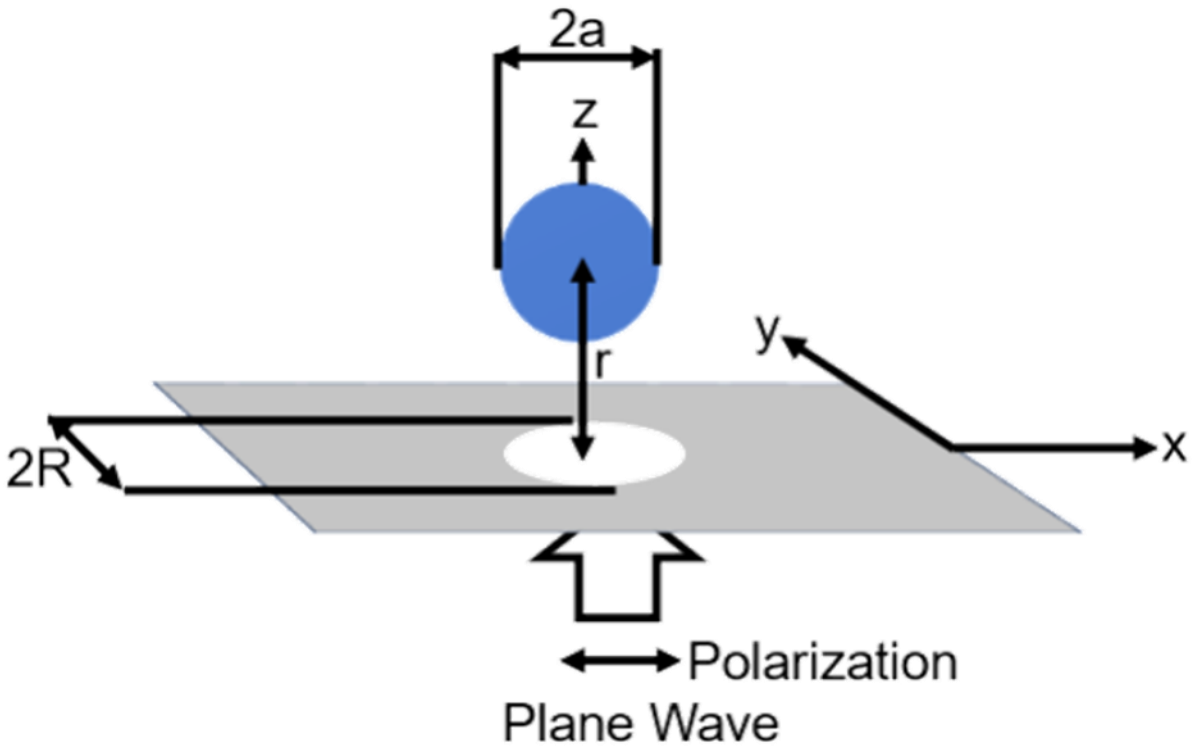

Figure 5.1: Geometry of an aperture in a metal film interacting with sphere with light incident from the opposite side. Copyright: Optica Publishing Group.

By Bethe's theory [197], the electric field produced by a subwavelength aperture in a perfect electric conductor can be modelled in terms of the electric field of an effective magnetic dipole with magnetic polarizability,

$$\gamma = \frac{8R^3}{3} \tag{5.1}$$

assuming a plane wave normally incident from below the conducting screen containing the aperture. The effective magnetic dipole at the aperture produces an electric field, $\vec{E}_m$, given by

$$\vec{E}_m = -\frac{Z_0}{4\pi} k^2 (\vec{n} \times \vec{m}) \frac{exp(ikr)}{r} \left(1 - \frac{1}{ikr}\right) \quad 5.2$$

where,

$$\vec{m} = \gamma \vec{H}_0 = \frac{8R^3}{3} \vec{H}_0 \quad 5.3$$

is the effective magnetic dipole moment of the aperture, with $\vec{H}_0$ being the magnetic field imposed on the aperture, Z_0 is the impedance of free space k is the propagation constant, $\vec{n}$ is the unit vector pointing in the direction from the center of the aperture to the center of the spherical dielectric and r is the distance from the center of the aperture to the center of the spherical dielectric. A harmonic time dependence is implicit.

The electric field of 2.1 polarizes the dielectric sphere, producing an electric polarization

$$\vec{p} = \alpha \vec{E}_m \quad 5.4$$

where $\vec{p}$ is the electric dipole moment of the dielectric sphere given by,

$$\alpha = 4\pi\epsilon_0 \frac{\epsilon_r - \epsilon_b}{\epsilon_r + 2\epsilon_b} a^3 \quad 5.5$$

with ϵ_r being the relative permittivity of the dielectric sphere embedded in a medium of relative permittivity ϵ_b, and ϵ_0 the permittivity of free space. The polarized dielectric creates a magnetic field, $\vec{H}_p$, given by

$$\vec{H}_p = \frac{ck^2}{4\pi} (-\vec{n} \times \vec{p}) \frac{exp(ikr)}{r} \left(1 - \frac{1}{ikr}\right) \quad 5.6$$

back at the aperture. Here, c is the vacuum speed of light. The magnetic field, $\vec{H}_p$, from the polarized dielectric modifies the magnetic field at the aperture resulting to an effective magnetic field, $\vec{H}_a$, at the aperture given by,

$$\vec{H}_a = \vec{H}_0 + \vec{H}_p \tag{5.7}$$

Thus, the magnetic dipole moment is changed from its value in (5.3) to

$$\vec{m}_{eff} = \gamma \vec{H}_a = \frac{8R^3}{3}\vec{H}_a \tag{5.8}$$

and through this modifies the electric field created by the aperture from what it should have been in the absence of the dielectric sphere, or if the sphere did not interact with the aperture. Using (5.8) in (5.2), we get

$$\vec{E}_m = -\frac{2R^3 Z_0}{3\pi} k^2 \left(\vec{n} \times \vec{H}_a\right) \frac{exp(ikr)}{r}\left(1 - \frac{1}{ikr}\right) \tag{5.9}$$

Using (5.4) in (5.6), we obtain

$$\vec{H}_p = \frac{\alpha c k^2}{4\pi}\left(-\vec{n} \times \vec{E}_m\right) \frac{exp(ikr)}{r}\left(1 - \frac{1}{ikr}\right) \tag{5.10}$$

Inserting (5.9) into (5.10), we get

$$\vec{H}_p = -\frac{\alpha R^3 Z_0 c k^4}{6\pi^2}\left(\frac{exp(ikr)}{r}\left(1 - \frac{1}{ikr}\right)\right)^2 \left(\vec{n} \times \left(\vec{n} \times \vec{m}_{eff}\right)\right) \tag{5.11}$$

If we assume for simplicity that $\vec{n}$ is in the z-direction and $\vec{m}$ is in the x-direction, then (5.11) simplifies to,

$$\vec{H}_p = -\frac{\alpha R^3 Z_0 c k^4}{3\pi^2}\left(\frac{exp(ikr)}{r}\left(1-\frac{1}{ikr}\right)\right)^2 \vec{m}_{eff} \tag{5.12}$$

where the final result has also been multiplied by 2 to account for the image dipole, since the ground plate of the conducting screen implies that the magnetic field at the aperture is doubled by the image dipole of the Rayleigh particle. Making $\vec{H}_p$ the subject of the formula in (5.7), then inserting the resulting expression along with (5.8) into (5.12) and solving for $\vec{H}_a$, we obtain

$$\vec{H}_a = \frac{\vec{H}_0}{1+\frac{\alpha R^3 Z_0 c k^4}{3\pi^2}\left(\frac{exp(ikr)}{r}\left(1-\frac{1}{ikr}\right)\right)^2} \tag{5.13}$$

(5.13) describes the back-action through the term in the denominator. By using (5.13) in (5.8), we obtain

$$\vec{m}_{eff} = \frac{\frac{8R^3}{3}}{1+\frac{\alpha R^3 Z_0 c k^4}{3\pi^2}\left(\frac{exp(ikr)}{r}\left(1-\frac{1}{ikr}\right)\right)^2}\vec{H}_0 \tag{5.14}$$

The transmitted intensity I through an aperture into the half-space, in terms of the effective magnetic dipole moment of the aperture, is given by

$$I = \frac{Z_0 k^2}{24\pi}\left|\vec{m}_{eff}\right|^2 \tag{5.15}$$

In the absence of back-action we use $\vec{m}_{eff} = \vec{m} = \frac{8R^3}{3}\vec{H}_0$ in (5.15) to obtain,

$$I = \frac{Z_0 k^2}{24\pi}\left(\frac{8R^3}{3}\right)^2\left|\vec{H}_0\right|^2 \tag{5.16}$$

By using (5.14) in (5.15), simplifying and dividing the resulting expression by (5.16), we obtain an expression for the normalized transmission,T, through the aperture:

$$T = \frac{1}{\left|1 + \frac{\alpha R^3 Z_0 c k^4}{3\pi^2}\left(\frac{exp(ikr)}{r}\left(1 - \frac{1}{ikr}\right)\right)^2\right|^2} \quad 5.17$$

A plot of T as a function of r, calculated from the Bethe-Rayleigh theory for $a = R = 50$ nm, $\lambda = 500$ nm, $\epsilon_r = 2.343$ and $\epsilon_b = 1$ is shown as a solid dark curve in Figure 5.2 below.

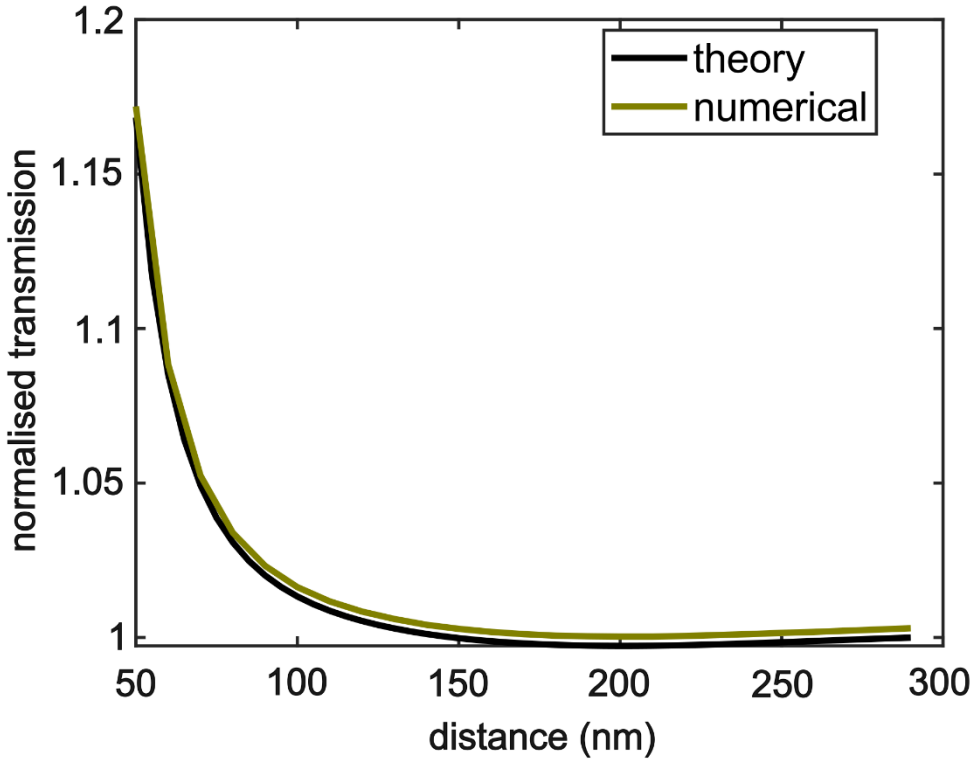

Figure 5.2: Transmission through aperture calculated with Bethe-Rayleigh theory, normalized to transmission without SIBA. Theoretical result and FDTD simulation shown. Copyright: Optica Publishing Group.

The trapping potential is given by,

$$U = -\frac{\alpha}{2}\left|\vec{E}_m\right|^2 \tag{5.18}$$

where all terms are as has been defined and $\vec{E}_m$ is given by (5.2) in the absence of SIBA or, in the presence of SIBA, by (5.9). The calculated difference between the trapping potentials with and without SIBA is shown as a solid dark curve in Figure 5.3 below, for an incident intensity of ~ 11.25 mW/μm^2. The theory is plotted only to 50 nm, so that the aperture and the particle are not overlapping, and the results are physically meaningful.

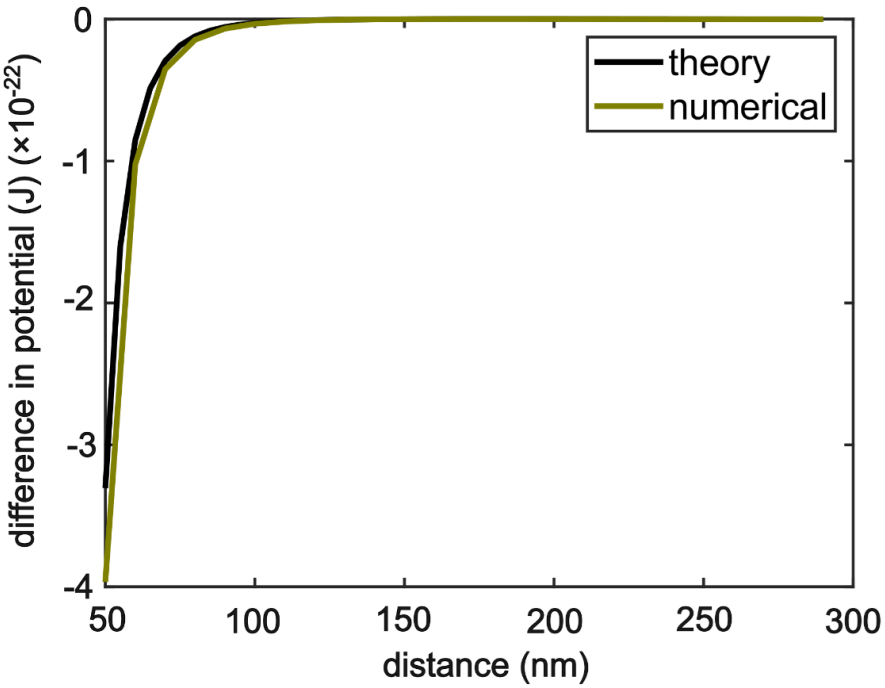

Figure 5.3: Difference in trapping potential of aperture with and without SIBA calculated with Bethe-Rayleigh theory (black), and for the FDTD simulations with and without SIBA (green). Copyright: Optica Publishing Group.

5.4 Numerical Simulations

FDTD simulations were performed using Ansys Lumerical FDTD to show that the dipole model, presented in the preceding section, captures the basic physics of the system. The structure of this FDTD simulation was a 1 nm thick perfect electric conductor (PEC) with a circular aperture of 50 nm radius through its center. The PEC had an area of 1 μm^2 in the $x - y$ plane. Because of the symmetry of the structure, a symmetric boundary condition was imposed at the minimum of the x-axis while anti-symmetric boundary condition was similarly imposed at the minimum of the y-axis. Perfectly Matched Layer (PML) boundary condition was used everywhere else. The simulation domain was made to go through the PEC to simulate an infinitely wide PEC plane. The simulation domain was 900 nm × 900 nm × 1000 nm. A total field scattered field (TFSF) source was used with 201 wavelengths in the range from 500 nm to 1500 nm. The source was y-polarized, with an amplitude of 2.911 × 10^6 V/m and propagated in the forward z-direction. The TFSF source was 640 nm × 640 nm × 682 nm. A dielectric sphere of 50 nm radius having a refractive index of 1.56 was moved along the direction of the beam, directly above the circular aperture of the PEC. A coarse uniform mesh with $dx = dy =$ 25 nm and $dz =$ 1 nm was initially set in the simulation region. To improve accuracy, however, a mesh override was used. The mesh override region was designed to match the dimensions of the TFSF source. For this mesh override, $dx = dy =$5 nm while $dz =$ 0.25 nm. The mesh refinement setting in the simulation region was set to the conformal variant 1 type. The dt stability factor was set to 0.95, the time step to 0.0031638 fs and the minimum step size to 0.025 nm. Two 2-D monitors of the frequency domain field and power type were used. One z-normal monitor was fixed at z = 0 and measured the transmission while another x-normal monitor was fixed at x = 0 and measured the E-field. The z-position of the dielectric sphere was varied in steps of 10 nm

from 51 nm to 261 nm, and for each position of the dielectric sphere, the transmission, T, and the E-field were recorded with and without the particle. The intensity at the desired wavelength (500 nm) was extracted from the record of intensity versus wavelength and the trapping potential, U, was computed in accordance with (5.18). Figure 5.4 below shows a yz-section of the simulation setup.

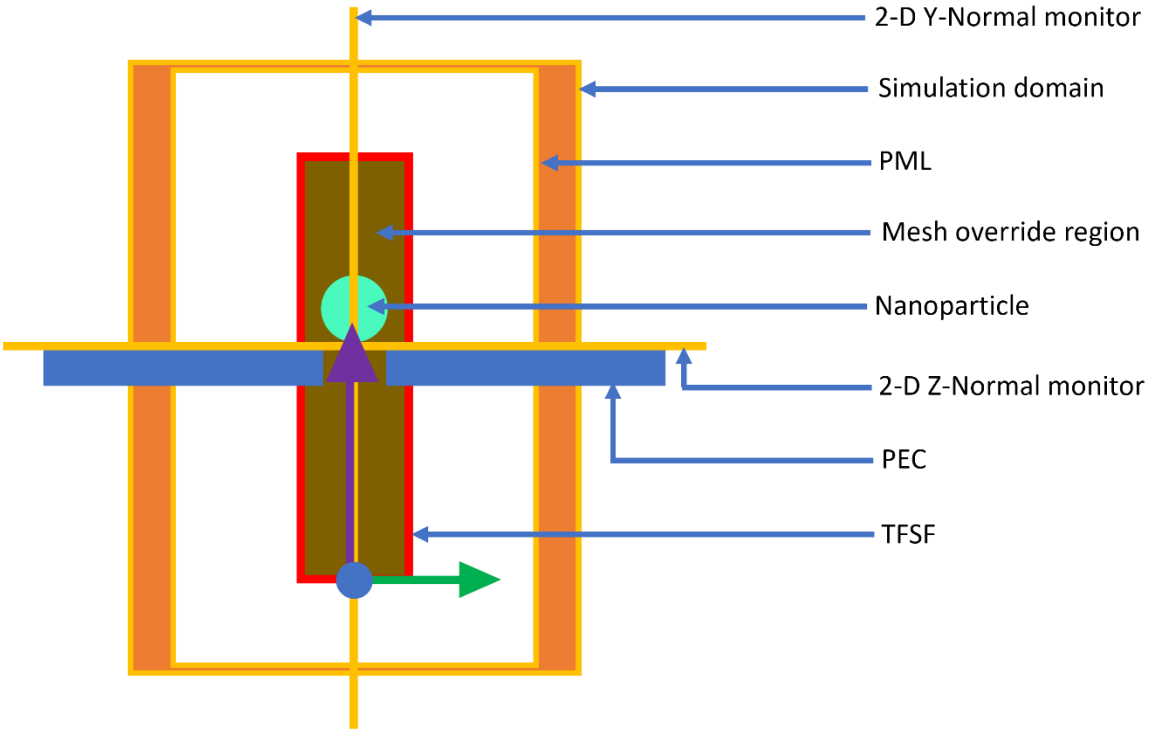

Figure 5.4: yz-section of simulation setup. Copyright: Optica Publishing Group.

Figures 5.5 A-D below show the distribution of the magnitudes of the electric and magnetic fields with and without the nanoparticle.

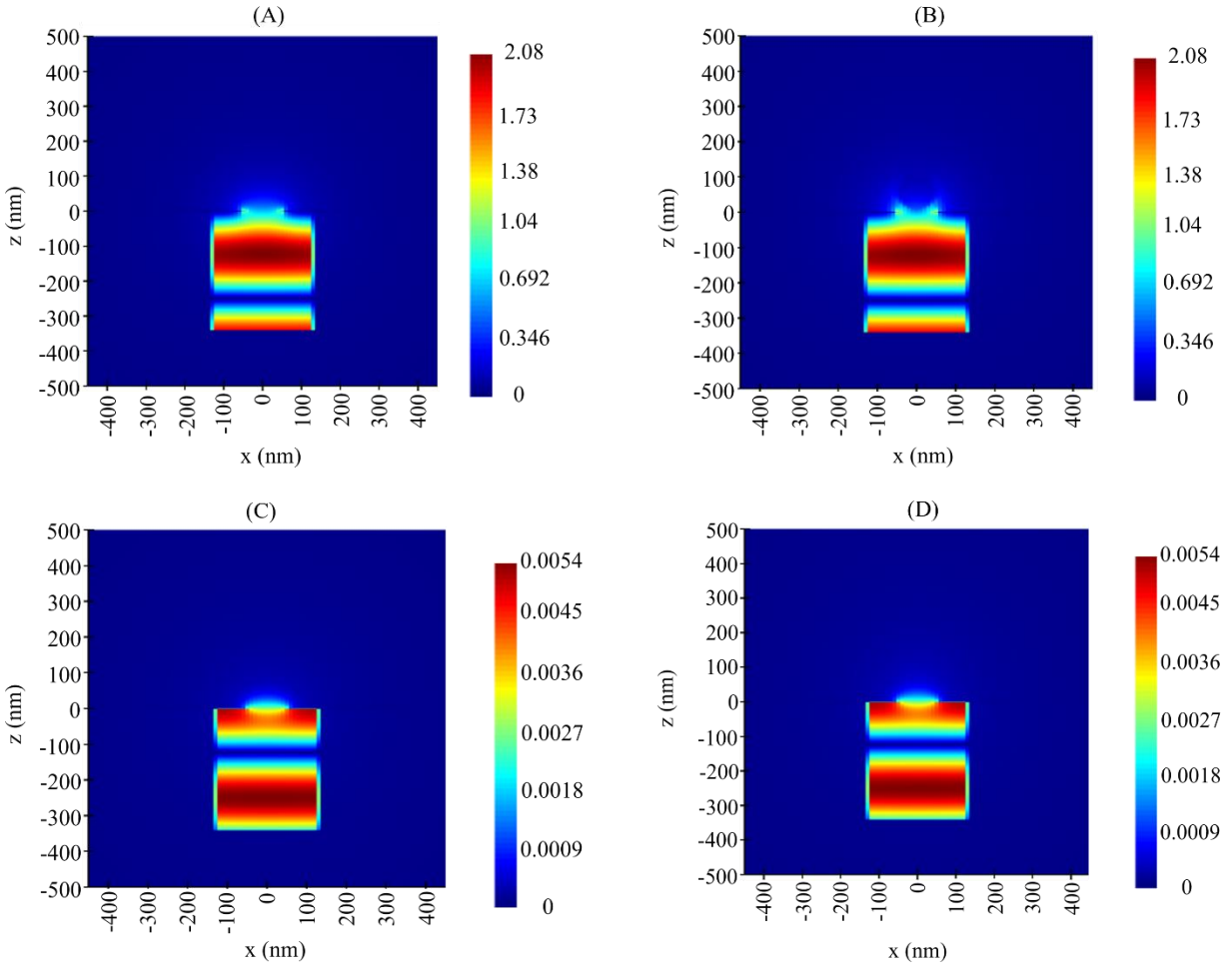

Figure 5.5: (A) Distribution of $\left|\vec{\boldsymbol{E}}\right|^{\mathbf{2}}$without SIBA. (B) Distribution of $\left|\vec{\boldsymbol{E}}\right|^{\mathbf{2}}$wit SIBA. (C) Distribution of $\left|\vec{\boldsymbol{H}}\right|^{\mathbf{2}}$without SIBA. (D) Distribution of $\left|\vec{\boldsymbol{H}}\right|^{\mathbf{2}}$without SIBA. Copyright: Optica Publishing Group.

The numerically computed transmission as a function of r is shown as the solid olive-green curve in Figure 5.2 above, while the difference between the numerically computed trapping potentials with and without SIBA is shown as a solid olive-green curve in Figure 5.3 above.

5.5 Discussion

Quantitative agreement between theory and simulation is found in this study, thus providing support that the dipole theory captures the relevant SIBA physics for this geometry. While off-axis excitation is possible, we will need to include electric dipole at the aperture that is normal to the aperture, so we have left it out in this simple theory to keep things as clear as possible. We moved the particle off-axis in the simulation and found a slight increase in the transmission of less than 1 % and an increase in the difference in trapping potential relative to the no-SIBA case of about 2 % above the on-axis value for every 5° tilt at a wavelength of 500 nm. For normal incidence, as in the current study, the first order effect is the magnetic-electric dipole interaction considered.

As can be seen from Figures 5.2 and 5.3 above, SIBA enhances both the transmission and the trapping potential. In particular, about 17 % increase in the transmission and about 28 % increase in the difference in trapping potential relative to the no-SIBA case can be observed in Figures 11 and 12 above. The enhancement shown explains the already known and exploited ability of aperture tweezers to work at lower optical intensities, a quality which makes them useful for trapping photosensitive samples.

The observation of SIBA with a PEC is interesting because it indicates that surface plasmons are not necessary, whereas it does not deny the existence of plasmons in real systems. Surface plasmons are particularly interesting close to the plasmonic resonance, which is not of primary interest for this off-resonance work. Shaping the aperture can also be captured within the present theory by using the effective magnetic polarizability of a shaped aperture.

The Bethe polarizability in the present model does not account for plasmonic resonance effects. Plasmonic resonances can shift the peak in the transmission, and the corresponding polarizability for larger apertures (for example, [198], [199]). It is possible then to consider that this theory can be modified to include these resonance effects; however, the simple Bethe theory does not present any resonance peak (in fact, it over-estimates the transmission for larger apertures due to the strong power scaling). The polarizability of the nanoparticle does contain implicitly the Frölich resonance condition that accounts for the plasmonic resonance of the particle, but that is not explored in this work.
The plasmon resonance of apertures in real metals are around 300 nm and in the visible regime for vacuum and Ag [200] and in the infrared for supported apertures in Au and in water [65]. At much longer wavelengths, the transmission through the aperture is better represented by a Bethe theory than the tail end of a Lorentzian, so we believe that the present theory would be better suited for that regime.

While equal nanoaperture and particle size was chosen as a starting point in this study to ensure that we were in the dipole limit for both the particle and aperture, we attempted different geometries as well. For example, doubling the aperture radius increased the change in transmission (normalized to the no-particle case) by over 5 times, and the potential increased by 64 times.

In this work, we have shown that there is a SIBA contribution within Bethe-Rayleigh theory for a particle-aperture system. By monitoring the transmission changes, it is possible to get information related to the particle size and position, which has already been done in experiments to size proteins [138]. It is also possible that this can be applied to tracking [201], and possibly to near-field polarization mapping [202]. To achieve polarization and full

position tracking, the present theory should be extended to include off-axis positions (including the electric dipole of the aperture as well).

While the agreement between analytical and numerical solutions found in this study is close, it is not exactly spot-on. Since we performed a convergence study and found that the solution was fully converged (showing negligible variation with smaller mesh sizes) for the simulation parameters used, we believe that the differences remaining between theory and experiment are the result of the dipole approximation made in the theory.

5.6 Conclusion

Here we have shown the most basic description of SIBA in an aperture system that uses an effective magnetic dipole of the aperture and the electric dipole of a particle within the interaction range of the aperture-particle system. The magnetic dipole of the Bethe aperture creates an electric field, which polarizes the electric dipole of the Rayleigh scatterer, which in turn creates a magnetic field back at the aperture. This can enhance the transmission and trapping potential significantly for the non-resonant case and benefit trapping. This simple theory may be extended to different aperture shapes, or different locations of the aperture with respect to the particle (and perhaps even multiple apertures or multiple particles).

Chapter 6

Impact of Point Mutation on PR65 Shape Using DNH Optical Trapping Signals

6.1 Chapter Overview

This Chapter applies much of what has been discussed so far in this work to studying the effect of mutations, and in particular point mutations, on the shape of the PR65, as the α-subunit of protein phosphatase 2A (PP2A) is known. PR65 wild type is studied along with six of its mutants. Results found show that, relative to PR65 wild type, certain mutants of PR65 are elongated while others are shortened when exposed to optical tweezer force. This provides a relatively simple and inexpensive method of tracking mutations in proteins by way of changes in their contour length.

6.2 Introduction

Proteins are not only the building blocks of life, but also represent the lowest level at which the physical manifestation of biological mutations [203] are usually noticeable [204]. The way that a protein functions and interacts with other proteins and non-protein biological molecules is critically tied to its shape or structure [205], [206], [103]. This underscores the importance of studying the impact of mutations on the shape of a protein like PR65 – the A-subunit of protein phosphatase 2A (PP2A) [103], which has been implicated in Alzheimer's [207], [132], and cancer [129], [156], [128].

Multifarious techniques have been, and continue to be, developed for interrogating protein conformation changes. Examples include fluorescence correlation spectroscopy [208], which can provide information on changes in protein conformation via measurement of the hydrodynamic

radius [167]; single molecule fluorescence energy transfer [209], which utilizes the distance dependence of Förster resonance to study conformational changes in proteins by attaching donor and acceptor chromophores at a single location on a protein and measuring the efficiency of the fluorescence resonance energy transfer between the chromophores, which provides direct information about the separation between the chromophores as the protein to which they are attached undergoes conformation changes [168]; single molecule force spectroscopy [210], in which tension or compression forces applied to a single protein molecule through tethers at two adjacent locations on a protein provide insight into the mechanical properties of a protein, such that the response of a protein to being altered or, equivalently, feedback from a mechanically altered protein can be used to monitor and to detect conformational changes undergone by a protein [169]; nanopore electro-osmotic trap (NEOtrap), in which a process known as electro-osmosis involving hydrodynamic flow of ions under a spatially uniform electric field through a porous origami-DNA sponge, or similar structure, adsorbed to a solid state membrane across a nanopore is used to drive a single protein molecule towards the origami-DNA molecule to which the protein then gets attached, producing a signature drop in ionic current that is used to interrogate physical properties of a protein as well as any conformational changes which may be undergone by a protein [121]. As well as these, another technique which has been used to conduct biophysical assays, and which has shown tremendous potential, if not superiority in some respects among other single molecule techniques, is the plasmonic double nanohole (DNH) aperture tweezers. This technique, unlike most, if not all, of the foregoing ones, does not require the use of molecular tethers or labelling, which not only increase cost and complexity, but can also introduce artifacts that can mask effects that one is trying to investigate or lead to erroneous results either by changing the intrinsic properties of a protein [211], [212] or forming a complex

with the protein that behaves differently from the protein [213]. To date, the DNH has been used to study the unfolding of single bovine serum albumin (BSA) molecules [115], the unzipping of DNA-hairpins and the interaction of these DNA-hairpins with proteins [33], the sizing of proteins [138], the binding of antibodies to specific proteins [126], [214], the interaction of proteins with ligands [136], [137], among several other applications that demonstrate the potential of the DNH for single molecule studies.

Here, specifically, we investigate the impact of point mutations on the shape of PR65 wild type and six (6) of its mutants using DNH optical trapping signals. Our choice of the DNH optical tweezers for this study is predicated on what has already been said, for example in chapter 3 and earlier in this chapter, but also on the fact that the DNH is cheap and easy to fabricate and to use [96], even as it yields results in real time. Furthermore, while the loss of sample fidelity due to denaturation caused by heating is an issue that is frequently a source of concern in the use of optical trapping techniques for studying biological samples [215], the plasmonic effect [6] and the self-induced back action (SIBA) effect [65], [1] allow for trapping with considerably lower optical intensities in plasmonic DNH tweezers, which thus produces less heat as a consequence; even the little heat generated is conducted away by the metal part of the plasmonic nanotweezers [6], the consequence of which is that sample damage due to heating is avoided in plasmonic DNH optical tweezers. Again, the enhanced isolation capability of the nanotweezer system due to its much smaller trapping volume eliminates the need for highly purified samples [116], leading to a further reduction in cost. Furthermore, the nanoplasmonic DNH optical tweezers has also shown greater sensitivity when compared to other techniques such as nanopore [126].

It has been shown [216] that point mutations can produce larger-than-average structural changes in proteins. We provide experimental evidence of such a structural change in PR65 involving a change in its shape – compacted versus elongated – by comparing the root mean squared deviation (RMSD) and corner frequency for PR65 wild type and six (6) of its mutants computed from the time trace of the signals acquired by trapping each of these in a DNH optical tweezers. The hypothesis underpinning the work is first presented. This is followed by a description of the experiment performed to test the hypothesis. The results obtained from the experiment are then presented and, lastly, an analysis of those results to show how well they support our hypothesis.

6.3 Hypothesis

If conformation changes induced by substitution mutations alter the material polarizability of PR65, then the DNH tweezer signal acquired by trapping each mutant of PR65 will have a different root-mean-square-deviation (RMSD) and corner frequency from that of wild type PR65.

To understand the rationale behind this hypothesis, imagine a dielectric sphere suspended in a fluid such as water being trapped in the cusp of a DNH such as that in Figure 4.2 of chapter 4. Imagine that the dielectric sphere experiences an optical force which elongates it into a spheroid. This will cause the polarizability of the elongated dielectric spheroid to increase relative to that of the original dielectric sphere while also reducing the hydrodynamic drag on the elongated spheroid, since narrower objects like arrows experience less drag than balls, for example. The increase in polarizability of the elongated sphere will result in it experiencing a stiffer trapping force in accordance with $\vec{F}_{grad} \propto real(\alpha)\nabla I$, where $\vec{F}_{grad}$ is the trapping (gradient) force, $real(\alpha)$ is the real part of the polarizability, α, and ∇I is the intensity gradient. For a dielectric

the imaginary part of the polarizability is negligible. The trapped particle undergoes Brownian motion, and the effect of a stiffer trap force is a reduction in the root-mean-square-deviation (RMSD) of the trapped particle due to increased confinement. Meanwhile, the trap stiffness, $k \propto real(\alpha)\nabla^2 I$ increases while the hydrodynamic drag, γ, decreases with the result that the corner frequency characteristic of the trapped particle's Brownian motion, $f_c = \frac{k}{\gamma}$, increases. If, on the other hand, a trapped particle, in response to the optical force, assumes a more compact shape than the one described, then the RMSD and the corner frequency go in the opposite direction, with the RMSD increasing and the corner frequency decreasing. The foregoing hypothesis is realized simply by replacing the dielectric particle in this thought experiment with a protein molecule such as PR65.

6.4 Method.

The optical trapping experiment was conducted by first making a microwell on a clean glass microscope slide of 150 μm thickness (Ted Pella, Inc.) using an imaging spacer (Secure Seal imaging spacer, Grace Bio-labs) to form an open chamber measuring 120 μm in depth and 9 mm in diameter. With a micropipette, this chamber was filled with 10 μL of the analyte, diluted to 10 μM from an initial concentration of 200 μM. A sample of gold-on-glass with double nanohole (DNH) apertures fabricated on it by colloidal lithography, was inverted over the microwell chamber to seal it off. Figure 6.1 below is a step-by-step cartoon of the assembly process.

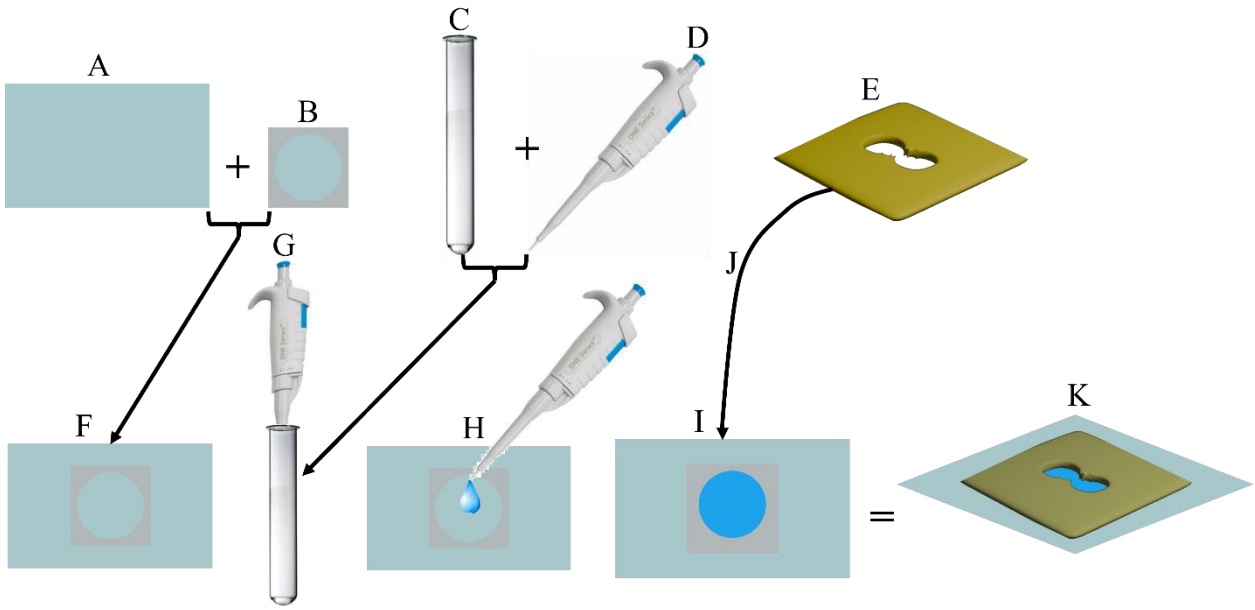

Figure 6.1: A. Clean glass microscope slide. B. Image spacer. C. Test tube containing solution of PR65 in phosphate-buffered saline. D. Micropipette. E. DNH in gold. F. Microwell. H. Introducing 10 µL of 10 µM dilute PR65 solution into microwell using a micropipette. I. 10 µL of 10 µM dilute PR65 solution in microwell. J. Inverting DNH over microwell to seal it off chamber. K. Completed sample ready for placement on sample stage for trapping experiment.

The microwell chamber sealed off with the gold-on-glass structure containing the DNHs was then carefully placed on a 3-axis piezo-controlled stage between a 1.3 NA 100× oil immersion objective and a 10× collection objective such that the underside of the microscope cover slide bearing the microwell was in contact with the oil immersion objective. By slow counterclockwise rotation of the z-knob of the 3-axis piezo-controlled stage, the sample mounted on the stage was brought to the confocal position between the oil immersion objective and the collection objective. Thereupon, multiple bright spots – corresponding to apertures on the gold-on-glass sample within the area of illumination of a light emitting diode (LED) which sent light through the apertures, which transmission was captured by a charge-coupled device (CCD)

camera – could be seen on the screen of a computer connected to the CCD camera. Using the x- and y-knobs of the 3-axis piezo stage, the DNH-bearing structure was moved over the LED beam so that the center of one of the observed spots coincided with the location of a colored tape strip used as a marker on the screen of the computer connected to the CCD camera. The LED was then turned off, and a 980 nm laser was focused through the 1.3 NA, 100× oil immersion objective to a diffraction limited spot through the selected aperture. The transmission through the aperture was monitored using an avalanche photodiode (APD) (with a 1.3 optical density (OD) filter placed in front of it to prevent its saturation). The laser was first turned on to a very low power (1.2 mW, for example) and, using the x-, y- knobs of the piezo-controlled 3-axis stage, the DNH-bearing gold-on-glass structure was moved on a horizontal plane to until the center of the laser spot coincided with the location of the colored tape strip used as a marker on the screen of the computer connected to the CCD camera. A half-wave plate (Thorlabs, WPH05M-980) mounted on the laser path was then used to verify if the selected aperture was a DNH by rotating the half-wave plate and observing the change in the APD signal, acquired using a USB-4771A data acquisition module from Advantech. The USB-4771A data acquisition module was connected to the same computer as the APD. The readout from the USB-4771A data acquisition module was viewed on the screen of this computer. For a DNH, the change in APD between 30 % and 50% was expected [146] with rotation of the half-wave plate because of the polarized nature of the DNH transmission, unlike other aperture configurations such as the single nanohole, the triangular triple and the square quadruple nanoholes which all show relatively negligible change in transmission with the rotation of the half-wave plate. The APD typically reads around 1.2 V – 1.6V at the minimum transmission polarization and between 1.56V – 1.8V and 2.1V – 2.4V at the maximum transmission polarization for a DNH. If an aperture did not

pass this test, a different one was selected by the same procedure and the test was repeated until a DNH was found. The laser power was then increased to 22.5 mW before the 100× oil immersion objective, and trapping, identified by a discrete jump and an increase in APD signal noise of at least 10%, was awaited. The data, acquired at a 100 kHz sampling rate over a duration of 5 – 10 s, was exported to MATLAB (or any other suitable scientific computing software) as a 2×500000 or 2×1000000 matrix for further analysis. Figure 6.2 below shows a schematic of the experimental setup while an exemplar trapping signal is as shown in Figure 6.3A below. The experiment was repeated at least 10 times for PR65 wild type and each mutant.

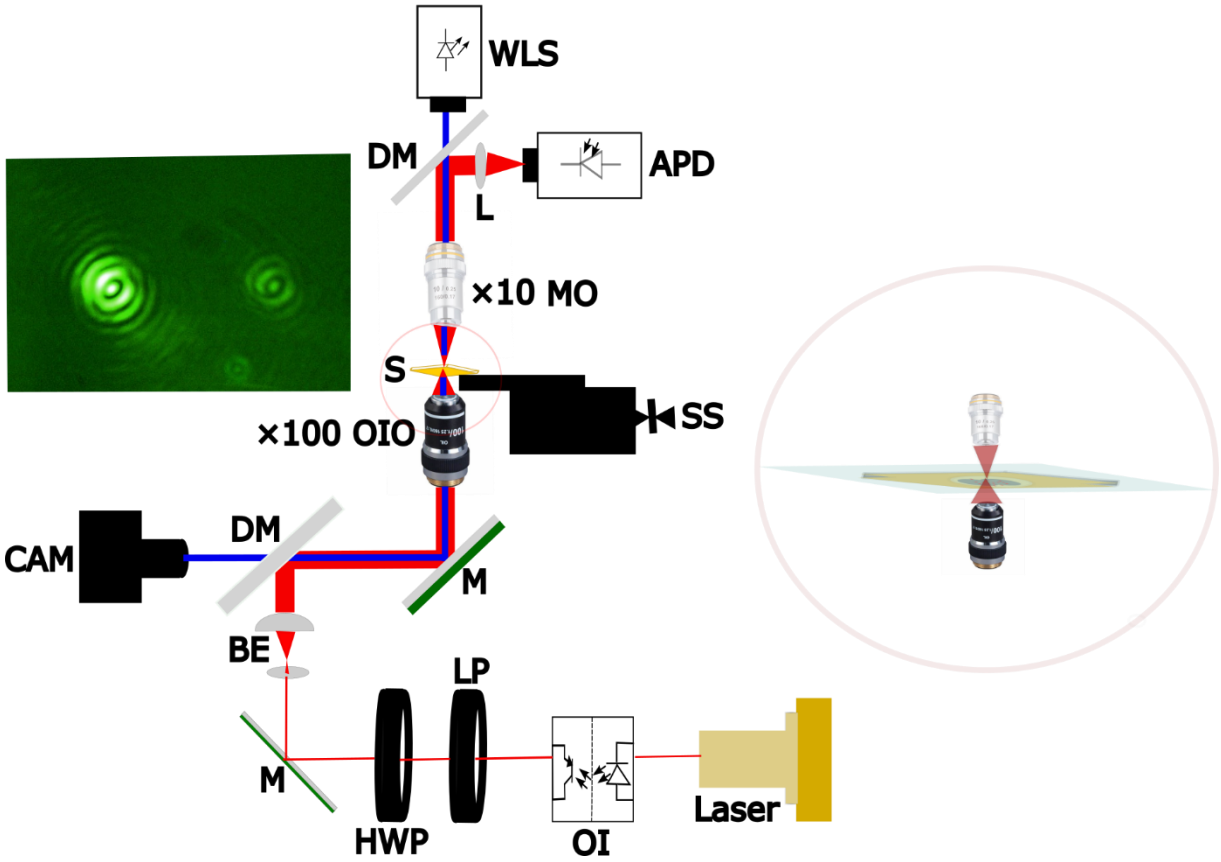

Figure 6.2: Schematic of experimental setup. WLS is a white light source; DM stands for dichroic mirror; APD stands for avalanche photodiode; L is a lens; MO stands for microscope objective; S is the sample; OIO stands for oil immersion objective; SS is the sample stage; CAM is a camera; M stands for mirror; BE is a beam expander; HWP is a half wave plate; LP is a linear polarizer; OI is an optical isolator. Top left inset shows the diffraction pattern seen when the laser is focused through the sample while center right inset shows how the laser light is focused through the sample by the OIO and collected by the MO. Throughout, magnifications are shown by the × symbol followed by a number to the left of an objective, e.g., ×10 MO indicates a microscope objective with a magnification of 10.

6.5 Results, Analysis and Characterization of PR65 and its Variants.

When it is trapped, the optical signal from the trapped PR65 (wild type or mutant) molecule exhibits a characteristic step in the APD signal coincident with the entry of the PR65 molecule into the optical trap, and an increase in the noise amplitude, as can be seen in Figure 6.3A. That this signal is from a single molecule is deduced from past studies. For example, [126] combined the DNH with a nanopore, which has a verified single molecule signal, and observed that the signal from the DNH was consistent with single molecule events from the nanopore. Similarly, molecular weight sizing of proteins achieved by [138] via monitoring the transmission signal of the DNH was found consistent with single protein sizes. The dark portion of the plot is the signal prior to trapping the molecule. The mean of a 0.5 s long portion of this part of the signal was used to normalize the entire signal to ensure that repeated measurements are not affected by small variations in the adjustments of the x- y- z-knobs of the piezo which align the DNH to the center of the laser beam. The grey portion of the plot is the signal corresponding to a molecule's trapping event. A 2 s long portion (green portion of plot) of this, necessary for accurately computing the corner frequency without minimal cost in computer memory [217] was selected such that it terminated 1s away from the end of the trapping event to ensure that the trapped particle is in steady state [90] – far away from the start of the of the trapping event and not too close to where the laser is blocked off to untrap the molecule. The corner frequency and RMSD are computed using this section. To compute the corner frequency, a Hanning-windowed discrete Fourier transform (DFT) was used to compute the power spectral density, and a portion of this corresponding to a lower cut-off frequency of 10 Hz and an upper cut-off frequency of 1.38 kHz – to avoid aliasing – was fitted with a Lorentzian of the form,

$$y(f) = \frac{A}{1 + \left(\frac{f}{f_c}\right)^2} \tag{6.1}$$

where y is the PSD, f is the frequency, A and f_c are free parameters, with f_c being the desired corner frequency. The fit is done by means of a non-linear least square method, with initial estimates for A and f_c being two Gaussian random numbers generated in MATLAB which were then refined using an iteration scheme that returned final values for A and f_c which minimized an objective function associated with (6.1), which was then fitted using the found values of A and f_c together with values for f. This is shown in Figure 6.3C below. To compute the RMSD, the portion of DNH was fed to the MATLAB function histcounts with the normalization parameter set to 'probability'. This returned a histogram of the DNH signal. The centers of each rectangle of the histogram were read and these together with the returned probabilities were used to compute a Gaussian envelope to the histogram of the form,

$$p(z) = Bexp\left(-\frac{(z-\mu)^2}{2\sigma^2}\right) \tag{6.2}$$

where p is the probabilities returned by 'histcount' from the DNH signal fed to it, z is the values corresponding to the centers of the rectangles of the histogram returned by 'histcounts' while B, μ and σ are fit parameters, with σ being the sought RMSD. As with the computation of the corner frequency, a non-linear least square method was used to obtain values for B, μ and σ. First, z was fed to the MATLAB function 'normfit' to obtain initial estimates for μ and σ. An initial estimate for B was chosen as the mean of the maximum and minimum values of p previously returned by 'histcount'. These initial estimates were refined in an iterative scheme that returned final values of these parameters which minimized an objective function associated

with (6.2). To remove contribution to the RMSD by noise from the pre-tap stage (dark segment of Figure 6.3A below), the trapping signal was filtered using a low pass finite impulse filter (fir) with a cut-off frequency twice the corner frequency from the PSD computation. This was implemented in MATLAB using the built in 'designfilt' routine. The Gaussian envelope in Figure 6.3B was computed using this difference in RMSD of the pre-trap signal and the trapping signal just described together with values of B, μ and z.

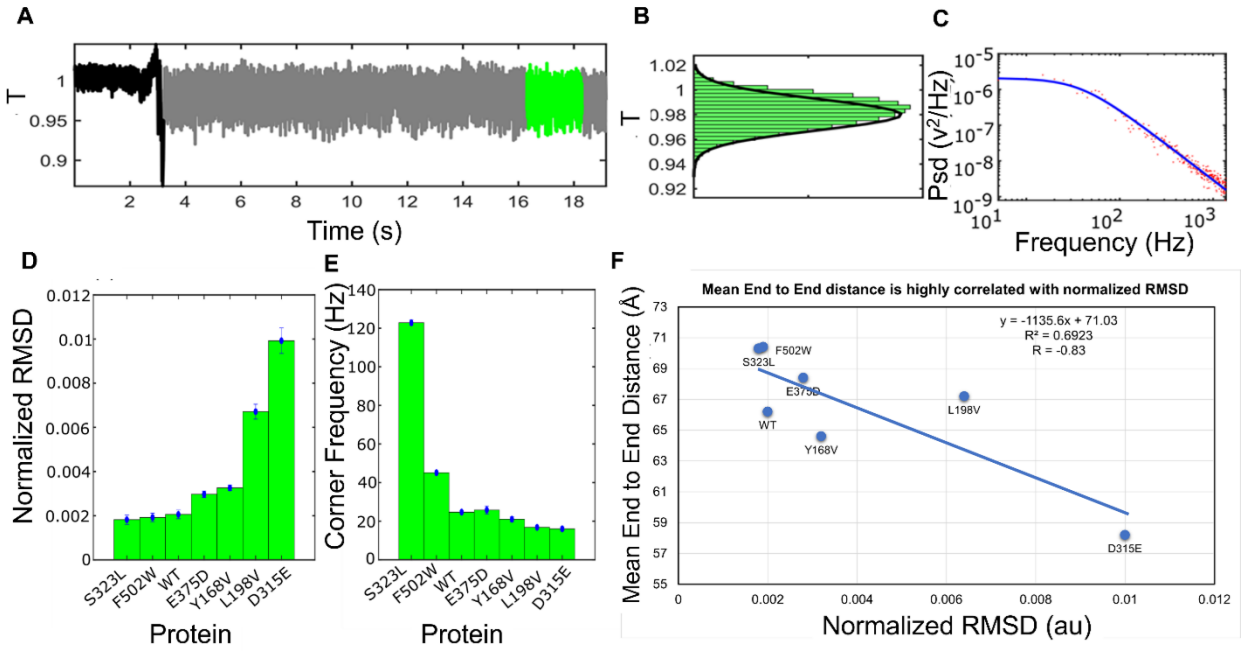

Figure 6.3: Tetherless aperture-based nanoplasmonic tweezers enable characterization of the structural dynamics of PR65 and single-site mutants. (A) PR65 undergoes a characteristic step as it enters the double nanohole trap, followed by an increase in noise from Brownian translational motion. (B) A histogram of this noise (transmission through the aperture, T, normalized to the pre-trap level) sampled after the trapping event. (C) The power spectral density from the detected transmission of PR65. (D) Root-mean-square deviation and (E) corner frequency of the amplitude of the noise for WT PR65 and the six mutants. (F) The mean end-to-end distance

observed across 1.5 μs of molecular dynamics simulation for WT PR65 and the six mutants report a Pearson correlation coefficient of -0.83 with the normalized RMSD.

This was repeated for each trapping event for wild type PR65 and each of its mutants studied.

Table 6.1 below shows mean values of the RMSD and corner frequency for each of these together with their standard deviations.

Table 6.1: Mean corner frequencies and normalized RMSDs for PR65 wild type (WT) and mutants.

protein	mean corner frequency (Hz)	standard deviation (Hz)	mean normalized RMSD	standard deviation
S323L	122.8180	5.3987	0.0018	0.0009
F502W	45.0714	2.0035	0.0019	0.0007
WT	24.6624	2.9474	0.0021	0.0009
E375D	25.7502	5.8874	0.0030	0.0007
Y168V	20.9672	4.2953	0.0033	0.0006
L198V	16.7766	1.2493	0.0067	0.0015
D315E	15.9921	3.1029	0.0099	0.0028

Figures 6.3 D and E above are histograms of the values of the corresponding variables in Table 6.1 above and the error bars in Figures 6.3 D and E above represent the standard deviations of the corresponding variables shown in Table 6.1. To further support the hypothesis that the differences observed in our DNH optical tweezer measurements were related to differences in conformational changes in the proteins, a linear correlation was computed between the RMSD

from our DNH aperture tweezer measurement and the mean contour lengths of each protein from molecular dynamics simulations performed by Mert Gur's groups at both the Istanbul Technical University, Turkey and the University of Pittsburgh, USA. As shown in Figure 6.3, a strong negative correlation existed between the two, showing that elongated conformations corresponded to lower RMSDs in agreement with the hypothesis. The choice of the RMSD instead of the corner frequency for this comparison is informed by the fact that RMSD depended solely on the confinement of the protein in the trap which, in turn, depended solely on the protein through its material polarizability whereas the corner frequency depended on the fluid in which the protein is suspended as well through the drag constant and thus less directly on the protein in comparison to the RMSD. Table 6.2 below shows the mean contour lengths of the proteins from molecular dynamics simulation used in making Figure 6.3F.

Table 6.2: Mean count lengths of PR65 WT and mutants from molecular dynamics simulations. Source: Mert Gur, Istanbul Technical University, Turkey and University of Pittsburgh, USA.

protein	mean contour length (Å)	standard deviation (Å)
S323L	70.3	9.4
F502W	70.4	9.9
WT	66.2	9.8
E375D	68.4	8.9
Y168V	64.6	11.2
L198V	67.2	9.7
D315E	58.2	15.6

The explanation for these results is follows. When trapped, the Brownian motion of the particle causes the "noise" seen in the APD signal (corresponding to the normalized

transmission, T, through the aperture, normalization being with respect to the pre-trap level of the APD signal) to increase. The greater the stiffness associated with the optical tweezer potential, the lower the amplitude of the Brownian motion of the particle [110], so a lower amplitude of the corresponding "noise" seen in the APD signal, measured by the root mean squared deviation (RMSD) of the acquired signal, is expected for a larger stiffness of the optical trap. The stiffness of the optical trap is proportional to the trapped particle's material polarizability, which is larger the longer a particle is, so that a lower RMSD is expected if a protein is elongated by a point mutation. Furthermore, the trapped particle is a thermally driven oscillator subject to the viscous drag of the fluid in which it is suspended. Consequently, it will oscillate with a range of frequencies, among which the energy of the particle's motion would be distributed according to the power spectral density which, as theory [218] shows in this case, is a Lorentzian of the form (6.1), characterized by a corner frequency, f_c, given by the ratio of the trap stiffness to the hydrodynamic drag on the proteins [110]. Not only does (6.1) not involve any inertial contribution, due to this being negligible [55], but also PR65 WT and its mutants studied in this work have very near identical molecular weights and, prior to being trapped, charge distributions. Accordingly, differences in the stiffness of the optical trap potential experienced by each protein must be due to differences in the material polarizability of the proteins resulting from their differences in conformational stability. Furthermore, regardless of how the viscous drag changes with the change in protein conformation, the trapping potential is generally higher than the thermal energy of the surrounding fluid (at least 10 times as much for a functional optical trap [43], [63]) and, for microscale objects, polarizability is more sensitive to changes in shape than the drag [214]. Consequently, the optical trap stiffness generally follows the polarizability of the trapped protein, and, as such, the corner frequency which, as has been

defined, is the ratio of the trap stiffness to the viscous drag, is expected to increase as the particle elongates, as opposed to the trend shown by the RMSD as the particle elongates.

The justification for the foregoing interpretation of the results is that point mutations are unlikely to change the physical dimensions of a protein significantly, so that all changes observed can be attributed to changes in the shape of the protein such as the way in which the protein is folded. Specifically, we distinguish elongation by unfolding from elongation by stretching. We similarly distinguish shortening by folding from shortening by compression. For example, the maximum RMSD in atomic positions observed in [210] was about 2.1 Å, which – although significant to support the conclusion that a new protein structure has emerged according to [210] – is yet less than the average contour length of an amino acid [211]; meanwhile, a single-domain protein would typically contain about 150 amino acid residues [212] – a change of less than 1 part in 600, supporting the reasoning behind the interpretation pursued in this work.

As has been explained, the acquired time trace in our experiment is related to the diffusion of the trapped protein, the characteristic of which depends on both the hydrodynamic radius and the polarizability of the protein, both of which depend on the size and shape of the protein [213], [137], as characterized by the RMSD and corner frequency of the time trace from trapping each protein. Differences in RMSDs and corner frequencies correspond to differences in material polarizability arising from differences in conformation changes corresponding to elongation or shortening, relative to PR65 WT, due to differences in conformational stability induced by different point mutations to PR65 WT.

6.6 Conclusion.

PP2A is a very important Serine/ Threonine phosphatase. It performs a central role in sustaining cellular processes and in maintaining signaling pathways. Its dysregulation has been

implicated in various human cancers, Alzheimer's disease, and decreased resistance to pathogen infections. In this study, the effects of point mutations on the structure and dynamics of PR65, a component of PP2A, have been investigated. The influence of minute alterations at specific regions of PR65 on the possible conformational changes that it can undergo in response to mechanical forces have been probed by targeting specific mutations at its hinge sites. By showing that differences in RMSDs and corner frequencies correspond to differences in material polarizability arising from differences in conformation changes corresponding to elongation or shortening, relative to PR65 WT, of point mutants of PR65 studied in this work – a result which can only be explained by these point mutants of PR65 having different conformational stabilities to the WT – our investigations seem to show that mutations at certain hinge sites, such as S323L, E375D and especially F502W, were favorable to extended conformations of PR65 while mutations at other hinge sites such as Y168V and D315E stabilized more compact forms of PR65.

The power of the DNH optical tweezers enabled the analysis of the differences in conformational changes of WT PR65 and its mutants at the single-molecule level without modifications by labels, tethers or both and the associated cost in one or more of money, time, technicality and complexity of conventional optical tweezers and other single-molecule techniques. Observed trends from comparing the DNH optical tweezer results obtained for PR65 WT with those of its mutants were consistent with molecular dynamics simulations. The mutants S323L, E375D, and F502W had the highest corner frequencies by the results of our analysis of the experimental data and indicated that these mutations resulted in larger trap stiffnesses and extended conformations while the mutants Y168V and D315E had the lowest corner frequencies, indicating that they resulted in smaller trap stiffnesses and compact forms of PR65.

We posit that the findings reported in this work may be relevant to understanding how mutations alter the function of PR65, and how these may be connected to any anatomical or physiological conditions for which PP2A has been implicated, potentially due to the impact of such mutations on the conformational flexibility and activity of the PP2A complex. These findings may also be relevant to studying the impact of mutations on other proteins, besides extending the utility of the DNH optical tweezers as a biophysical tool.

Further, as a matter of reliability, it is worth reporting that previous studies [219], [125], [220] have investigated heating in aperture systems similar to the DNH employed in the current study and indicate a temperature rise of $\sim 1° \frac{C}{mW}$ (for a diffraction limited spot size of around 1 μm^2) of laser power. In the current work, ~16 mW of laser power was incident on the sample. Accordingly, the expected temperature rise was around $16°C$ above room temperature, which was well within physiological limits. Furthermore, the same laser power and wavelength were employed for all measurements for consistency of the results.

Chapter 7

Diverse PP2A Scaffold Dynamics Observed Directly by Nanoaperture Optical Tweezers

Disclaimer: The work in this chapter is the result of a collaboration. I performed all experimental work while the data analysis and figures, apart from Figure 7.3, were made by Dr Demelza Wright.

7.1 Chapter Overview

Allostery is a term in biochemistry that refers to the presence of a physical location or locations (regulatory site(s)), other than the active site, on complex proteins to which ligands can bind [221]. Allostery comes from two Greek root words, “allos” meaning other and “stereos” meaning solid (object) [222]. Allostery is a useful mechanism for cell signalling and for cell regulation of enzyme activity [221] via protein conformational changes or changes in protein dynamics [223], [224]. Motivated by the possible link between the catalytic activity of protein phosphotase 2A and the spring-like nature of its A-subunit, otherwise known as PR65, this chapter follows up previous *in silico* analysis [103] which predicted deformation and unstacking under applied force. Nanoaperture optical trapping of individual unlabelled and untethered PR65 molecules undergoing a distinct step transition that is identified as deformation is presented. As in the previous chapter, it is observed that the trapping signal is strongly impacted by point mutations to PR65. But whereas the previous chapter dealt with the impact of mutations on the shape of PR65 using nano-optical tweezers, here the impact of mutations on the flexibility of PR65 to shape changes or, put differently, the mechanism by which the shape changes studied in the previous chapter occur, is investigated via the deformation timescale. An order of magnitude change in the deformation timescale is observed. It is further observed that telegraphing between

native and deformed states on the order of milliseconds for specific mutants can occur owing to stochastic resonance. The investigation provides a new insight into the mechanical properties of PR65 and a path to probing the biomechanical contribution to enzymatic activity.

7.2 Introduction

Understanding the structure-function relationship of proteins is a cornerstone of biomedical science. In the last few decades, interest in proteins has greatly increased due to development of new therapies (such as anti-cancer) and through development of new techniques to study these small (nm-scale) yet ubiquitous molecules. This is at the core of our study of allostery; how protein conformational dynamics underlie complex signal communication and function [225], [226]. State-of-the-art techniques now focus on measurements of single proteins to reap benefits such as small sample requirements and resolving heterogeneity, though many still rely on indirect measurements (via fluorescent tags) and protein modification by tethering that can have unpredictable impact on protein motion. Label and tether-free optical measurement of proteins has been repeatably demonstrated by the DNH optical tweezer method. Herein, DNH optical tweezer is used to observe the dynamic motion of a scaffold repeat protein and the impact of mutation on conformational stability of PR65.

We select PR65, the scaffold subunit of protein phosphatase 2A (PP2A), because of its role in regulating the function and activity of PP2A [103], which is involved in many cellular activities and which dysregulation has been associated with the development of cancer [227]. PR65 was previously shown in molecular dynamics simulations to undergo viscoelastic deformations in response to forces that occur in living systems [103], as well as unstacking conformational changes [103]. The flexible nature of PR65 and its ability to unstack and deform can modulate

the enzymatic action of PP2A [228], [229]. Understanding and modulating these properties is key to understanding PP2A activation in anti-cancer therapies [128].

Despite PP2A being one of the most abundant enzymes in the human body, there has been no direct experimental evidence of the mechanical properties of PR65, likely due to its small size (~10 nm) being near or below the resolution of most protein pulling methods [230], [231]. We provide the first experimental evidence of these deformations by single protein measurements in DNH optical tweezers. We further demonstrate that (as predicted) the behavior of these deformations can be subtly tuned through substitutions on mutant versions of the protein.

7.3 Methods

A schematic of the experimental setup used for this work is shown in Figure 7.1a below. A laser diode focused onto samples through a microscope objective while the transmitted light is collected through a second objective and measured on an avalanche photodiode. Exemplar scanning electron microscopy image of a double nanohole aperture is shown in Figure 7.1b below. Trapping events are identified by monitoring the transmitted laser light through the aperture for a sudden increase (or for some experiments decrease) in transmission and simultaneous increase in signal variation, often measured by RMS of the captured aperture transmission [120], [138], [139].

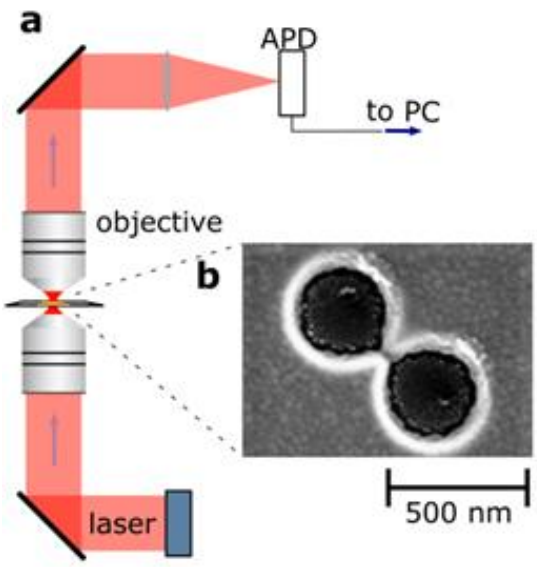

Figure 7.1: Optical trapping with DNH. a. Optical setup schematic showing laser focused onto sample and collection. b. Representative scanning electron microscope image of a DNH.

Double nanohole samples were prepared as in past work using 500 nm polystyrene particles as template [96], [146], resulting in a cusp separation of 27 nm and hole diameter of 350 nm. The sample was cleaned with hexane between runs. After a few runs samples were cleaned with a plasma etch to remove the stuck proteins from the surface. The concentration of 10 μM was used for all the proteins in 0.01 M phosphate buffer and 2 mM dithiothreitol. Trapping was performed with an optical tweezer setup modified from Thorlabs OTKB with 980 nm laser diode. The laser power was maintained at ~ 22 mW, measured just before the lower microscope objective in Figure 7.1 a above.

7.4 Results and Discussion

PR65 displays additional features in its trapping profile as shown in Figure 7.2 below. A sharp dip in the transmission (II) is followed by an increase that plateaus at an intermediate step (III)

before final transition to a higher level (IV). The intermediate step time (sometimes multiple steps) varies between 35 ms and 1 s, with a mean value of 380 ms. The final trap step remains indefinitely until the protein is released from the trap by blocking the laser beam.

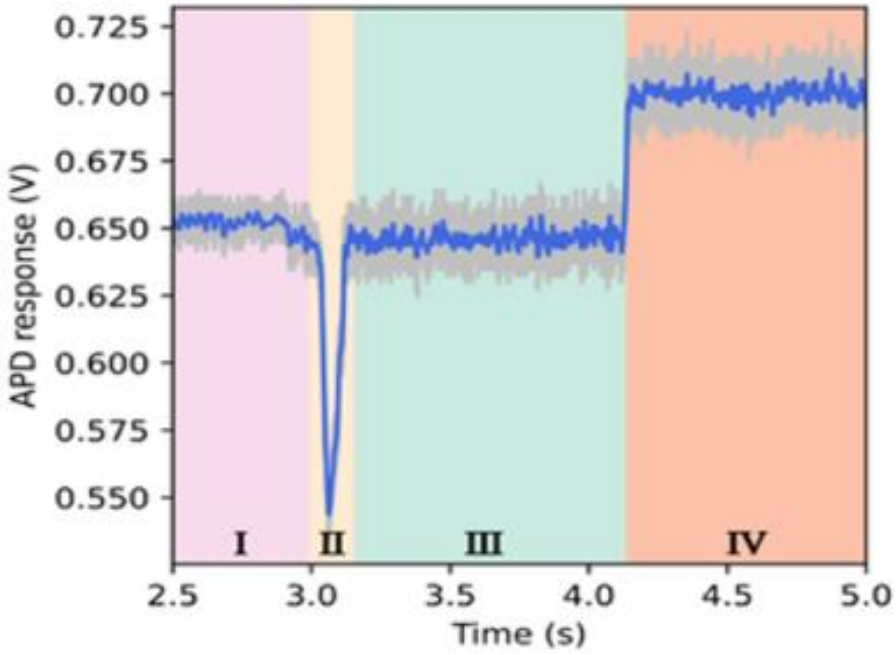

Figure 7.2: PR65 WT trapping event with regions highlighted in color: Untrapped (pink, I), sharp dip (yellow, II), intermediate step (green, III), final step (orange, IV).

These events are associated with the trapping of a single protein which has been confirmed by several works [139], [232], [233], including those with nanopores where a separate nanopore signal is obtained to confirm the single particle nature [234]. Once a single protein is trapped it is unlikely that a second protein will enter the trap due to electrostatic repulsion [116], [120]. As further confirmation, single protein trapping has enabled the accurate sizing of individual proteins based on their dynamic motion [138].

Previous works have shown that when a protein has multiple conformations, differences in polarizability can result in discrete steps in the trapping signal [138], [115]. For example, BSA transitioning between N and F forms [115], enzyme action [137], or small molecule binding [137]. We attribute the steps seen in this work with similar transitions that occur spontaneously in the dynamics of PR65.

The viscoelastic properties of PR65 have been modelled previously [103]. In that work, PR65's repeat units were shown to undergo unstacking in response to (physiologically accessible) pulling forces around 150 pN; an important result given PR65's role in PP2A as a mechanical linkage between substrate binding and catalytic subunits. The result of our experimental measurements presented here seem to be consistent with this, although as discussed below the magnitude of the force in our experiment was much smaller than 150 pN, and might well mean that a different mechanism accounted for the deformation observed in our experiment, or perhaps studying PR65 in an aqueous environment in lieu of air as in the numerical study allowed the same deformation mechanism reported in [103] to obtain in our experiment, albeit at a much lower axial force.

Past *in silico* works used 150 pN applied over 2 nm to cause PR65 unstacking, corresponding to an energy ~3 $\times 10^{-19}$ J which is ~100 k_BT [103]. Those works calculated that unstacking occurs in ~50 ps. We observe significantly longer (7 – 9 orders of magnitude) unstacking times, which show that a much smaller force is being applied in our experiments. While stable trapping occurs for ~10 k_BT (Ashkin's criterion) [42], the long timescale of the unstacking compared to past calculations suggests that we are applying a negligible force compared to those works and that the transitions are driven by normal stochastic motion with a relatively small bias from electrostriction (also of the order of 1-10 k_BT). The order of magnitude quoted for the

contribution from electrostriction is based on the fact that the computed power spectrum, as shown in Figure 7.3 below, is Lorentzian, indicating a weak trap [61] with a potential within the Ashkin criterion [39].

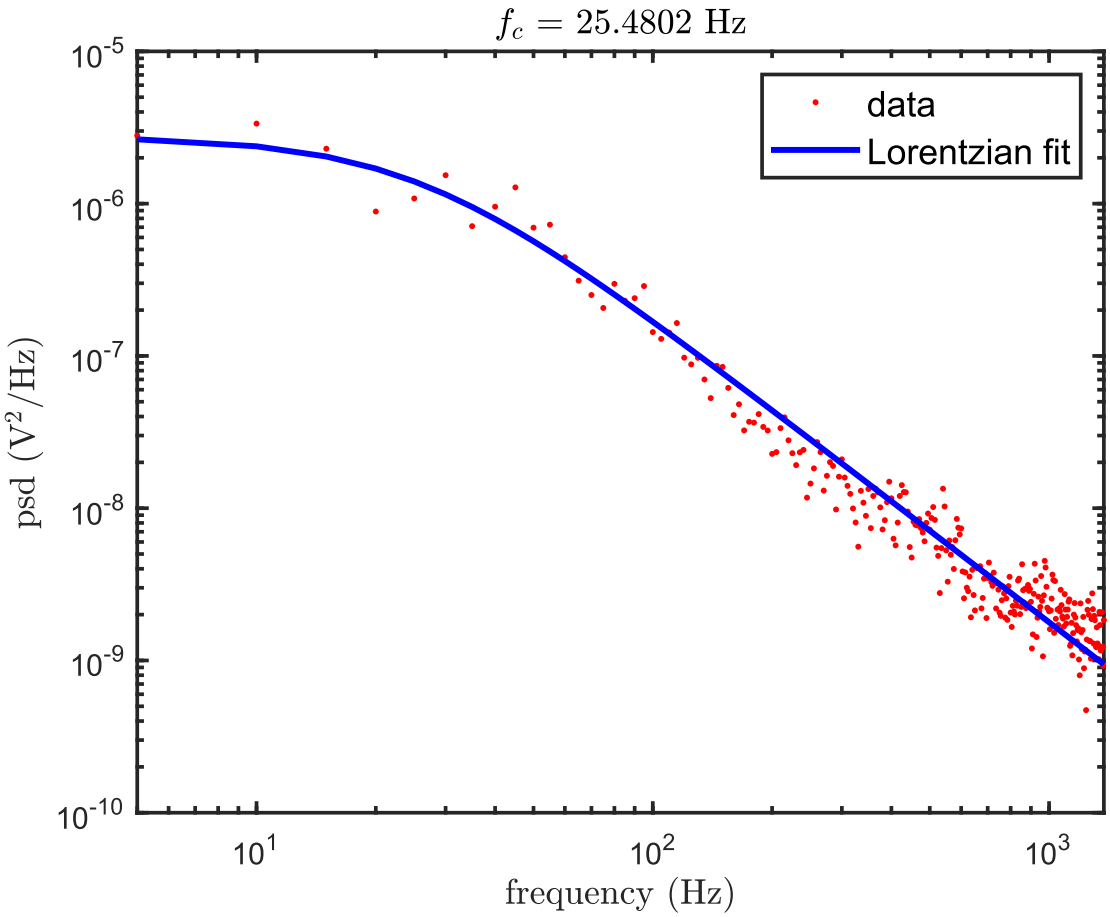

Figure 7.3: Power spectral density plot of trapping signal from DNH showing Lorentzian characteristic typical of weak optical traps.

In molecular dynamics simulations, the deformations of PR65 have been predicted to be related to the amino acid configuration and substitution mutations resulted in changes to the

location of and energy barrier towards unstacking [103]. In addition, experimental works on ensembles have shown sensitivity of denaturalization on point mutations [228]. To probe the impact of point mutations on single proteins in experiment, we perform additional trapping experiments with six PR65 mutants: Y168V, F502W, E375D, D315E, S323L and L198V. To compare behavior between PR65 wild type (WT) and mutants, the length of intermediate steps were extracted from data. Figure 7.4a below shows the intermediate step length between the start of trapping (dip in transmission) to the final trapped state for PR65 WT and mutant trapping events (between 4 to 7 events for each mutant), with the median value shown in black. For events with quasi-stable final states, the shortest time to highest transmission state was selected. While the distribution of intermediate step lengths is broad for all mutants, median values vary by an order of magnitude from 50 ms (S323L) to 0.8 s (E375D). This shows clearly that the process causing a multi-step trapping signal is strongly impacted by mutations to PR65.

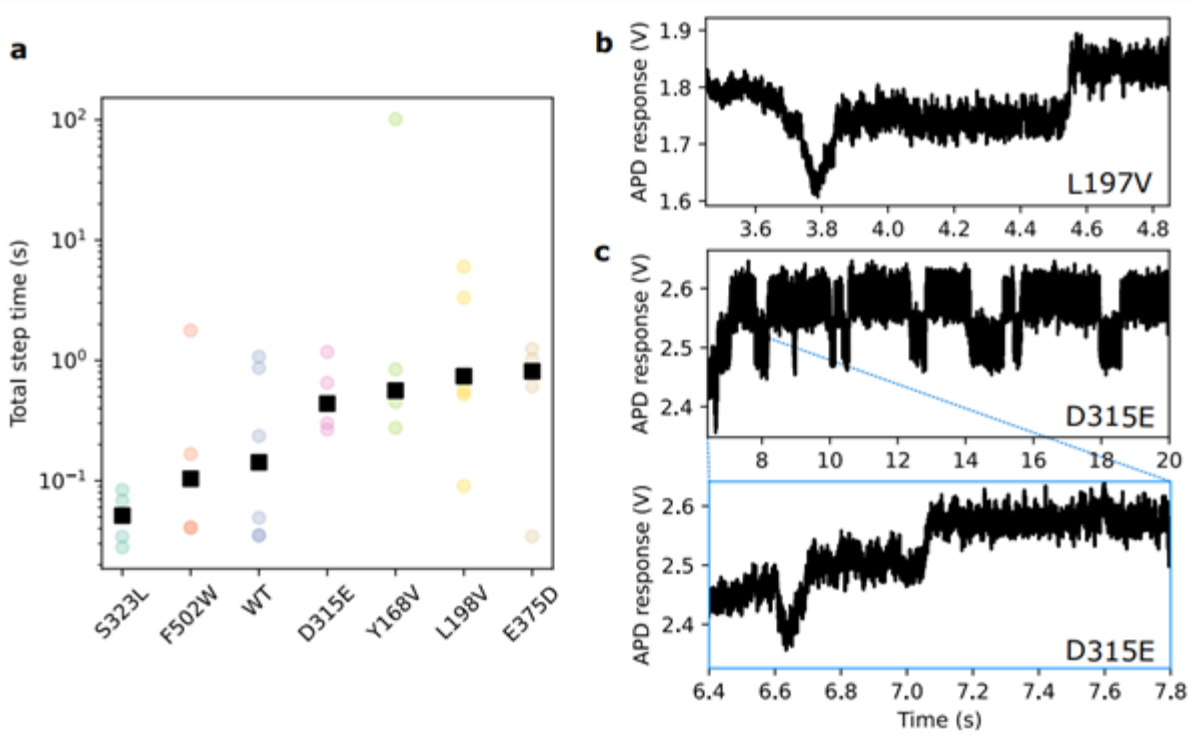

Figure 7.4: PR65 WT and mutants. a. Intermediate step times (colored circles) and mean values (black squares) for PR65 WT and mutants versus relative stability. b. Trapping event of mutant L197V, scaled to show long intermediate step. c. Trapping event of mutant D315E, scaled to show telegraphing behavior (upper) and scale zoomed to show intermediate step (lower).

These results support the intermediate steps observed (Figure 7.4b above, for example) during optical trapping of PR65 being attributed to an unstacking deformation of the structure that can be delayed in onset by increasing the stability of the protein towards unfolding. Unstacking was predicted to occur at multiple sites, each with a different energy [103], [228], a feature which is likely linked to PR65's ability to bind subunit C and multiple isoforms of subunit B [229].

Some of the trapped proteins (D315E and S323L) displayed a telegraphing behavior, shown here in Figure 7.4c above. This behavior is indicative that the protein is quasi-stable between two

different conformations, showing that the electrostriction force from the DNH optical tweezer is sufficiently low that it is perturbative but does not govern the observed dynamics.

7.5 Summary and Conclusion

In summary, we have observed a spontaneous change in the trapping signal of PR65 (WT and 6 mutants) when trapped in a DNH optical tweezer, which we interpret as changes in the polarizability coming from unstacking under thermal fluctuations, with some contribution also from electrostriction. Many orders of magnitude faster unstacking had been predicted *in silico* with much higher pulling forces than we expect to be present in our setup. We see a general trend that point mutations can strongly influence the energetics of unstacking. This approach shows potential to investigate the connection between mechanical properties and catalytic activity, as well as application to curing cancers and neurological diseases by modulating this activity. For example, the L197V mutation we investigated has been shown to prevent a small molecule activation of anti-tumor activity in a previous study [128] (it was labelled L198V in that work), and so it is interesting to note that it confers significantly greater mechanical stability in our experiments. However, the source of the broadness of the distribution of intermediate step lengths seen in these measurements needs to be further investigated to reveal whether it is a feature of the protein itself or caused by a feature of the experiment.

Chapter 8

Conclusion

The purpose of the current research was to investigate the effect of point (substitution) mutations on the conformation changes of PR65 using DNH aperture tweezers.

The study was anchored on answering the following questions:

(a) How does a dielectric nanoparticle interact with a nanoaperture, and could this be exploited to study protein conformation changes using aperture tweezers such as the DNH aperture tweezer?

(b) What can be said of the behavior of PR65 when trapped in a DNH aperture tweezer, and can this be explained in terms of how PR65 interacts with the DNH aperture?

(c) What is the impact of point mutations on the conformational dynamics of PR65 trapped in a DNH aperture tweezer?

The interaction between a nanoaperture and a dielectric nanoparticle was modelled in terms of a simple dipole-dipole interaction based on the Rayleigh scattering and Bethe aperture theorems. The model showed that the interaction enhanced both the trapping potential and the transmission through the aperture in accordance with the SIBA effect, in which a nanoparticle interacting with a focused laser beam aided its own trapping. The model also showed that the transmission was characteristic of the particle's polarizability through the modification of the field of the aperture by the dielectric particle. This suggested that nanoaperture tweezer signals might be used to probe particle changes that altered the polarizability of a particle. In particular, it was hypothesized that if conformation changes induced by substitution mutations alter the material

polarizability of PR65, then the DNH optical tweezer signal acquired by trapping each mutant PR65 will have a different RMSD and corner frequency from that of wild type PR65.

To test the stated hypothesis, PR65 wild type and six of its mutants were trapped in a DNH aperture tweezer at a laser power of ~ 22 mW, and the resulting optical signals captured using an APD connected to a digital USB-4771A data acquisition module were analyzed using MATLAB. Parameters extracted from the acquired signals and studied included the median transition time between the characteristic jump states shown by the acquired signals and the RMSD and corner frequency of the acquired signals. Comparison of these parameters for the mutants with those for wild type PR65 showed that some mutations conferred more stability on PR65 while other mutations had a destabilizing effect on PR65. Correlation of these parameters with *in silico* mean contour lengths of PR65 wild type and six of its mutants studied was also consistent with this conclusion, in line with the hypothesis.

Based on the foregoing results, it can be concluded that under mechanical forces such as would be present in an optical tweezer, PR65 undergoes conformation changes that are impacted by substitution mutations, which can be probed using nanoaperture tweezers such as the DNH aperture tweezer since the transmission through the aperture of the DNH aperture tweezer depends on the material polarizability of PR65 which, in turn, depends on the conformation of PR65. This might have potential for the detection of mutant proteins and for tracking protein mutations and conformational dynamics. Additionally, the technique might be extended to study the binding of ligands to proteins, with implications for drug discovery and testing.

Bibliography

[1] S. Mathew and R. Gordon, "Self-induced back-action for aperture trapping: Bethe-Rayleigh theory," *Opt. Express,* vol. 31, no. 26, pp. 44190 - 44198, 2023.

[2] H. A. Atwater, "The Promise of Plasmonics," *Scientific American,* vol. 17, no. 3, pp. 56 - 63 , 2007.

[3] H. Raether, Surface Plasmons on Smooth and Rough Surfaces and on Gratings, Berlin: Springer-Verlag, 1988.

[4] S. A. Maier, M. L. Brongersma, P. G. Kik, S. Meltzer, A. A. G. Requicha and H. A. Atwater, "Plasmonics - A Route to Nanoscale Optical Devices," *Advanced Materials,* vol. 13, no. 19, pp. 1501 - 1505, 2001.

[5] M. L. Brongersma, "Introductory lecture: nanoplasmonics," *Faraday Discussions. DOI: 10.1039/c5fd90020d,* 2015.

[6] R. Gordon, "Nanostructured metals for light-based technologies," *Nanotechnology,* vol. 30, no. 212001, pp. 1 - 20, 2019.

[7] N. J. Hales, "Plasmonics sheds light on the nanotechnology of daguerreotypes," *PNAS,* vol. 116, no. 28, pp. 13724 - 13726, 2019.

[8] W.-C. Liu and D. P. Tsai, "Optical tunneling effect of surface plasmon polaritons and localized surface plasmon resonance," *Physical Review B,* vol. 65, no. 155423, pp. 1 - 5, 2002.

[9] R. Gordon, "Surface plasmon nanophotonics: a tutorial," *IEEE Nanotechnology Magazine,* vol. 2, no. 3, pp. 12 - 18, 2008.

[10] E. Babaei, Z. Sharifi and R. Gordon, "Improving sensitivity of existing surface plasmon resonance systems with grating-coupled short-range surface plasmons," *J. Opt. Soc. Am. B,* vol. 36, no. 8, pp. 144 - 148, 2019.

[11] F. Wang and R. Y. Shen, "General Properties of Local Plasmons in Metal Nanostructures," *Physical Review Letters,* vol. 97, no. 20, pp. 1 - 4, 2006.

[12] R. H. Ritchie, "Plasma Losses by Fast Electrons in Thin Films," *Physical Review,* vol. 106, no. 5, pp. 874 - 881, 1957.

[13] C. J. Powell and J. B. Swan, "Origin of the Characteristic Electron Energy Losses in Aluminum," *Physical Review,* vol. 115, no. 4, pp. 869 - 875, 1959.

[14] C. J. Powell and J. B. Swan, "Origin of the Characteristic Electron Energy Losses in Magnessium," *Physical Review,* vol. 116, no. 1, pp. 81 - 83, 1959.

[15] K. L. Corum and J. F. Corum, "Nikola Tesla, Lightning Observations, And Stationary Waves," in *Proccedings of the 1994 International Tesla Symposium*, Colarado, 1994.

[16] R. Warnock, "On the Propagation of Electromagnetic Waves along a Wire by A. Sommerfield," *Electromagnetics,* vol. 39, no. 5, pp. 281-324, 2019.

[17] D. Wang, N. B. Saleh, A. Byro, R. Zepp, E. Sahle-Demessie, T. P. Luxton, K. T. Ho, B. R. M, M. Flury, J. C. White and C. Su, "Nano-enabled pesticides for sustainable agriculture and global food security," *Nat. Nanotechnol.,* vol. 17, no. 4, pp. 347-360, 2022.

[18] T. Vo-Dinh and B. A. Inman, "What potential does plasmonics-amplified synergistic immuno photothermal nanotherapy have for treatment of cancer," *Nanomedicine,* vol. 13, no. 2, pp. 139 - 144, 2017.

[19] C. Loo, A. Lin, L. Hirsch, M.-H. Lee, J. Barton, N. Hales and J. D. R. West, "Nanoshell-Enabled Photonics-Based Imaging and Therapy of Cancer," *Technol Cancer Res Treat,* vol. 3, no. 1, pp. 33 - 40, 2004.

[20] S. Ambardar, D. Nguyen, G. Binder, Z. W. Withers and D. V. Voronine, "Quantum Leap from Gold and Silver to Aluminium Nanoplasmonics for Enhanced Biomedical Applications," *Applied Sciences,* vol. 10, no. 4210, pp. 3 - 28, 2020.

[21] J. Singh, S. Sekhon and S. Verma, "Plasmonics: the future wave of communication," *Current Science,* vol. 101, no. 4, pp. 484 - 488, 2011.

[22] M. Cohen, Y. Abulafia, D. Lev, A. Lewis, R. Shavit and Z. Zalevsky, "Wireless Communication with Nanoplasmonic Data Carriers: Macroscale Propagation of Nanophotonic Plasmon Polaritons Probed by Near-Field Nanoimaging," *Nano Lett,* vol. 17, no. 9, p. 5181–5186, 2017.

[23] W. O. F. Carvalho and R. J. Mejía-Salazar, "Plasmonics for Telecommunications Applications," *Sensors,* vol. 20, no. 9, pp. 1 - 21, 2020.

[24] G. Baffou and R. Quidant, "Thermo-plasmonics: using metallic nanostructures as nano-sources of heat," *Laser Photonics Rev,* vol. 7, no. 2, pp. 171 - 187, 2013.

[25] B. Liedberg, C. Nylander and I. Lundström, "Biosensing with surface plasmon resonance — how it all started," *Biosensor and Bioelectronics,* vol. 10, no. 8, pp. 1 - 9, 1995.

[26] X. Han, K. Liu and C. Sun, "Plasmonics for Biosensing," *Materials,* vol. 12, no. 1411, pp. 1 - 24, 2019.

[27] W. Ye, R. Long, H. Huang and Y. Xiong, "Plasmonic nanostructures in solar energy conversion," *J. Mater. Chem. C,* vol. 5, pp. 1008 - 1021, 2017.

[28] P. V. Kamat and G. V. Hartland, "Plasmons for Energy Conversion," *ACS Energy Lett.*, vol. 3, no. 6, p. 1467–1469, 2018.

[29] M. S. Shariatdoust, A. L. Frencken, A. Khademi, A. Alizadehkhaledi, F. C. J. M. van Veggel and R. Gordon, "Harvesting Dual-Wavelength Excitation with Plasmon-Enhanced," *ACS Photonics,* vol. 5, pp. 3507 - 3512, 2018.

[30] Y. B. Zheng, B. Kiraly, P. S. Weiss and T. J. Huang, "Molecular plasmonics for biology and nanomedicine," *Nanomedicine (Lond),* vol. 7, no. 5, pp. 751 - 770, 2012.

[31] D. E. Kretschmann, "The determination of the optical constants of metals by excitation of surface plasmons," *Z. Physik*, vol. 241, pp. 313 - 324, 1971.

[32] Y. Pang and R. Gordon, "Optical Trapping of a Single Protein," *Nano Lett.*, vol. 12, no. 1, pp. 402 - 406, 2012.

[33] A. Kotnala and R. Gordon, "Double nanohole optical tweezers visualize protein p53 suppressing unzipping of single DNA-hairpins," *Biomed. Opt. Express,* vol. 5, pp. 1886 - 1894, 2014.

[34] S. Jones, A. A. Al Balushi, Gordon and Reuven, "Raman spectroscopy of single nanoparticles in a double-nanohole optical tweezer system," *Journal of Optics,* vol. 17, pp. 1 - 6, 2015.

[35] K. Svoboda and S. M. Block, "Biological Applications of Optical Forces," *Annu. Rev. Biophys. Biomol. Struct.*, vol. 23, pp. 247 - 285, 1994.

[36] D. J. Griffiths, Introduction to Electrodynamics, 3rd Ed., p. 443 - 447, New Jersey: Prentice-Hall Inc., 1999.

[37] D. J. Jackson, Classical Electrodynamics, 3rd Ed., p. 407 - 412, New Jersey: John Wiley & Sons, Inc., 1999.

[38] S. A. Maier, Plasmonics: Fundamentals and Applications, New York: Springer, 2007.

[39] T. W. Ebbesen, H. J. Lezec, H. F. Ghaemi and T. Thio, "Extraordinary optical transmission through sub-wavelength hole arrays," *Nature*, vol. 391, pp. 667 - 669, 1998.

[40] H. F. Ghaemi, T. Thio, D. E. D. E. Grupp, T. W. Ebbesen and H. J. Lezec, "Surface plasmons enhance optical transmission through subwavelength holes," *Physical Review B,* vol. 58, no. 11, pp. 6779 - 6782, 1998.

[41] A. Ashkin, " Acceleration and trapping of particles by radiation pressure," *Phys. Rev. Lett.*, vol. 24, no. 4, pp. 156 - 159, 1970.

[42] A. Ashkin, J. M. Dziedzic, J. E. Bjorkholm and S. Chu, "Observation of a single-beam gradient force optical trap for dielectric particles," *Optics Letters*, vol. 11, no. 5, pp. 288 - 290, 1986.

[43] A. Ashkin, "History of optical trapping and manipulation of small-neutral particle, atoms, and molecules," *IEEE Journal of Selected Topics in Quantum Electronics*, vol. 6, no. 6, pp. 841 - 856, 2000.

[44] D. G. Grier, "A Revolution in Optical Manipulation," *Nature*, vol. 424, pp. 810 - 816, 2003.

[45] K. C. Neuman and B. M. Steven, "Optical trapping," *The Review of scientific instruments*, vol. 75, no. 9, pp. 787 - 809, 2004.

[46] A. Ashkin, "Optical trapping and manipulation of neutral particles using lasers," *Proc. Natl. Acad. Sci.*, vol. 94, no. 10, pp. 4853 - 4860, 1997.

[47] S. E. S. Spesyvtseva and K. Dholakia, "Trapping in a Material World," *ACS Photonics,* vol. 3, pp. 719 - 736, 2016.

[48] T. D. Bouloumis and S. N. Chormaic, "From Far-Field to Near-Field Micro- and Nanoparticle Optical Trapping," *Applied Sciences,* vol. 10, no. 1375, pp. 1 - 18, 2020.

[49] J. M. A. Gajraj, "Optical Tweezers," in *Encyclopedia of Modern Optics*, Amsterdam, Elsevier, 2005, pp. 78 - 86.

[50] T. Nieminen, N. Heckenberg and H. Rubinsztein-Dunlop, "Forces in optical tweezers with radially and azimuthally polarized trapping beams," *Opt. Lett.,* vol. 33, no. 2, pp. 122 - 124, 2008.

[51] A. Mazolli, P. A. Maia Neto and H. M. Nussenzveig, "Theory of trapping forces in optical tweezers," *Proc. R. Soc. Lond. A.,* vol. 459, no. 2040, pp. 3021 - 3041, 2003.

[52] F. Kalantarifard, P. Elahi, G. Makey, O. M. Maragò, Ö. F. Ilday and G. Volpe, "Intracavity optical trapping of microscopic particles in a ring-cavity fiber laser," *Nature Communications,* vol. 10, no. 1, pp. 1 - 11, 2019.

[53] G. Pesce, P. H. Jones, O. M. Maragò and G. Volpe, "Optical tweezers: theory and practice," *Eur. Phys. J. Plus,* vol. 135, no. 949, pp. 948 - 985, 2020.

[54] H. J, M. J, V. G and M. K, "Non-spherical particles in optical tweezers: A numerical solution," *PLoS ONE,* vol. 14, no. 12, pp. 1 - 21, 2019.

[55] P. Polimeno, A. Magazzù, M. A. Iatì, F. Patti, R. Saija, C. D. E. Boschi, M. G. Donato, P. G. Gucciardi, P. H. Jones, G. Volpe and O. M. Maragò, "Optical tweezers and their applications," *Journal of Quantitative Spectroscopy and Radiative Transfer,* vol. 218, pp. 131 - 150, 2018.

[56] E. Almaas and I. Brevik, "Radiation forces on a micrometer-sized sphere in an evanescent field," *J. Opt. Soc. Am. B,* vol. 12, no. 12, pp. 2429 - 2438 , 1995.

[57] J. P. Barton, D. R. Alexander and S. A. Schaub, "Internal and near-surface electromagnetic fields for a spherical particle irradiated by a focused laser beam," *J. Appl. Phys.,* vol. 64, no. 4, pp. 1632 - 1639 , 1988.

[58] P. Zemánek, A. Jonáš and M. Miroslav Liška, "Simplified description of optical forces acting on a nanoparticle in the Gaussian standing wave," *J. Opt. Soc. Am. A,* vol. 19, no. 5, pp. 1025 - 1034 , 2002.

[59] K. F. Ren, G. Gréha and G. Gouesbet, "Radiation pressure forces exerted on a particle arbitrarily located in a Gaussian beam by using the generalized Lorenz-Mie theory, and associated resonance effects," *Opt. Commun.,* vol. 108, no. (4 - 6), pp. 343 - 354 , 1994.

[60] H. C. van de Hulst, Light Scattering by Small Particles, New York: Dover Publications, Inc., 1981.

[61] J. Bechhoefer and S. Wilson, "Faster, cheaper, safer optical tweezers for the undergraduate laboratory," *American Journal of Physics,* vol. 70, no. 4, pp. 392 - 400, 2002.

[62] J. A. Käs, "Introduction - Optical Traps," Soft Matter Physics Division, University of Leipzig, 28 February 2003. [Online]. Available: https://home.uni-leipzig.de/pwm/web/?page=opticaltraps&section=introduction. [Accessed 27 March 2022].

[63] A. Ashkin and J. M. Dziedzic, "Optical Trapping and Manipulation of Viruses and Bacteria," *Science,* vol. 235, no. 4795, pp. 1517 - 1520, 1987.

[64] E. Gregersen, "Arthur Ashkin," Encyclopedia Britannica, 17 September 2021. [Online]. Available: https://www.britannica.com/biography/Arthur-Ashkin. [Accessed 27 March 2022].

[65] M. L. Juan, R. Gordon, Y. Pang, F. Eftekhari and R. Quidant, "Self-induced back-action optical trapping of dielectric nanoparticles," *Nature Physics,* vol. 5, pp. 915 - 919 , 2009.

[66] T. J. Davis, "Brownian Diffusion of Nano-particles in Optical Traps," *Optics Express,* vol. 15, no. 5, pp. 2702 - 2712, 2007.

[67] Y. Liu, G. J. Sonek, M. W. Berns and B. J. Tromberg, "Physiological Monitoring of Optically Trapped Cells: Assessing the Effects of Confinement by 1064-nm Laser Tweezers Using Microfluorometry," *Biophysical Journal,* vol. 71, no. 4, pp. 2158 - 2167 , 1996.

[68] Y. Chen, A. Kotnala, L. Yu, J. Zhang and R. Gordon, "Wedge and gap plasmonic resonances in double nanoholes," *Optics Express,* vol. 23, no. 23, pp. 30227 - 30236, 2015.

[69] P. B. Catrysse and S. F. Shin, "Propagating modes in subwavelength cylindrical holes," *J. Vac. Sci. Technol. B,* vol. 23, no. 6, pp. 2675 - 2678 , 2005.

[70] J. B. Pendry, L. Martin-Moreno and F. J. Garcia-Vidal, "Mimicking Surface Plasmons with Structured Surfaces," *Science,* vol. 305, no. 5685, pp. 847 - 848, 2004.

[71] E. C. Kinzel and X. Xu, "Extraordinary infrared transmission through a periodic bowtie aperture array," *Optics Letters,* vol. 35, no. 7, pp. 992 - 994 , 2009.

[72] J. R. DiMaio and J. Ballato, "Polarization-dependent transmission through subwavelength anisotropic aperture arrays," *Opt. Express,* vol. 14, no. 6, pp. 2380 - 2384 , 2006.

[73] H. J. Lezec and T. Thio, "Diffracted evanescent wave model for enhanced and suppressed optical transmission through subwavelength hole arrays," *Optics Express,* vol. 12, no. 16, pp. 3629 - 3651 , 2004.

[74] Y. Zhang, C. Min, X. Dou, X. Wang, H. P. Urbach, M. G. Somekh and X. Yuan, "Plasmonic tweezers: for nanoscale optical trapping and beyond," *Light: Science & Applications,* vol. 10, no. 59, pp. 1 - 41 , 2021.

[75] L. Numeier, R. Quidant and D. E. Chang, "Self-induced back-action optical trapping in nanophotonic systems," *New J. Physics,* vol. 17, no. 12, pp. 1 - 15, 2015.

[76] T. Zhu, Y. Cao, L. Wang, Z. Nie, T. Cao, F. Sun, Z. Jiang, M. Nieto-Vesperinas, Y. Liu, C.-W. Qiu and W. Ding, "Self-Induced Backaction Optical Pulling Force," *Physical Review Letters,* vol. 120, no. 12, pp. 1 - 6, 2018.

[77] N. Descharmes, U. P. Dharanipathy, Z. Diao, M. Tonin and R. Houdre´, "Observation of Backaction and Self-Induced Trapping in a Planar Hollow Photonic Crystal Cavity," *Physical Review Letters,* vol. 110, no. 12, pp. 1 - 4, 2013.

[78] V. Giannini, A. I. Fernández-Domínguez, S. C. Heck and S. A. Maier, "Plasmonic Nanoantennas: Fundamentals and Their Use in Controlling the Radiative Properties of Nanoemitters," *Chemical Reviews,* vol. 111, no. 6, pp. 3888 - 3912 , 2011.

[79] P. Biagioni, J.-S. Huang and B. Hecht, "Nanoantennas for visible and infrared radiation," *Rep. Prog. Phys.*, vol. 75, no. 2, pp. 1 - 41, 2012.

[80] D. G. Kostsifaki and S. N. Chormaic, "Plasmonic optical tweezers based on nanostructures: fundamentals, advances and prospects," *Nanophotonics,* vol. 8, no. 7, pp. 1227 - 1245 , 2019.

[81] K. Okamoto and S. Kawata, "Radiation Force Exerted on Subwavelength Particles near a Nanoaperture," *Physical Review Letters,* vol. 83, no. 22, pp. 4534 - 4537, 1999.

[82] M. Nieto-Vesperinas, P. C. Chaumet and A. Rahmani, "Near-Field Photonic Forces," *Philosophical Transactions: Mathematical, Physical and Engineering Sciences,* vol. 362, no. 1817, pp. 719 - 737 , 2004.

[83] E.-S. Kwak, T.-D. Onuta, D. Amarie, R. Potyrailo, B. Stein, S. C. Jacobson, W. L. Schaich and B. Dragnea, "Optical Trapping with Integrated Near-Field Apertures," *J. Phys. Chem. B,* vol. 108, no. 36, pp. 13607 - 13612 , 2004.

[84] K. Sloyan, H. Melkonyan, H. Apostoleris, M. S. Dahlem, M. Chiesa and A. Al Ghaferi, "A review of focused ion beam applications in optical fibers," *Nanotechnology,* vol. 32, no. 47, pp. 1 - 27, 2021.

[85] A. Lesuffleur, L. Kumar, S. Kiran, A. G. Brolo, K. L. Kavanagh and R. Gordon, "Apex-Enhanced Raman Spectroscopy Using Double-Hole Arrays in a Gold Film," *Journal of Physical Chemistry C,* vol. 111, pp. 2347 - 2350, 2007.

[86] S. Iyer, S. Popov and A. T. Friberg, "Impact of apexes on the resonance shift in double hole nanocavities," *Optics Express,* vol. 18, no. 1, pp. 193 - 203 , 2009.

[87] L. Kumar, S. Kiran and R. Gordon, "Overlapping Double-Hole Nanostructure in a Metal Film for Localized Field Enhancement," *IEEE Journal of Selected Topics in Quantum Electronics,* vol. 12, no. 6, pp. 1228-1232, 2006.

[88] P. Biagioni, J.-S. Huang and B. Hecht, "Nanoantennas for visible and infrared radiation," *Rep. Prog. Phys.,* vol. 75, pp. 1 - 41, 2012.

[89] J. Zhou and G. Yang, "Focused Ion-Beam Based Nanohole Modeling, Simulation, Fabrication, and Application," *ASME. J. Manuf. Sci. Eng.,* vol. 132, no. 1, pp. 1 - 8, 2010.

[90] A. Kotnala and R. Gordon, "Quantification of High-Efficiency Trapping of Nanoparticles in a Double Nanohole Optical Tweezer," *Nano Lett.,* vol. 14, no. 2, pp. 853 - 856 , 2014.

[91] M. Najiminaini, F. Vasefi, B. Kaminska and J. J. L. Carson, "Optical resonance transmission properties of nano-hole arrays in a gold film: effect of adhesion layer," *Optics Express,* vol. 19, no. 27, pp. 26186 - 26197 , 2011.

[92] S. H. Baek, S. Lee, J.-H. Bae, C.-W. Hong, M.-J. Park, H. Park, M.-C. Baek and S.-W. Nam, "Nanopillar and nanohole fabrication via mixed lithography," *Materials Research Express,* vol. 7, no. 3, p. 035008, 2020.

[93] J. Bergeron, A. Zehtabi-Oskuie, S. Ghaffari, Y. Pang and R. Gordon, "Optical Trapping of Nanoparticles," *J. Vis. Exp.,* vol. 71, p. e4424, 2013.

[94] A. Zehtabi-Oskuie, A. A. Zinck, R. M. Gelfand and R. Gordon, "Template stripped double nanohole in a gold film for nano-optical tweezers," *Nanotechnology,* vol. 25, no. 9, p. 495301, 2014.

[95] P. Nagpal, N. C. Lindquist, S.-H. Oh and D. J. Noris, "Ultrasmooth patterned metals for plasmonics and metamaterials," *Science,* vol. 325, no. 5940, pp. 594 - 597 , 2009.

[96] A. R. Lalitha, M. S. Shariatdoust, S. Mathew and R. Gordon, "Colloidal lithography double-nanohole optical trapping of nanoparticles and proteins," *Optics Express,* vol. 27, no. 11, pp. 16184 - 16194, 2019.

[97] J.-F. Masson, M.-P. Murray-Méthot and L. S. Live, "Nanohole arrays in chemical analysis: manufacturing methods and applications," *Analyst,* vol. 135, no. 7, pp. 1483 - 1489 , 2010.

[98] J. C. Hulteen and R. P. Van Duyne, "Nanosphere lithography: A materials general fabrication process for periodic particle array surfaces," *Journal of Vacuum Science & Technology A,* vol. 13, no. 3, pp. 1553 - 1558 , 1995.

[99] S. H. Lee, K. C. Bantz, N. C. Lindquist, S.-H. Oh and C. L. Haynes, "Self-Assembled Plasmonic Nanohole Arrays," *Langmuir,* vol. 25, no. 23, pp. 13685 - 13693 , 2009.

[100] A. Pravitasari, M. Negrito, K. Light, W.-S. Chang, S. Link, M. Sheldon and J. D. Batteas, "Using Particle Lithography to Tailor the Architecture of Au Nanoparticle Plasmonic Nanoring Arrays," *J. Phys. Chem. B,* vol. 122, no. 2, pp. 730 - 736 , 2018.

[101] A. Gajraj and J. C. Meiners, "Optical Tweezers," in *Encyclopedia of Modern Optics (Guenther, R. D., Ed.),* Amsterdam, Elsevier, 2005, pp. 78 - 86 .

[102] M. C. Williams, "Optical Tweezers: Measuring Piconewton Forces," 23 March 2002. [Online]. Available: https://www.semanticscholar.org/paper/Optical-Tweezers-:-Measuring-Piconewton-Forces-Williams/8f039df534bb8243862917aefa54acc532e09baa. [Accessed 31 March 2022].

[103] A. Grinthal, I. Adamovic, B. Weiner, M. Karplus and N. Kleckner, "PR65, the HEAT-repeat scaffold of phosphatase PP2A, is an elastic connector that links force and catalysis," *Biophysics and Computational Biology,* vol. 107, no. 6, pp. 2467 - 2472 , 2010.

[104] I. Kolokolnikov, E. Neopomnyashchaya and E. Velichko, "Static light scattering for determination of physical parameters of macro- and nanoparticles," in *6th International School and Conference "Saint Petersburg OPEN 2019": Optoelectronics, Photonics, Engineering and Nanostructures*, Saint Petersburg, Russian Federation, 2019.

[105] R. Xu, "Light scattering: A review of particle characterization applications," *Particuology,* vol. 18, pp. 11 - 21 , 2015.

[106] S. Santucci and V. Esposito, "Electrostrictive Ceramics and Their Applications," in *Encyclopedia of Materials: Technical Ceramics and Glasses (Paleroy, M., Ed.),* Amsterdam, Elsevier, 2021, pp. 369 - 374 .

[107] X. Zhao and Z. Suo, "Electrostriction in elastic dielectrics undergoing large deformation," *Journal of Applied Physics,* vol. 104, no. 12, pp. 123530-1 - 123530-7, 2008.

[108] R. Gordon, "Biosensing with nanoaperture optical tweezers," *Optics & Laser Technology,* vol. 109, no. 5, pp. 328 - 335 , 2019.

[109] N. Banaz, J. Mäkelä and S. Uphoff, "Choosing the right label for single-molecule tracking in live bacteria: side-by-side comparison of photoactivatable fluorescent protein and Halo tag dyes," *J. Phys. D: Appl. Phys.,* vol. 52, no. 6, p. 064002, 2019.

[110] C. Bustamante, Y. R. Chemla, S. Liu and M. D. Wang, "Optical tweezers in single-molecule biophysics," *Nat Rev Methods Primers,* vol. 1, no. 25, pp. 1 - 29 , 2021.

[111] Y. Kimura and P. R. Bianco, "Single molecule studies of DNA binding proteins using optical tweezers," *Analyst,* vol. 131, no. 8, pp. 868 - 874 , 2006.

[112] K. Svoboda, C. F. Schmidt, B. J. Schnapp and S. M. Block, "Direct observation of kinesin stepping by optical trappig interferometry," *Nature,* vol. 365, no. 6448, pp. 721 - 727 , 1993.

[113] J. T. Finer, R. M. Simmons and J. A. Spudich, "Single myosin molecule mechanics: piconewton forces and nanometre steps," *Nature,* vol. 368, no. 6467, pp. 113 - 119 , 1994.

[114] K. C. Neuman, Abbondanzieri, R. Landick, J. Gelles and S. M. Block, "Ubequitous Transcription Pausing Is Independent of RNA Polymerase Backtracking," *Cell,* vol. 115, no. 4, pp. 437 - 447 , 2003.

[115] Y. Pang and R. Gordon, "Optical Trapping of Single Protein," *Nano Lett.,* vol. 12, no. 1, pp. 402 - 406, 2012.

[116] R. Gordon, "Future Prospects for Biomolecular Trapping with Nanostructured Metals," *ACS Photonics,* pp. A - I, 2022.

[117] S. Wheaton, R. M. Gelfand and R. Gordon, "Probing the Raman-active acoustic vibrations of nanoparticles with extraordinary spectral resolution," *Nature Photonics,* vol. 9, no. 1, pp. 68 - 72 , 2015.

[118] P. Senet, "Protein Conformational Dynamics: from Normal Mode Analysis to Free-energy Landscape Perspective, YouTube," 17 June. [Video file]. 2021. [Online]. Available: https://youtube.be/aNjQmdKJE_c. [Accessed 13 April 2022].

[119] S. Wheaton and R. Gordon, "Single Molecule Protein Sizing in Double Nano-hole Optical Tweezers," in *Optics in the Life Sciences*, 2015.

[120] N. Hacohen, C. J. X. Candice J. X. Ip and R. Gordon, "Analysis of Egg White Protein Composition with Double Nanohole Optical Tweezers," *ACS Omega,* vol. 3, no. 5, pp. 5266 - 5272 , 2018.

[121] S. Schmid, P. Stömmer, H. Dietz and C. Dekker, "Nanopore electro-osmotic trap for the label-free study of single proteins and their conformations," *Nature Nanotechnology,* vol. 16, no. 11, pp. 1244 - 1250 , 2021.

[122] G. Young, N. Hundt, D. Cole, F. Adam, J. Andrecka, A. Tyler, A. Olerinyova, A. Ansari, E. G. Marklund, M. P. Collier, S. A. Chandler, O. Tkachenko, J. Allen, M. Crispin and N. Billington, "Quantitative mass imaging of single biological macromolecules," *Science.*, vol. 360, no. 6387, pp. 423 - 427 , 2018.

[123] M. Piliarik and V. Sandoghdar, "Direct optical sensing of single unlabelled proteins and super-resolution imaging of their binding sites," *Nature communications,* vol. 5, no. 4495, pp. 1 - 8 , 2014.

[124] H. S. Chung, K. McHale, J. M. Louis and W. A. Eaton, "Single-Molecule Fluorescence Experiments Determine Protein Folding Transition Path Times," *Science,* vol. 335, no. 6071, pp. 981 - 984 , 2012.

[125] D. V. Verschueren, S. Pud, X. Shi, L. De Angelis, L. Kuipers and C. Dekker, "Label-Free Optical Detection of DNA Translocations through Plasmonic Nanopores," *ACS Nano,* vol. 13, no. 1, pp. 61 - 70 , 2019.

[126] S. Peri, S. Santosh, M. K. Sabnani, M. U. Raza, S. Ghaffari, S. Gimlin, D. D. Wawro, J. S. Lee, M. J. Kim, J. Weidanz and G. Alexandrakis, "Detection of specific antibody-ligand interactions with a self-induced back-action actuated nanopore electrophoresis sensor," *Nanotechnology,* vol. 31, no. 8, pp. 1 - 12 , 2020.

[127] A. A. Al Balushi, A. Zehtabi-Oskuie and R. Gordon, "Observing single protein binding by optical transmission through a double nanohole aperture in a metal film," *Biomed Opt Express,* vol. 4, no. 9, pp. 1504 - 1511 , 2013.

[128] J. Sangodkar, A. Perl, R. Tohme, J. Kiselar, D. B. Kastrinsky, N. Zaware, S. Izadmehr, S. Mazhar, D. D. Wiredja, C. M. O'Connor, D. Hoon, N. S. Dhawan and M. Ohlmeyer, "Activation of tumor suppressor protein PP2A inhibits KRAS-driven tumor growth," *J Clin Invest.,* vol. 127, no. 6, pp. 2081 - 2090 , 2017.

[129] G. Calin, M. Iasio, E. Caprini, I. Vorechovsky, P. Natali, G. Sozzi, C. Croce, G. Barbanti-Brodano, G. Russo and M. Negrin, "Low frequency of alterations of the (ppp2r1a) and (ppp2r1b) isoforms of the subunit a of the serine-threonine phosphatase 2a in human neoplasms," *Oncogene,* vol. 19, pp. 1191 - 1195 , 2000.

[130] M. R. Groves, N. Hanlon, P. Turowski, B. A. Hemmings and D. Barford, "The structure of the protein phosphatase 2a pr65/a subunit reveals the conformation of its 15 tandemly repeated heat motifs," *Cell,* vol. 96, pp. 99 - 110 , 1999.

[131] T. Torrent and I. Ferrer, "PP2A and alzheimer disease," *Current Alzheimer Research,* vol. 9, no. 2, p. 248–256, 2012.

[132] P. Rudrabhatla and H. C. Pant, "Role of protein phosphatase 2A in alzheimers disease," *Current Alzheimer Research,* vol. 8, no. 6, pp. 623 - 632 , 2011.

[133] D. Haesen, L. Abbasi Asbagh, R. Derua, A. Hubert, S. Schrauwen, Y. Hoorne, F. Amant, E. Waelkens, A. Sablina and V. Janssens, "Recurrent PPP2R1A mutations in uterine cancer act through a dominant-negative mechanism to promote malignant cell growth," *Cancer research,* vol. 76, no. 19, pp. 5719-5731, 2016.

[134] C. M. O'Connor, D. Leonard, D. Wiredja, R. A. Avelar, Z. Wang, D. Schlatzer, B. Bryson, E. Tokala, S. E. Taylor and A. Upadhyay, "Inactivation of PP2A by a recurrent mutation drives resistance to MEK inhibitors," *Oncogene,* vol. 39, no. 3, pp. 703-717, 2020.

[135] R. Ruediger, J. Ruiz and G. Walter, "Human cancer-associated mutations in the Aα subunit of protein phosphatase 2A increase lung cancer incidence in Aα knock-in and knockout mice," *Molecular and cellular biology,* vol. 31, no. 18, pp. 3832-3844, 2011.

[136] A. A. Al Balushi and R. Gordon, "A label-free untethered approach to single-molecule protein binding kinetics," *Nano Lett,* vol. 14, no. 10, pp. 5787-5791, 2014.

[137] A. A. Al Balushi, A. Kotnala, S. Wheaton, R. M. Gelfand, Y. Rajashekara and R. Gordon, "Label-free free-solution nanoaperture optical tweezers for single molecule protein studies," *Analyst,* vol. 140, no. 14, pp. 4760 - 4778 , 2015.

[138] S. Wheaton and R. Gordon, "Molecular weight characterization of single globular proteins using optical nanotweezers," *The Analyst,* vol. 140, no. 14, pp. 4799-4803, 2015.

[139] C. Ying, E. Karakaci, E. Bermudez-Urena, A. Ianiro, C. Foster, S. Awasthi, A. Guha, L. Bryan, J. List, S. Balog, G. P. Acuna, R. Gordon and M. Mayer, *Watching Single Unmodified Enzymes at Work,* arXiv: 2107.06407 [cs], July 2021.

[140] J. Becker, J. S. Peters, I. Crooks, S. Helmi, M. Synakewicz, B. Schuler and P. Kukura, "A Quantitative Description for Optical Mass Measurement of Single Biomolecules," *ACS Photonics,* vol. 10, no. 8, pp. 2699 - 2710, 2023.

[141] J. L. Sebastián, S. Muñoz and M. Sancho, "Polarizability of shelled particles of arbitrary shape in lossy media with an application to hematic cells," *Physical Review E,* vol. 78, no. 051905, pp. 1 - 11 , 2008.

[142] R. Gordon and A. Ahmed, "Reaching the Limits of Enhancement in (Sub)Nanometer Metal Structures," *ACS Photonics,* vol. 5, no. 11, pp. 4222 - 4228 , 2018.

[143] R. B. Miles, W. R. Lempert and J. N. Forkey, "Laser Rayleigh scattering," *Meas. Sci. Technol.,* vol. 12, no. 5, pp. R33 - R51 , 2001.

[144] S. Margulies, "Force on a dielectric slab inserted into a parallel-plate capacitor," *Am. J. Phys.,* vol. 52, no. 6, pp. 515 - 518 , 1984.

[145] R. Regmi, A. A. Al Balushi, H. Rigneault, R. Gordon and J. Wenger, "Nanoscale volume confinement and fluorescence enhancement with double nanohole aperture," *Sci Rep,* vol. 5, no. 15852, pp. 1 - 10, 2015.

[146] G. Hajisalem, B. Elham, M. Dobinson, S. Iwamoto, Z. Sharifi, E. Jon, M. Synakewicz, L. S. Itzhaki and R. Gordon, "Accessible high-performance double nanohole tweezers," *Optics Express,* vol. 30, no. 3, pp. 3760 - 3769 , 2022.

[147] N. B. Viana, T. S. Freier and O. N. Mesquita, "Dyanamic light scattering from an optically trapped microsphere," *Phys Rev E,* vol. 65, no. 4, pp. 1 - 11, 2002.

[148] L. S. Booth, E. V. Browne, N. P. Mauranyapin, L. S. Madsen, S. Barfoot, A. Mark and W. P. Bowen, "Modelling of the dynamic polarizability of macromolecules for single-molecule optical biosensing," *Scientific Reports,* vol. 12, no. 1, p. 1995, 2022.

[149] J. C. Blackstock, "CHAPTER 4 - Amino acids and proteins," in *Guide to Biochemistry (Blackstock, J. C, Ed.)*, Oxford, Butterworth-Heinemann, 1989, pp. 32 - 52 .

[150] C. M. Vun, "Conformational change in Protein," 25 November 1996. [Online]. Available: http://www.cryst.bbk.ac.uk/PPS2/projects/vun/PPS96proj_Vun.htm. [Accessed 17 April 2022].

[151] R. H. Khan, M. Siddiqi and P. Salahuddin, "Protein Structure and Function," Austin Publishing Group, New Jersey, 2017.

[152] F. Sanger, "The Arrangement of Amino Acids in Proteins," in *Advances in Protein Chemistry (Anson, M. L; Bailey, K; Edsall, J. T, Eds.)*, Amsterdam, Elsevier, 1952, pp. 1 - 67 .

[153] H. M. Berman, J. Westbrook, Z. Feng, G. Gilliland, T. N. Bhat, H. Weissig, I. N. Shindyalov and P. E. Bourne, "The Protein Data Bank," *Nucleic Acids Research,* vol. 28, no. 1, pp. 235 - 242 , 2000.

[154] D. L. Nelson and M. M. Cox, Lehninger Principles of Biochemistry, 6th Edition, New York: W. H. Freeman and Company, 2013.

[155] H. P. Erickson, "Size and shape of protein molecules at the nanometer level determined by sedimentation, gel filtration, and electron microscopy," *Biological Procedures Online,* vol. 11, pp. 32 - 51 , 2009.

[156] M. R. Groves, N. Hanlon, P. Turowski, B. A. Hemmings and D. Barford, "The Structure of the Protein Phosphatase 2A PR65/A Subunit Reveals the Conformation of Its 15 Tandemly Repeated HEAT Motifs," *Cell,* vol. 96, no. 1, pp. 99 - 110 , 1999.

[157] S. Yi Gong, "Assembly and structure of protein phosphatase 2A," *Sci China Ser C-Life Sci,* vol. 52, no. 2, pp. 135 - 146, 2009.

[158] A. G. Arimbasseri and R. J. Maraia, "Distinguishing Core and Holoenzyme Mechanisms of Transcription Termination by RNA Polymerase III," *Molecular and Cellular Biology,* vol. 33, no. 8, pp. 1571 - 1581 , 2013.

[159] K. S. Bhullar, N. O. Lagarón, E. M. McGowan, I. Parmar, A. Jha, B. P. Hubbard and V. H. P. Rupasinghe, "Kinase-targeted cancer therapies: progress, challenges and future directions," *Molecular Cancer,* vol. 17, no. 48, pp. 1 - 20 , 2018.

[160] H.-C. Cheng, R. Z. Qi, H. Paudel and H.-J. Zhu, "Regulation and Function of Protein Kinases and Phosphatases," *Enzyme Res.*, vol. 2011, no. 794089, pp. 1 - 3 , 2011.

[161] A. A. Sablina and W. C. Hahn, "The Role of PP2A A Subunits in Tumor Suppression," *Cell Adh Migr.,* vol. 1, no. 3, pp. 140 - 141 , 2007.

[162] A. F. Johnson, H. Nguyen and R. A. Veitia, "Causes and effects of haploinsufficiency," *Biol Rev Camb Philos Soc,* vol. 94, no. 5, pp. 1774-1785, 2019.

[163] H. Apparatus, "Overview of Equilibrium Dialysis," 2020. [Online]. Available: https://www.harvardapparatus.com/overview-equilibrium-dialysis. [Accessed 23 April 2022].

[164] A. E. Ruoho, H. Kiefer, P. E. Roeder and S. J. Singer, "The Mechanism of Photoaffinity Labeling," *Proc. Nat. Acad. Sci. USA,* vol. 70, no. 9, pp. 2567 - 2571 , 1973.

[165] E. Smith and I. Collins, "Photoaffinity labeling in target- and binding-site identification," *Future Med Chem.*, vol. 7, no. 2, pp. 159 - 183 , 2015.

[166] E. L. Rodriguez, S. Poddar, S. Iftekhar, K. Suh, A. G. Woolfork, S. Ovbude, A. Pekarek, M. Walters, S. Lott and D. S. Hage, "Affinity chromatography: A review of trends and developments over the past 50 years," *Journal of Chromatography B,* vol. 1157, no. 10, pp. 122332-1 - 122332-16, 2020.

[167] S. E, A. Itkin, Y. Y. Kuttner, E. Rhoades, D. Amir, E. Haas and G. Haran, "Using fluorescence correlation spectroscopy to study conformational changes in denatured proteins," *Biophys J,* vol. 94, no. 12, pp. 4819-4827, 2008.

[168] T. Heyduk, "Measuring protein conformational changes by FRET/LRET," *Current opinion in biotechnology,* vol. 13, no. 4, pp. 292-296, 2002.

[169] A. E. M. Beedle and S. Garcia-Manyes, "The role of single-protein elasticity in mechanobiology," *Nat Rev Mater,* vol. 8, pp. 10-24, 2023.

[170] Y. Pang and R. Gordon, "Optical trapping of 12 nm dielectric spheres using double-nanoholes in a gold film," *Nano Lett.,* vol. 11, no. 9, pp. 3763-3767, 2011.

[171] T. F. D. b. Farlex, "lithos," 2011. [Online]. Available: https://www.thefreedictionary.com/lithos. [Accessed 29 April 2022].

[172] Wiktionary, "γράφειν.," 16 October 2019. [Online]. Available: https://en.wiktionary.org/w/index.php?title=%CE%B3%CF%81%CE%AC%CF%86%CE%B5%CE%B9%CE%BD&oldid=55780346.. [Accessed 29 April 2022].

[173] S. Frank, "LITHOGRAPHY," 3 November 2021. [Online]. Available: https://www.tate.org.uk/art/art-terms/l/lithography. [Accessed 29 April 2022].

[174] W. contributors, "Alois Senefelder," 26 January 2022. [Online]. Available: https://en.wikipedia.org/w/index.php?title=Alois_Senefelder&oldid=1068030434. [Accessed 29 April 2022].

[175] U. C. Fischer and H. P. Zingsheim, "Submicroscopic pattern replication with visible light," *Journal of Vacuum Science and Technology,* vol. 19, no. 4, pp. 881 - 885 , 1981.

[176] H. W. Deckman and J. H. Dunsmuir, "Natural lithography," *Appl. Phys. Lett.,* vol. 41, no. 4, pp. 377 - 378, 1982.

[177] C. L. Haynes and R. P. Van Duyne, "Nanosphere Lithography: A Versatile Nanofabrication Tool for Studies of Size-Dependent Nanoparticle Optics," *J. Chem. B,* vol. 105, no. 24, pp. 5599 - 5611, 2001.

[178] J. C. Hulteen, D. A. Treichel, M. T. Smith, M. L. Duval, T. R. Jensen and R. P. Van Duyne, "Nanosphere Lithography: Size-Tunable Silver Nanoparticle and Surfcae Cluster Arrays," *J. Phys. Chem. B.*, vol. 103, no. 19, pp. 3854 - 3863, 1999.

[179] U. C. Fischer, "Optical characteristics of 0.1 μm circular apertures in a metal," *Journal of Vacuum Science & Technology B: Microelectronics Processing and Phenomena*, vol. 3, no. 1, pp. 386 - 390, 1985.

[180] U. C. Fischer, "Submicrometer aperture in a thin metal film as a probe of its microenvironment through enhanced light scattering and flourescence," *JOSA B,* vol. 3, no. 10, pp. 1239 - 1244, 1986.

[181] S. H. Lee, K. C. Bantz, N. C. Lindquist, S.-H. Oh and C. L. Haynes, "Self-assembled plasmonic nanohole arrays," *Langmuir,* vol. 25, no. 23, pp. 13685 - 13693 , 2009.

[182] M.-P. Murray-Méthot, M. Ratel and J.-F. Masson, "Optical properties of Au, Ag, and bimetallic Au on Ag nanohole arrays," *The Journal of Physical Chemistry C,* vol. 114, no. 18, pp. 8268 - 8275 , 2010.

[183] J.-F. Masson, M.-P. Murray-Méthot and L. S. Live, "Nanohole arrays in chemical analysis: manufacturing methods and applications," *Analyst,* vol. 135, no. 7, pp. 1483 - 1489 , 2010.

[184] T.-D. Onuta, M. Waegele, C. C. DuFort, W. L. Schaich and B. Dragnea, "Optical Field Enhancement at Cusps Between Adjacent Nanoapertures," *Nano Letters,* vol. 7, no. 3, pp. 557 - 564 , 2007.

[185] C. Qiaoying and J. Y. Yong, "A review of polystyrene bead manipulation by dielectrophoresis," *RSC Adv.*, vol. 9, pp. 4963-4981, 2019.

[186] L. O. Mair, B. Evans, A. R. Hall, J. Carpenter, A. Shields, K. Ford, M. Millard and R. Superfine, "Highly controllable near-surface swimming of magnetic Janus nanorods: application to payload capture and manipulation," *Journal of Physics D: Applied Physics,* vol. 44, no. 12, p. 125001, 2011.

[187] J. Berthelot, S. S. Aćimović, M. L. Juan, M. P. Kreuzer, J. Renger and R. Quidant, "Three-dimensional manipulation with scanning near-field optical nanotweezers," *Nature Nanotechnology,* vol. 9, no. 4, pp. 295-299, 2014.

[188] W. Yang, M. van Dijk, C. Primavera and C. Dekker, "Fib-milled plasmonic nanoapertures allow for long trapping times of individual proteins," *iScience,* vol. 24, no. 103237, 2021.

[189] H. Zhang, P. Moazzezi, J. Ren, B. Henderson, C. Cordoba, V. Yeddu, A. M. Blackburn, M. I. Saidaminov, I. Paci, S. Hughes and R. Gordon, "Coupling Perovskite Quantum Dot Pairs in Solution using a Nanoplasmonic Assembly," *Nano Lett,* vol. 22, no. 13, pp. 5287-5293, 2022.

[190] R. A. Jensen, I.-C. C. O. Huang, J. T. Choy, T. S. Bischof, M. Lončar and M. G. Bawendi, "Optical Trapping and Two-Photon Excitation of Colloidal Quantum Dots Using Bowtie Apertures," *ACS Photonics,* vol. 3, no. 3, pp. 2330-4022, 2016.

[191] C. Hong and J. C. Ndukaife, "Scalable trapping of single nanosized extracellular vesicles using plasmonics," *arXiv preprint arXiv:2302.07370,* 2023.

[192] L. Neumeier, R. Quidant and D. E. Chang, "Self-induced back-action optical trapping in nanophotonic systems," *New J. Phys.,* vol. 17, no. 123008, 2015.

[193] M. Barth and O. Benson, "Manipulation of dielectric particles using photonic crystal cavities," *Appl. physics letters,* vol. 89, 2006.

[194] D. Nicolas, P. D. Ulagalandha, D. Zhaolu, T. Mario and R. Houdré, "Observation of Backaction and Self-Induced Trapping in a Planar Hollow Photonic Crystal Cavity," *Phys. Rev. Lett.,* vol. 110, no. 12, pp. 123601-123604, 2013.

[195] S. H. Mirsadeghi and J. F. Young, "Ultrasensitive diagnostic analysis of au nanoparticles optically trapped in silicon photonic circuits at sub-milliwatt powers," *Nano Lett.,* vol. 14, pp. 5004-5009, 2014.

[196] M. Pau, B. Johann, S. A. Srdjan and Q. Romain, "Unraveling the optomechanical nature of plasmonic trapping," *Light Sci Appl,* vol. 5, no. 7, pp. e16092-e16092, 2016.

[197] H. A. Bethe, "Theory of diffraction by small holes," *Phys. Rev,* vol. 66, p. 163–182 , 1944.

[198] P. B. Catrysse and S. Fan, "Propagating plasmonic mode in nanoscale apertures and its implications for extraordinary transmission," *J. Nanophotonics,* vol. 2, p. 021790, 2008.

[199] G. S. Karlberg, "Adsorption trends for water, hydroxyl, oxygen, and hydrogen on transition-metal and platinum-skin surfaces," *Phys. Rev. B ,* vol. 74, p. 153414, 2006.

[200] A. Degiron, H. Lezec, N. Yamamoto and T. T. Ebbesen, "Optical transmission properties of a single subwavelength aperture in a real metal," *Opt. Commun. ,* vol. 239, p. 61–66, 2004.

[201] M. Peters, D. McIntosh, B. A. Albu, C. Ying and R. Gordon, "Label-free tracking of proteins through plasmon-enhanced interference," *ACS Nanosci. Au,* 2023.

[202] H. W. Kihm, S. M. Koo, Q. H. Kim, K. Bao, J. E. Kihm, W. S. Bak, S. H. Eah, C. Lienau, H. Kim, N. J. P. Nordlander, Halas, N. K. Park and D.-S. Kim, "Bethe-hole polarization analyser for the magnetic vector of light," *Nat. Commun,* vol. 2, no. 451, 2011.

[203] F. D. M and S. M. Rosenberg, "What is mutation?," *PLoS Genet,* vol. 15, no. 4, pp. 1-14, 2019.

[204] M. Chiasson and D. M. Fowler, "Mutagenesis-based protein structure determination," *Nat Genet,* vol. 51, pp. 1072-1073, 2019.

[205] H. Hegyi and M. Gerstein, "The relationship between protein structure and function: a comprehensive survey with application to the yeast genome 11Edited by G. von Heijne," *Journal of Molecular Biology,* vol. 288, no. 1, pp. 147-164, 1999.

[206] G. Shannon, C. R. Marples, R. D. Toofanny and P. M. Williams, "Evolutionary drivers of protein shape," *Scientific Reports,* vol. 9, no. 1, p. 11873, 2019.

[207] L. F. I. Torrent, "PP2A and Alzheimer Disease," *Current Alzheimer Research,* vol. 9, no. 2, pp. 248 - 256, 2012.

[208] A. J. García-Sáez and S. P, "Single molecule techniques for the study of membrane proteins," *Appl Microbiol Biotechnol,* vol. 76, no. 2, pp. 257-266, 2007.

[209] R. Roy, S. Hohng and T. Ha, "A practical guide to single-molecule FRET," *Nat Methods,* vol. 5, no. 6, pp. 507-516, 2008.

[210] O. K. Dudko, G. Hummer and A. Szabo, "Theory, analysis, and interpretation of single-molecule force spectroscopy experiments," *Proceedings of the National Academy of Sciences,* vol. 105, no. 41, pp. 15755-15760, 2008.

[211] A. Syahir, K. Usui, K. Y. Tomizaki, K. Kajikawa and H. Mihara, "Label and Label-Free Detection Techniques for Protein Microarrays," *Microarrays (Basel),* vol. 4, no. 2, pp. 228-244, 2015.

[212] E. Babaei, D. Wright and R. Gordon, "Fringe Dielectrophoresis Nanoaperture Optical Trapping with Order of Magnitude Speed-Up for Unmodified Proteins," *Nano Lett.*, vol. 23, no. 7, pp. 2877-2882, 2023.

[213] D. Kümmel and U. Heinemann, "Diversity in structure and function of tethering complexes: evidence for different mechanisms in vesicular transport regulation," *Current protein & peptide science,* vol. 9, no. 2, pp. 197-209, 2008.

[214] A. Zehtabi-Oskuie, H. Jiang, B. R. Cyr, D. W. Rennehan, A. A. Al-Balushi and R. Gordon, "Double nanohole optical trapping: dynamics and protein-antibody co-trapping," *Lab Chip,* vol. 13, no. 13, pp. 2563-2568, 2013.

[215] F. Català, F. Marsà, M. Montes-Usategui, A. Farré and E. Martín-Badosa, "Influence of experimental parameters on the laser heating of an optical trap," *Scientific Reports,* vol. 7, no. 1, p. 16052, 2017.

[216] T. Arodź and P. M. Płonka, "Effects of point mutations on protein structure are nonexponentially distributed," *Proteins: Structure, Function, and Bioinformatics,* vol. 92, no. 1, pp. 225-233, 2007.

[217] r. sjh, "Optical Tweezers," 14 October 2020. [Online]. Available: https://www.phys.ufl.edu/courses/phy4803L/group_IV/optical_tweezers/OT.pdf. [Accessed 3 March 2024].

[218] K. Berg-Sørensen and H. Flyvbjerg, "Power spectrum analysis for optical tweezers," *Rev. Sci. Instrum.*, vol. 75, no. 3, p. 594–612, 2004.

[219] Z. Xu, W. Song and K. B. Crozier, "Direct Particle Tracking Observation and Brownian Dynamics Simulations of a Single Nanoparticle Optically Trapped by a Plasmonic Nanoaperture," *ACS Photonics,* vol. 5, no. 7, pp. 2850-2859, 2018.

[220] Q. Jiang, B. Rogez, J. B. Claude, A. Moreau, J. Lumeau, G. Baffou and J. Wenger, "Adhesion layer influence on controlling the local temperature in plasmonic gold nanoholes," *Nanoscale,* vol. 12, no. 4, pp. 2524-2531, 2020.

[221] B. S. Cooperman, "Allosteric Regulation," in *Encyclopedia of Biological Chemistry (Second Edition)*, Waltham, Academic Press, 2013, pp. 71-74.

[222] W. contributors, "Allosteric regulation," Wikipedia, The Free Encyclopedia, 24 August 2023. [Online]. Available: https://en.wikipedia.org/w/index.php?title=Allosteric_regulation&oldid=1171997337. [Accessed 13 November 2023].

[223] L. J and N. R, "Allostery: An Overview of Its History, Concepts, Methods, and Applications," *PLoS Comput Biol* , vol. 12, no. 6, p. e1004966, 2016.

[224] A. Cooper and D. T. F. Dryden, "Allostery without conformational change," *European Biophysics Journal,* vol. 11, no. 2, pp. 103-109, 1984.

[225] R. G. Smock and L. M. Gierasch, "Sending Signals Dynamically," *Science,* vol. 324, no. 5924, pp. 198-203, 2009.

[226] I. Bahar, T. R. Lezon, A. Bakan and I. H. Shrivastava, "Normal Mode Analysis of Biomolecular Structures: Functional Mechanisms of Membrane Proteins," *Chem. Rev,* vol. 110, no. 3, pp. 1463-1497, 2010.

[227] J. Sangodkar, C. C. Farrington, K. McClinch, M. D. Galsky, D. B. Kastrinsky and G. Narla, "All roads lead to PP2A: exploiting the therapeutic potential of this phosphatase," *The FEBS journal,* vol. 283, no. 6, pp. 1004-1024, 2016.

[228] M. Tsytlonok, P. Craig, E. Sivertsson, D. Serquera, S. Perrett, R. Best, P. Wolynes and L. Itzhaki, "Complex Energy Landscape of a Giant Repeat Protein," *Structure,* vol. 21, no. 11, pp. 1954-1965, 2013.

[229] Y. Shi, "Serine/threonine phosphatases: mechanism through structure," *Cell,* vol. 139, no. 3, pp. 468-484, 2009.

[230] K. Abdi, G. Lee, M. Rabbi, W. Lee, M. Yang, C. J. Schofield, V. Bennett and P. E. Marszalek, "Fast and forceful refolding of stretched alpha-helical solenoid proteins," *Biophysical Journal,* vol. 98, no. 12, pp. 3086-3092, 2010.

[231] M. Synakewicz, R. S. Eapen, A. Perez-Riba, P. J. E. Rowling, D. Bauer, A. Weißl, G. Fischer, M. Hyvönen, M. Rief, L. S. Itzhaki and J. Stigler, "Unraveling the Mechanics of a Repeat-Protein Nanospring: From Folding of Individual Repeats to Fluctuations of the Superhelix," *ACS Nano,* vol. 16, no. 3, pp. 3895-3905, 2022.

[232] D. Verschueren, X. Shi and C. Dekker, "Nano-Optical Tweezing of Single Proteins in Plasmonic Nanopores," *Small Methods,* vol. 3, no. 5, pp. 2366-9608, 2019.

[233] Z. Xu, W. Song and K. B. Crozier, "Direct particle tracking observation and Brownian dynamics simulations of a single nanoparticle optically trapped by a plasmonic nanoaperture," *ACS Photonics,* vol. 5, no. 7, pp. 2850-2859, 2018.

[234] U. R. Muhammad, S. S. P. Sai, M. Liang-Chieh, M. I. Samir and A. George, "Self-induced back action actuated nanopore electrophoresis (SANE)," *Nanotechnology,* vol. 29, no. 43, p. 435501, 2018.

[235] M. R. Groves, N. Hanlon, P. Turowski, B. Hemmings and D. Barford, "Crystal structure of constant regulatory domain of human PP2A, PR65ALPHA, doi: 10.2210/pdb1B3U/pdb," 1998.

[236] S. R. K. Ainavarapu, J. Brujic, H. H. Huang, A. P. Wiita, H. Lu, L. Li, K. A. Walther, M. Carrion-Vazquez, H. Li and J. M. Fernandez, "Contour length and refolding rate of a small protein controlled by engineered disulfide bonds," *Biophysical journal,* vol. 92, no. 1, pp. 225-233, 2007.

[237] D. Xu and R. Nussinov, "Favorable domain size in proteins," *Fold Des,* vol. 3, no. 1, pp. 11-17, 1998.

[238] J. Stetefeld and S. A. McKenna, "Dynamic light scattering: a practical guide and applications in biomedical sciences," *Biophys Rev,* vol. 8, no. 4, pp. 409-427, 2016.

[239] L. S. Booth, E. V. Browne, N. P. Mauranyapin, L. S. Madsen, S. Barfoot, A. Mark and W. P. Bowen, "Modelling of the dynamic polarizability of macromolecules for single-molecule optical biosensing," *Scientific Reports,* vol. 12, no. 1, p. 1995, 2022.

[240] S. S. S. Peri, M. K. Sabnani, M. U. Raza, E. L. Urquhart, S. Ghaffari, J. S. Lee, M. J. Kim, J. Weidanz and G. Alexandrakis, "Quantification of low affinity binding interactions between natural killer cell inhibitory receptors and targeting ligands with a self-induced back-action actuated nanopore electrophoresis (SANE) sensor," *Nanotechnology,* vol. 4, no. 32, p. 045501, 2021.

[241] D. Yoo, K. L. Gurunatha, H.-K. Choi, D. A. Mohr, C. T. Ertsgaard, R. Gordon and S.-H. Oh, "Low-Power Optical Trapping of Nanoparticles and Proteins with Resonant Coaxial Nanoaperture Using 10 nm Gap," *Nano Lett*, vol. 18, no. 6, pp. 3637-3642, 2018.

[242] A. Yousefi, C. Ying, C. D. J. Parmenter, M. Assadipapari, G. Sanderson, Z. Zheng, L. Xu, S. Zargarbashi, G. J. Hickman, R. B. Cousins, C. J. Mellor, M. Mayer and M. Rahmani, "Optical Monitoring of In Situ Iron Loading into Single, Native Ferritin Proteins," *Nano Lett*, vol. 23, no. 8, pp. 3251-3258, 2023.

Appendix A. MATLAB Code for Computing PSD

```
function [] = psd_comp(FileName,vsp)
%This fxn takes an input data file and returns plots of PSD and
%Laurentzian fit and prints the corner frequency as a title
%FileName = file name. File must be .txt format. E.g.,'pr65_today_1.txt';
%vsp = row vector of time points that define the data segment to compute
%PSD from. E.g., to compute PSD from a data segment from
%t = 8 s to t = 10 s, then vsp = [8,10];
% Call: psd_comp(FileName,vp);
%NOTE: The trapping data should have no more than one jump.
fs=100000;
fid=fopen(FileName);
M=textscan(fid,'%f','HeaderLines',15,'CollectOutput',1);
fclose(fid);
A=M{1};

%%%%%%% SEGMENT WHICH PICKS OUT SEGMENT OF RAW DATA TO COMPUTE PSD FROM %%%%%%%%%%%%

A2=A((numel(A)-1000)+1:end);
mide=mean(A2);
lst=min(A);lsti=find(A==lst);
if lsti==numel(A)
    disp('problem: have to find jump position by hand!')
else
    for iq=lsti:numel(A)
        if A(iq)-lst>=mide-lst
            idj=iq;
            break;
        end
    end
end
idu=idj-20000;
An=A(1:idu);
ins=100;
nf=round(numel(An)/ins);
boi=1;
vec=[];
av=[];
for id=1:nf
    if id*ins>numel(An)
        break;
    end
    eoi=id*ins;
    temps=An(boi:eoi);
    if numel(temps)<ins

    else
        vec(id)=mean(abs(temps-mean(temps)));
        av(id)=mean(temps);
    end
```

```
    boi=eoi+1;
end
kz=find(vec==min(vec));
if numel(kz)>1
    kzu=kz(1);
else
    kzu=kz;
end
Am=av(kzu);
B=A(fs*(vsp(1):vsp(2)))/Am;

%%% SEGMENT WHICH PERFORMS PSD COMPUTATION AS WELL AS LAURENTZIAN FIT %%%%%%%%

nt=0.2;
ntd=nt*fs;
nn=numel(B);
rmd=rem(nn,ntd);
if rmd~=0
    k=(nn-rmd)/ntd;
else
    k=nn/ntd;
end
bvn=cell(1,[]);
for i=1:k
    temp=B(((i-1)*ntd)+1:i*ntd);
    bvn{i}=temp;
end
nbd=numel(bvn{1});
nj=numel(bvn);
pstm=zeros(nbd,nj);
for jj=1:nj
    temp1=bvn{jj};
    x=(1:nbd)*(1/fs);
    a=[sum(x.^2),sum(x);sum(x),numel(x)];b=[sum(x.*temp1');sum(temp1)];
    X=a\b;Y=(X(1)*x)+X(2);
    pstm(:,jj)=temp1-Y';
end
wn=zeros(nbd,1);
for jk=1:nbd
    wn(jk)=0.5*(1-cos(2*pi*(jk-1)/nbd));
end
s1=sum(wn);
mat=zeros((nbd/2)+1,nj);
for ij=1:nj
    yfft=fft(pstm(:,ij).*wn,nbd);
    yfftn=yfft(1:nbd/2+1);
    psd=(1/(s1^2))*abs(yfftn).^2;
    psd(2:end-1)=2*psd(2:end-1);
    mat(:,ij)=psd;
end
pxx=mean(mat,2);
f=0:fs/nbd:fs/2;
psdx=pxx(2:end-1);
freq=f(2:end-1)';
qp=freq>=10;qr=freq>=1380;qs=qp-qr;qq=find(qs~=0);
```

```
p=psdx(qq);
pp=psdx(qq);
fp=freq(qq);
fpp=freq(qq);
psd_fit=@(As,fc,fp)log10(As)-log10(fc^2+fp.^2);
obj_f=@(params)sum((log10(p)-psd_fit(params(1),params(2),fp)).^2);
start_point=rand(1,2);
opts1 = optimset ('MaxFunEvals',1e6);
opts2 = optimset('maxiter',1e6);
options = optimset(opts1,opts2);
estimates = fminsearch(obj_f, start_point,options);
Au=estimates(1);f_c=estimates(2);
fsc=f_c/max(fp);
while 1
    if fsc>0.1
        break;
    end
    start_point=rand(1,2);
    opts1 = optimset ('MaxFunEvals',1e6);
    opts2 = optimset('maxiter',1e6);
    options = optimset(opts1,opts2);
    estimates = fminsearch(obj_f, start_point,options);
    Au=estimates(1);f_c=estimates(2);
    fsc=f_c/max(fp);
end
psdxn=Au./(f_c^2+fp.^2);

%%% SEGMENT WHICH PLOTS THE RESULTS %%%%%%%%

fig2=figure('Color','w');
loglog(fpp,pp,'.r','LineWidth',2);
hold on;
loglog(fp,psdxn,'-b','LineWidth',2);
xlabel('frequency (Hz)','FontSize',12)
ylabel('psd (V$^2$/Hz)','FontSize',12)
% title({['upper state'],['$f_c$ = ',num2str(f_c),' Hz']},'FontSize',12);
title({['$f_c$ = ',num2str(f_c),' Hz']},'FontSize',12);
legend({['data'],['Lorentzian fit']},'FontSize',12)
ax=gca;ay=gca;
ax.LineWidth=1.25;
ay.LineWidth=1.25;

saveas(gcf,'PSD','svg');
```

Appendix B. MATLAB Script For Plotting The PSD

```
%%% Script for Plotting the PSD %%%
clear;
clc;
close all;
format long;
set(groot,'defaulttextinterpreter','latex');
name='pr65_today_1.txt';
fs=100000;
ts=18.3314;te=19.9419;
vp=[ts,te];
psd_comp(name,vp);
set(gcf,'InvertHardcopy','off');
saveas(gcf,'PSD_pr65_WT9','svg');
```

Appendix C. MATLAB Code for Computing RMSD

```
function [] = rmsd_comp_projs(FileName,tj,fs,vsp,nbars)
%This fxn takes an input data file and returns plots of returns plots of
%histogram and Gaussian fit and prints the rmsd as a title
%FileName = file name. File must be .txt format. E.g.,'pr65_today_1.txt';
%tj = time point where jump occurs if computed by hand. Initially
%set tj =[]. If the program can not automatically find tj, the user
%will be prompted to compute this manually and then call this function
%again with the value of tj as a second input argument. If prompted
%by the program to compute tj manually, all that is required is to
%plot the trapping data vs time and find the time point where the
%jump occurs by eye inspection. Let's say that this time point is ts,
%then tj = ts.
%vsp=row vector of time points that define the data segment to compute
%PSD from. E.g., to compute PSD from a data segment from
%t = 8 s to t = 10 s, then vsp = [8,10];
%NOTE: vsp must be the same for both the PSD and the RMSD computations.
%fs=sampling frequency at which trapping data was acquired.
%nbars=number of bars that give best look to plot of histogram and
%Gaussian envelop. The bars of the histogram should fit in the envelop
%as closely as possible. User can try any nbars>=25;e.g., nbars=35.
% Call: rmsd_comp_projs(FileName,[],fs,vsp,nbars) or
% rmsd_comp_projs(FileName,tj,fs,vsp,nbars) if tj is found manually.
%NOTE: The trapping data should have no more than one jump.
fid=fopen(FileName);
M=textscan(fid,'%f','HeaderLines',15,'CollectOutput',1);
fclose(fid);
A=M{1};
if isempty(tj)
    A2=A((numel(A)-1000)+1:end);
    mide=mean(A2);
    lst=min(A);lsti=find(A==lst);
    if numel(lsti)>1
        ilst=round(quantile(lsti,0.5));
    else
        ilst=lsti;
    end
    if numel(lsti)==numel(A)||ilst>=floor((1+numel(A))/2)
        disp(['signal has drift: have to find jump position by eye ...' ...
            'then enter manually as 3rd argument in call to this function!']);
        return;
    else
        for iq=lsti:numel(A)
            if A(iq)-lst>=mide-lst
                idj=iq;
                break;
            end
        end
    end
else
    idj=tj*fs;
```

```
end
idu=idj-20000;
An=A(1:idu);
ins=100;
nf=round(numel(An)/ins);
boi=1;
vec=[];
av=[];
for id=1:nf
    if id*ins>numel(An)
        break;
    end
    eoi=id*ins;
    temps=An(boi:eoi);
    if numel(temps)<ins

    else
        vec(id)=mean(abs(temps-mean(temps)));
        av(id)=mean(temps);
    end
    boi=eoi+1;
end
kz=find(vec==min(vec));
if numel(kz)>1
    kzu=kz(1);
else
    kzu=kz;
end
Am=av(kzu);
t=(1:1:length(A))/fs;
si=vsp(1)>t;se=vsp(2)>=t;di=se-si;ip=di~=0;
B=A(ip)/Am;
tp=t(ip);
nt=0.2;
ntd=nt*fs;
nn=numel(B);
rmd=rem(nn,ntd);
if rmd~=0
    k=(nn-rmd)/ntd;
else
    k=nn/ntd;
end
bvn=cell(1,[]);
for i=1:k
    temp=B(((i-1)*ntd)+1:i*ntd);
    bvn{i}=temp;
end
nbd=numel(bvn{1});
nj=numel(bvn);
pstm=zeros(nbd,nj);
for jj=1:nj
    temp1=bvn{jj};
    x=(1:nbd)*(1/fs);
    a=[sum(x.^2),sum(x);sum(x),numel(x)];b=[sum(x.*temp1');sum(temp1)];
    X=a\b;Y=(X(1)*x)+X(2);
```

```
    pstm(:,jj)=temp1-Y';
end
wn=zeros(nbd,1);
for jk=1:nbd
    wn(jk)=0.5*(1-cos(2*pi*(jk-1)/nbd));
end
s1=sum(wn);
mat=zeros((nbd/2)+1,nj);
for ij=1:nj
    yfft=fft(pstm(:,ij).*wn,nbd);
    yfftn=yfft(1:nbd/2+1);
    psd=(1/(s1^2))*abs(yfftn).^2;
    psd(2:end-1)=2*psd(2:end-1);
    mat(:,ij)=psd;
end
pxx=mean(mat,2);
f=0:fs/nbd:fs/2;
psdx=pxx(2:end-1);
freq=f(2:end-1)';
qp=freq>=10;qr=freq>=1380;qs=qp-qr;qq=find(qs~=0);
p=psdx(qq);
pp=psdx(qq);
fp=freq(qq);
fpp=freq(qq);
psd_fit=@(As,fc,fp)log10(As)-log10(fc^2+fp.^2);
obj_f=@(params)sum((log10(p)-psd_fit(params(1),params(2),fp)).^2);
start_point=rand(1,2);
opts1 = optimset ('MaxFunEvals',1e6);
opts2 = optimset('maxiter',1e6);
options = optimset(opts1,opts2);
estimates = fminsearch(obj_f, start_point,options);
Au=estimates(1);f_c=estimates(2);
fsc=f_c/max(fp);
while 1
    if fsc>0.1
        break;
    end
    start_point=rand(1,2);
    opts1 = optimset ('MaxFunEvals',1e6);
    opts2 = optimset('maxiter',1e6);
    options = optimset(opts1,opts2);
    estimates = fminsearch(obj_f, start_point,options);
    Au=estimates(1);f_c=estimates(2);
    fsc=f_c/max(fp);
end
cf=2*f_c;
design_LPF=designfilt('lowpassfir','FilterOrder',4,'CutoffFrequency',...
    cf,'SampleRate',100000);
AA=filter(design_LPF,A);
C=AA(ip);
Ac=AA(1:idu);
inc=100;
nfc=round(numel(Ac)/inc);
boc=1;
vcc=[];
```

```
avc=[];
for idc=1:nfc
    if idc*inc>numel(Ac)
        break;
    end
    eoc=idc*inc;
    tempc=An(boc:eoc);
    if numel(tempc)<inc

    else
        vcc(idc)=mean(abs(tempc-mean(tempc)));
        avc(idc)=mean(tempc);
    end
    boc=eoc+1;
end
kzc=find(vcc==min(vcc));
if numel(kzc)>1
    kcu=kzc(1);
else
    kcu=kzc;
end
Amc=avc(kcu);
[N,edges]=histcounts(C/Amc,nbars,'Normalization','probability');
centers=zeros(1,numel(N));
for i=1:numel(N)
    centers(i)=(edges(i)+edges(i+1))/2;
end
id=find(N~=0);
centers=centers(id(1:end));
N=N(id(1:end));
y=@(a,m,s,centers)a*exp(-(((centers-m).^2)/(2*(s^2))));
obj_fxn=@(params)sum((N-y(params(1),params(2),params(3),centers)).^2);
[mn,sg]=normfit(centers);
y0=[(max(N)+min(N))/2,mn,sg];
opts1=optimset('MaxFunEvals',1e6);
opts2=optimset('maxiter',1e6);
options=optimset(opts1,opts2);
f0=fminsearch(obj_fxn,y0,options);
au=f0(1); mu=f0(2);su=f0(3);
yu=au*exp(-(((centers-mu).^2)/(2*(su^2))));
figure('Color','w');
subplot(1,2,1)
plot(t(1:idj-1),A(1:idj-1)/Am,'-k','LineWidth',2);
hold on;
plot(t(idj:end),A(idj:end)/Am,'Color',[0.5,0.5,0.5],'LineWidth',2);
plot(tp,A(ip)/Am,'Color',[0,0,1],'LineWidth',2);
hold off;
xlabel('time (s)','FontSize',14);
ylabel('T','FontSize',14);
axx=gca;ayy=gca;
axx.LineWidth=1.25;
ayy.LineWidth=1.25;
axx.FontSize=14;
set(axx,'fontname','Arial');
ayy.FontSize=14;
```

```
set(ayy,'fontname','Arial');
axis('tight');
subplot(1,2,2)
h=histogram(C/Amc,numel(N),'Normalization','probability');
hold on;
plot(centers,yu,'-k','LineWidth',2);
hold off;
h.FaceColor=[0,0,1];
h.EdgeColor=[0,0,0];
ax=gca;ay=gca;
ax.LineWidth=1.25;
ay.LineWidth=1.25;
ax.FontSize=14;
xlabel('T','FontSize',14);
ay.YTickLabel='';
ax.XAxis.Exponent = 0;
set(ax,'fontname','Arial');
ay.FontSize=14;
set(ax,'fontname','Arial');
set ( gca, 'xdir', 'reverse' );
axis('auto');
camroll(-90);
end
```

Appendix D. MATLAB Script for Plotting The RMSD

```
clear;
clc;
close all;
format long;
set(groot,'defaulttextinterpreter','latex');
name='PR65_MUTANT_B_6.txt';
rmsd_comp_projs(name,[],100000,[2,4],35);
set(gcf,'InvertHardcopy','off');
saveas(gcf,'rmsd_pr65_WT5','svg');
saveas(gcf,'rmsd_F502W_6','svg');
```

Appendix E. MATLAB Codes for Plotting The Trapping Data Vs Time

```
clear;
clc;
close all;
format long;
set(groot,'defaulttextinterpreter','latex');
fid=fopen('PR65_MUTANT_B_6.txt');
M=textscan(fid,'%f','HeaderLines',15,'CollectOutput',1);
fclose(fid);
A=M{1};
fs=100000;
step = 1/fs;
tmin = 1;
tmax = length(A);
t=(1:1:tmax)*step;

A2=A((numel(A)-1000)+1:end);
mide=mean(A2);
lst=min(A);lsti=find(A==lst);
if lsti==numel(A)
    disp('problem: have to find jump position by hand!')
else
    for iq=lsti:numel(A)
        if A(iq)-lst>=mide-lst
            idj=iq;
            break;
        end
    end
end
idu=idj-20000;
An=A(1:idu);
ins=100;
nf=round(numel(An)/ins);
boi=1;
vec=[];
av=[];
for id=1:nf
    if id*ins>numel(An)
        break;
    end
    eoi=id*ins;
    temps=An(boi:eoi);
    if numel(temps)<ins

    else
        vec(id)=mean(abs(temps-mean(temps)));
        av(id)=mean(temps);
    end
    boi=eoi+1;
end
kz=find(vec==min(vec));
if numel(kz)>1
    kzu=kz(1);
```

```
else
    kzu=kz;
end
Am=av(kzu);
B=A/Am;
figure('color','w')
plot(t(1:idj),B(1:idj),'-k','LineWidth',2);
hold on;
plot(t(idj+1:end),B(idj+1:end),'-','Color',[0.5,0.5,0.5],'LineWidth',2);
hold off;
xlabel('time (s)','FontSize',14);
ylabel('normalised transmission','FontSize',14);
ax=gca;ay=gca;
ax.LineWidth=1.25;
ay.LineWidth=1.25;
ax.FontSize=14;
set(ax,'fontname','Arial');
ay.FontSize=14;
set(ax,'fontname','Arial');
axis('tight');
set(gcf,'InvertHardcopy','off');
saveas(gcf,'MUT_L_3','svg');
```